POLITECNICO DI MILANO
DEPARTMENT OF MECHANICAL ENGINEERING
DOCTORAL PROGRAMME IN MECHANICAL ENGINEERING

ADVANCES IN LIFE PREDICTION AND DURABILITY OF RAILWAY AXLES

Doctoral Dissertation of:
Daniele Regazzi

Supervisor:
Prof. Stefano Beretta

Co-Supervisor:
Dr. Michele Carboni

Tutor:
Prof. Stefano Bruni

The Chair of the Doctoral Program:
Prof. Bianca Maria Colosimo

AY 2010-2013 – cycle XXVI

Abstract

This PhD thesis discusses some relevant topics for improving the design of railway axles, based on traditional fatigue concepts, to the novel damage tolerance approach.

Firstly an overview of the design methodologies adopted by the current regulations, using an infinite life concept, and by the safe life and damage tolerant approaches, pointing out the points still in discussion, is given, highlighting the importance of complementing the traditional approach with the novel damage tolerance.

Firstly, a series of VA tests under spectrum loading was carried out, in order to calibrate the allowable damage sum, then, a comparison of the results adopting the three design methodologies is presented, applied to the case of old axles no longer complaint with the current regulations. Realistic loading spectra were evaluated for the application of novel approaches; the allowable damage sum D, for the application of the safe life methodology, was set to the value estimated by the dedicated experiments onto small scale specimens. Limits and contradictions of the traditional approach are shown, and simple parameters, more representative of the expected lifetime, are presented and discussed.

The focus is then pointed onto two topics, still under discussion, which can affect the lifetime of real components: the effect of a compressive residual stress field, given by deep rolling, and the effect of variable amplitude loading onto crack propagation and inspection intervals.

The beneficial effect of the compressive residual stresses is studied by dedicated experiments, carried out onto three specially machined, and deep rolled, full-scale specimens, tested against crack propagation under variable amplitude loading. The lifetime increase due to deep rolling is shown, and compared against appropriate predictions, taking into account the presence of the compressive residual stress field. The study leads to the possibility of increase the expected lifetime, and, consequently, the distance between inspection intervals, for real axles, by extension of the results obtained from full-scale specimens.

Finally, the effect of variable amplitude onto crack growth retardation is addressed, by variable amplitude loading tests carried out onto four batches of medium strength (A4T) and high strength (34CrNiMo6 and 30NiCrMoV12) steel grades; both time history and equivalent load spectrum, eventually with different length of the blocks, are

applied, and both crack propagation and crack closure are measured along the tests. The experimental evidence is then compared against crack growth simulations, firstly adopting a simple no-interaction model, with thresholds from both CPLR and ΔK-decreasing methodologies, then by the more refined Strip-Yield model. A simple model, as a 'rule of thumb' for engineering lifetime calculation, is then presented and discussed.

Summary

Railway axles are components adopted since mid nineteen century and which have occupied and still occupy a large place in the scientific research. On one hand, they are safety components, whose failure can lead to tragic consequences, and are consequently designed with an infinite life approach; on the other one, there is an increasing needing of optimizing the costs and operations connected to the in-line inspections during the working life, especially considering the more recent applications to high-speed trains. Despite the great amount of studies, railway axles are nowadays still designed against fatigue limit and mostly based onto pregressed experience. By such approach, even if a high safety standard has been reached, it's not possible to make a step further in the direction of optimizing the design and all the costs related to production and exercise.

For this reason, the traditional design against infinite life is being more and more complemented by the relatively new, at least in the railway field, damage tolerant approach, able to take into account the degradation or damaging of the axle along lifetime. Several aspects contribute to a reliable estimation of the prospective lifetime and, consequently, a correct design and plan of the inspection intervals, such as the definition of the load history on the component, the mechanical properties and behavior to crack propagation of the adopted steel grade, the knowledge of the SIFs at the crack tip and the qualification of the NDT techniques adopted during inspections. Among these aspects, many points are still open, leaving a large amount of uncertainties onto the design process; a scientific effort is required in this direction.

Aim of this phD thesis was to point out the importance of moving the design to the novel damage tolerance approach, and focus onto two aspects reputed to have great importance upon the lifetime prediction of a railway axle: the effect of the compressive residual stresses and variable amplitude loading onto crack propagation, in the case of railway axles.

In particular, the present Ph.D. work has been developed as follows:

1. **Chapter 1: State of the art**. An overview of the literature is presented, giving an outline of the main arguments involved in the design of railway axles. The evolution of the design methodology is firstly shown, starting from the infinite life assessment, typical of the current regulations, through the adoption of damage sum criteria, ending in the increasing needing of the damage tolerant approach, not

yet well covered by the standards. From this approach, the knowledge of the stress history, residual stress field, the evaluation of the stress intensity factors along a crack and the behavior of a crack under constant and variable amplitude loading have to be known, as well as the performance of the non-destructive inspections adopted, in order to properly define appropriate inspection intervals for a given railway axle. The chapter highlights the open points that will be addressed in the thesis.

2. **Chapter 2: Variable amplitude fatigue assessment onto small-scale specimens**. The assessment of the fatigue life under variable amplitude, adopting damage sum calculations is considered in this part of the work. Several smooth small-scale specimens, made of A4T, are tested under variable amplitude loading. The choice of the allowable damage sum and the fatigue curve to be adopted for the calculations are discussed, by comparison of predictions against the experimental evidence. The parameters typically adopted in the present guidelines are compared with the results.

3. **Chapter 3: Fatigue Assessment of Axles with Old Design**. In this chapter, the lifetime extension of old axles, no longer complaint with the current regulations, is shown. This calculation, based on the damage tolerant approach, instead of the simple infinite life approach, gives the opportunity to compare the active European Standards for the assessment of railway axles. Limits and contradictions are shown, and simple parameters, more representative of the expected lifetime, are presented and discussed.

4. **Chapter 4: The effect of compressive residual stresses due to roll-forming onto fatigue crack propagation in railway axles**. The beneficial effect of the compressive residual stress field given by the deep rolling technological process has been studied in this chapter. Three full-scale specimens have been machined and subjected to deep rolling, then tested against crack propagation under variable amplitude loading. The lifetime increase due to deep rolling is shown, and compared against appropriate predictions, taking into account the compressive residual stress field. Finally, the increase of expected lifetime, for the case of a real axle is shown, extending the results obtained from full-scale specimens.

5. **Chapter 5: Load Interaction Effects in Medium and High Strength Steels for Railway Axles**. In the last chapter, the effect of variable amplitude onto crack growth retardation is addressed. Several variable amplitude loading tests have been carried out, onto four batches of medium strength (A4T) and high strength (34CrNiMo6 and 30NiCrMoV12) steel grades; both time history and equivalent load spectrum, eventually with different length of the blocks, are applied, and both crack propagation and crack closure are measured along the tests. The experimental evidence is then compared against crack growth simulations, firstly adopting a simple no-interaction model, with thresholds from both CPLR and ΔK-decreasing methodologies, then by the more refined Strip-Yield model. A simple model, as a 'rule of thumb' for engineering lifetime calculation, is then presented and discussed.

Contents

List of Figures

List of Tables

CHAPTER 1

State of the art

1.1 Evolution of the assessment of railway axles

Railway axles are safety critical components whose failure may result in derailments, with serious damage for the rolling stock and the infrastructure; it can cause injury to passengers and it can lead to casualties in the most serious cases. Therefore, axle resistance to failure is a key issue in designing and correctly maintaining railway vehicles, to ensure high safety standards and, at the same time, to optimize life-cycle costs from a system point of view. Railway axles are designed, manufactured and maintained so that they should not fail in service, usually targeting up to 40 years of service, or 10^7 km.

1.1.1 Infinite life assessment

The current regulations for the design of railway axles, active in the European Union, are EN13103 [1] and EN13104 [2], relative to trailer and motor railway axles respectively. These regulations, only dated 2001 and representing the infinite life design methodology, consider two steel grades, the low strength A1N (normalized C40 carbon steel) and the medium strength A4T (quenched 25CrMo4), typically adopted in Europe for the railway axles production. Calculations are carried out evaluating the stress state, along all the critical sections of the axle, due to the bending moments given a defined distribution of loads acting at the bearing journals, at the contact points between wheels and rails and on the brake disks; moreover, regarding the motor axles, the effect of traction is considered. Usually the service loads onto a wheelset are not well known, so EN13103/04 adopt a combination of loads onto the axle, chosen as representative of the most critical loading condition, only based onto pregressed experience. The design is then performed by a simple comparison of the stress state acting on the critical sections

of the axle against the Fatigue Limit of the involved material, opportunely reduced by a generous safety factor η, as in eq.(1.1), in order to take into account all the uncertainties about the working conditions of the wheelset during its life.

$$\Delta\sigma < \Delta\sigma_{design} = \frac{\Delta\sigma_{lim}}{\eta} \tag{1.1}$$

Regarding other steel grades, not covered by the Standards, simple relationship for evaluating the reduced fatigue limit are presented; typical examples of materials not covered, but widely used in Europe, are the 30NiCrMoV12 and the 34CrNiMo6 high strength steel grades, adopted for the production of railways axles for high speed applications (the 'Pendolino' train for the first and the ICE German train for the second one). An application of the lifetime assessment according to European Standard EN13104 will be shown in chapter 3.

1.1.2 Safe life assessment

Another approach for the railway axle design, according to the FKM guidelines [3], is the fatigue assessment adopting damage sum criteria derived from the concepts of damage accumulation originally due to Miner [4]. In particular, two approaches are proposed by the guidelines: the simplest is the Haibach model [5], identical to the original Miner's rule except that two regions of the fatigue curve are defined, the 'finite life' region (having slope m in the S-N diagram) and the 'infinite life' one (showing a $2m-1$ slope). The more complex approach, on the other hand, is represented by the Konsequent Miner's rule: when the component starts its service, under VA loadings, in the case the load spectrum contains some cycles above the (initial) endurance limit, these cycles will reduce it for a certain amount, and this process of reduction progressively increase while the damage rises; as a consequence of the phenomenon, continuing the VA loading, also the cycles of the spectrum initially under the endurance limit begin to contribute to the damage, till the damage sum reaches a critical value and the endurance limit gets zero.

A discussion is still open about the allowable damage sum index, relatively to the safe life assessment of railway axles: recent studies, by Grubisic and Fischer [6] indicate a value lower than the unity, suggested as $D = 0.5$ with calculations performed onto the mean fatigue life, while the FKM guidelines [3] suggest even more conservative values, fixed in an allowable damage sum $D = 0.3$, evaluated on the percentile $p_{2.5\%}$ of the fatigue curve. This was confirmed by further studies, in the WIDEM project [7], where an allowable damage sum $D = 0.1$, evaluated on the mean fatigue curve, was found; this assumption leads to calculations similar to those by the FKM guidelines, but only few specimens were adopted for the purpose. Even if these indications seem to agree, there is the needing of increasing the existing database in order to consolidate the value to consider as allowable damage sum.

1.2 Damage tolerance assessment

Despite infinite life is the methodology adopted for the design of railway axles, a few accidents have occurred in the past. In addition, this methodology is unable to take into account the deterioration of the axles during service, such as paint detachment, pitting

from corrosion [8] and damage from ballast impacts [9], as in Figure 1.1. All these kind of damage can act as an initiation of a fatigue crack, causing final fracture of the component.

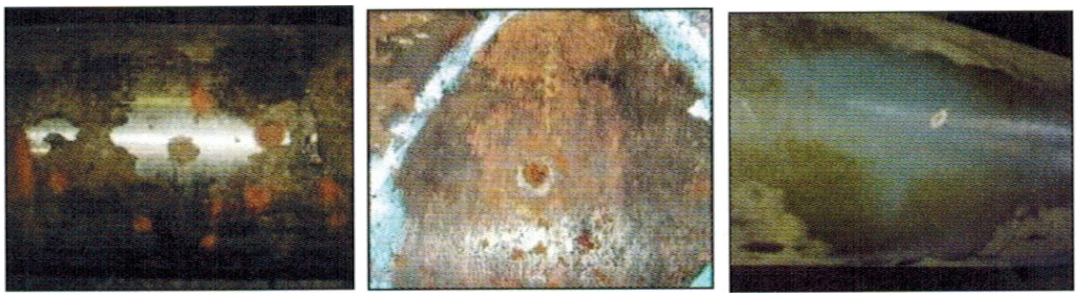

(a) Painting detachment (b) Corrosion pits (c) Damage from ballast impact

Figure 1.1: *Different kind of damaging of an in-service railway axle*

The traditional fatigue approach has to be complemented by a 'damage tolerant' approach, originally developed for aeronautic applications in the seventies [10, 11] and more recently introduced in the railway industry [12–14]. By this approach, it is assumed that a crack is present in the axle and it can grow during service; by appropriate analysis, the residual lifetime and, consequently, an adequate inspection plan, can be defined, in order to increase safety; a simple definition of the inspection interval, by which at least one possibility of detecting the crack during the axle's service is given, is shown in Figure 1.2.

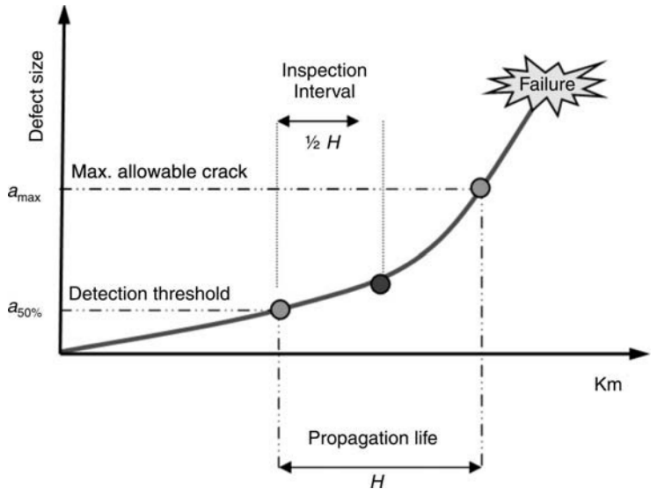

Figure 1.2: *Simple definition of the inspection interval, from the crack growth simulation, as H/2 [15]*

Other methodologies for the definition of the inspection intervals are based onto the probabilistic approach, for the definition of the probability of failure; this methods will be presented in the following sections.

Concerning the current regulations, only operative indications for the freight axles, regarding the distance between inspections, are present in the active guidelines, drafted

by VPI Germany, Austria and VAP Swiss [16]. These guidelines recommend, as general indication, that an inspection has to be carried out every 600000 km, controlling the axle by ultrasonic inspections. Relatively to the railway axles for freight wagons, a full inspection of the axle, including magnetic particles, is usually carried out each 1.2 millions km, when the wheels are re-profiled; intermediate inspections are carried out only adopting visual and ultrasonic inspections. It's worth to remark, here, that there is no Standard regarding the inspections of railway axle, but only guidelines about the freight wagons; the responsibility is totally demanded to the constructor and the maintenance service.

The knowledge of several factors is essential for a precise calculation according to the damage tolerant approach, resumed in Figure 1.3: the load spectrum acting on the axle during service, the crack growth behavior of the adopted steel grade, as well as the precise evaluation of the stress intensity factors along a crack have to be known, together with the performance of the non-destructive technique (NDT) adopted during in-line inspections, by which the initial flaw size, for the calculations, is decided.

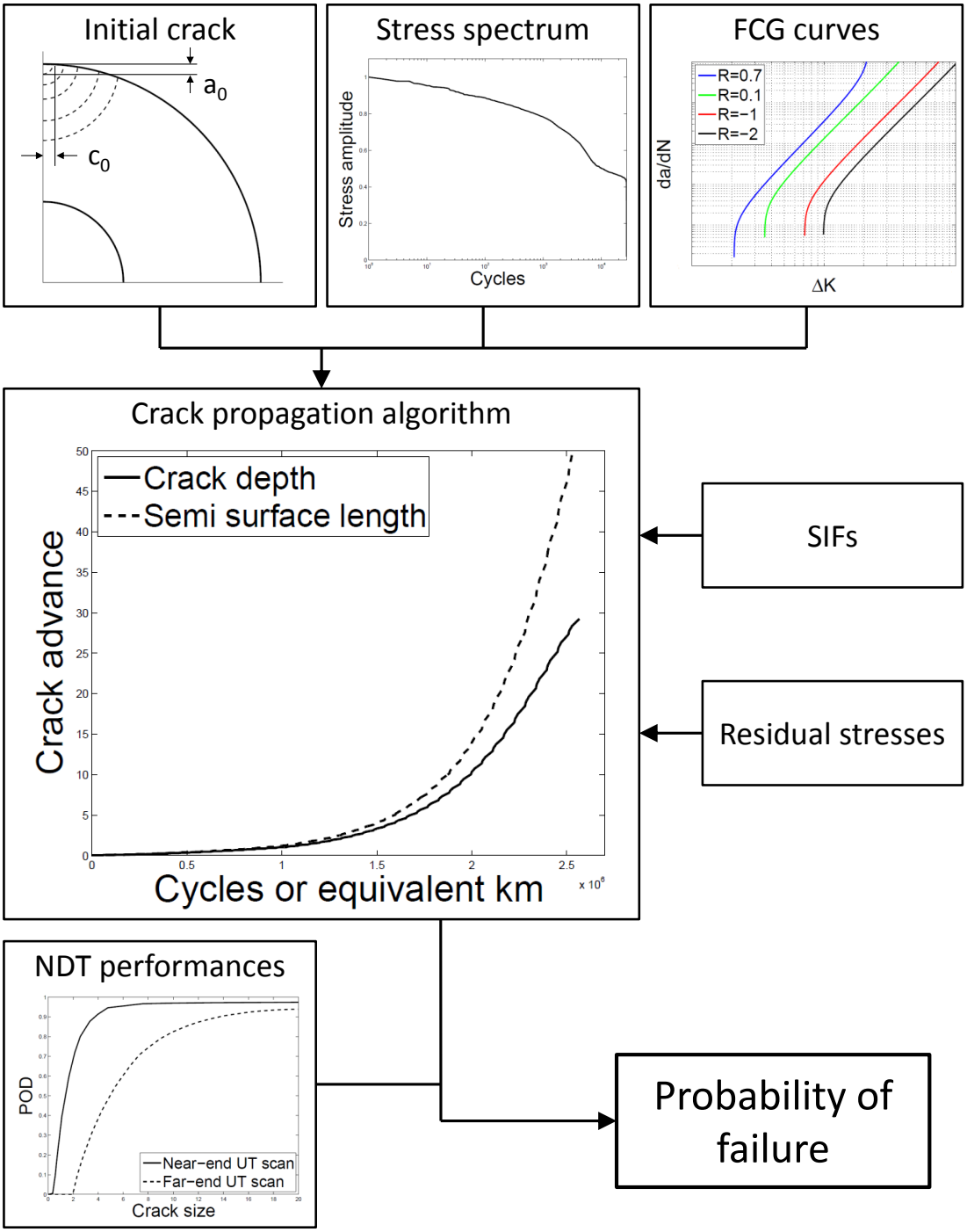

Figure 1.3: *Overview of the structural integrity assessment for a railway axle*

1.2.1 NDT Reliability

Even if the current regulations, for the railway axles, adopt an infinite life design, the wheelset, during service, can be subjected to deterioration, due to corrosion, loss of paint or damage from ballast impact. For this reason it is necessary to establish a plan of periodic non-destructive inspections during the service of the vehicle, in order to be able to detect damaging and prevent failures of the component. The most common methods for inspecting railway axles are visual testing (VT), Ultrasonic Testing (UT) and magnetic particle testing (MT). These inspections are usually scheduled based onto pregressed experience; only recently a more ingegneristic approach is starting to be applied from the operators of the sector.

The knowledge of the performances of the NDT techniques adopted is essential for establishing the plan of the periodic inspections, adopting a more sophisticated probabilistic approach, in order to guarantee structural integrity during the life of the railway axles. In fact, NDT reliability is a statistical matter [17], and the parameter usually adopted for its reliability is the probability of detection curve; Figure 1.4b reports the POD curve, by Benyon and Watson [18], widely adopted in the railway axle field, considering the case of MT inspections and UT from 'near-end' and 'far-end' scans, defined for a solid axle in Figure 1.4a. Regarding hollow axles, similar POD curves were recently derived in the frame of research activities carried out at PoliMi [15].

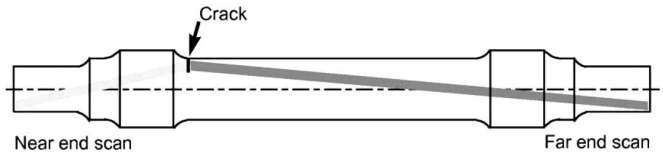

(a) Definition of 'near-end scan' and 'far-end scan' UT techniques

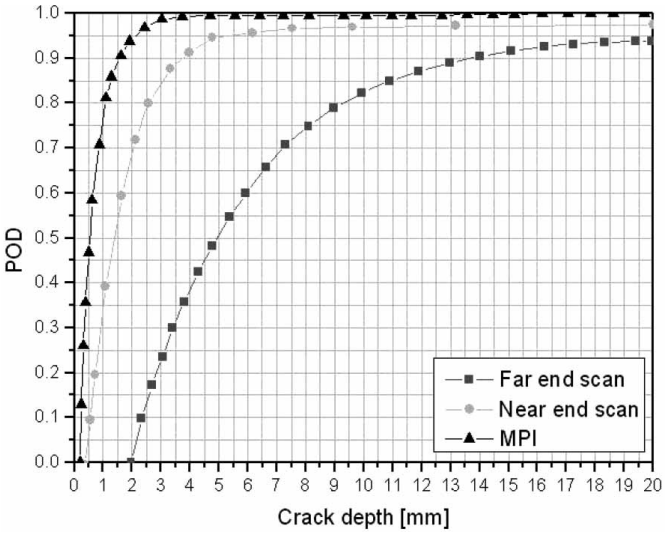

(b) POD curves for typical railway NDT technologies

Figure 1.4: *POD for a typical railway axle, according to Benyon and Watson [18]*

As can be noticed from Figure 1.4b, MT inspections are the more powerful in the detection of small cracks, able to detect a 0.5 mm flaw, with the 50% of probability,

followed by the 'near-end' scan (1.5 mm detectable with 50% probability) and 'far-end' scan respectively (about 5 mm detectable with 50% probability). Usually [16] MT are performed only when the wheels have to be re-profiled or substituted (typically every 1.2 millions km, according to [16]), so only UT is applied during intermediate inspections, with lower probability of detection of small flaws. POD curves allow the estimation of the largest defect that can be missed, more important that the smaller defect that can be detected, from the damage tolerant point of view [19]; usually POD curves are given with an appropriate lower confidence limit, typically 95%.

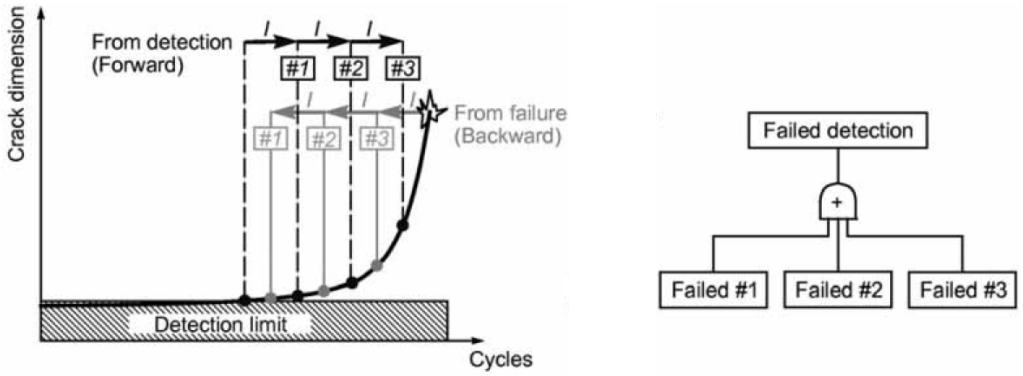

(a) Definition of 'forward' and 'backward' inspections

(b) Fault tree of the inspection

Figure 1.5: *Calculation of the cumulative probability of detection [20]*

It is desirable that the inspection method is planned in order to have the possibility to observe the axle more than once prior to failure; consequently, the probability of detection of the eventual crack is not the POD during one single NDT control, but has to be evaluated, once fixed the distance between inspections, as a function of the crack size development and the POD curve of the adopted NDT. Figure 1.5a [20] reports one case of NDT plan, considering three inspections along the life of the railway axle; the two approaches based on 'forward', starting from the limit of detectability of the crack, and 'backward' detection, going back from final failure, are shown. While the first one seems to be the natural choice, with the second one only to be adopted in a trial given a real accident, in order to assign responsibilities, the latter is the most adopted in the design of the inspection intervals, because it is less conservative. The cumulative probability of detection (PC_{DET}) of the crack can be evaluated as:

$$PC_{DET} = 1 - \left[\prod_i POND(a)_i\right] = 1 - \left\{\prod_i \left[1 - POD(a)_i\right]\right\} \tag{1.2}$$

where $POND(a)_i$ and $POD(a)_i$ are the probability of non detection and the probability of detection, respectively, at the i_{th} inspection, when the crack size is a_i. The probability of failure P_f, given that all the inspections failed to detect the crack, as in Figure 1.5b, can be calculated, given PC_{DET}, as:

$$P_f = 1 - PC_{DET} = \prod_i POND(a)_i = \prod_i \left[1 - POD(a)_i\right] \tag{1.3}$$

Another method for the evaluation of the probability to failure, originally proposed for application in the railway axle field [12], is the so-called 'last chance' detection, represented in Figure 1.6.

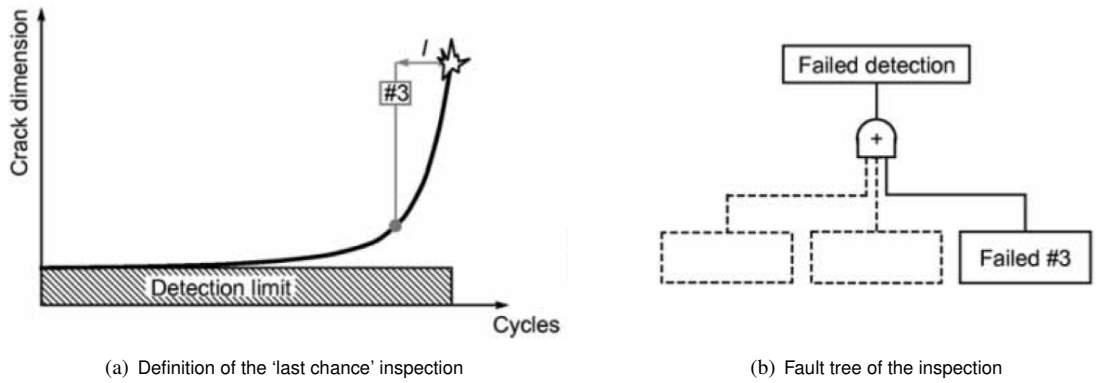

(a) Definition of the 'last chance' inspection

(b) Fault tree of the inspection

Figure 1.6: *Probability of detection for the 'last chance' method [20]*

This methodology is intended to avoid the error amplification characteristic of the first method, due to the fact that in the near-detection area the PC_{DET} is really low. By the 'last chance' method, only the last detection is considered (in the backward direction); the probability of detection is evaluated as:

$$P_{DET} = POD(a)_{max(i)} \tag{1.4}$$

and the probability of failure becomes:

$$P_f = 1 - P_{DET} = 1 - POD(a)_{max(i)} \tag{1.5}$$

Regarding the damage tolerant approach, applied to railway axles, the discussion is still open. A comparison of this relatively new methodology against what is prescribed by the current regulations (infinite life approach) and against the safe life approach, according to the damage sum, are still under discussion and will be covered in the present research.

1.3 Service load assessment

Important inputs for the fatigue analysis and the damage tolerant assessment, according to Figure 1.3, are load spectra, i.e. the occurrence distribution of stress amplitudes at each critical section along the axle, that depend on the railway line, the vehicle characteristics and the loading conditions. Load spectra, which act as an input for the fatigue life or crack propagation assessments, can be evaluated by both experimental, using instrumented wheelsets running in-line, or numerical approaches, by the meaning of dedicated Vehicle Multi body simulations.

1.3.1 Experimental approach using an instrumented wheelset

Regarding the experimental methodology, strain measurements are usually performed on the axle and the wheel during the first in-line tests for the qualification of a new

vehicle; this kind of measurements are traditionally made to verify that the derailment limit Y/Q (Nadal's limit [21]) is never reached; more than this, dedicated experimental campaigns, using instrumented wheelsets, as in Figure 1.7, can be carried out for the evaluation of the contact forces.

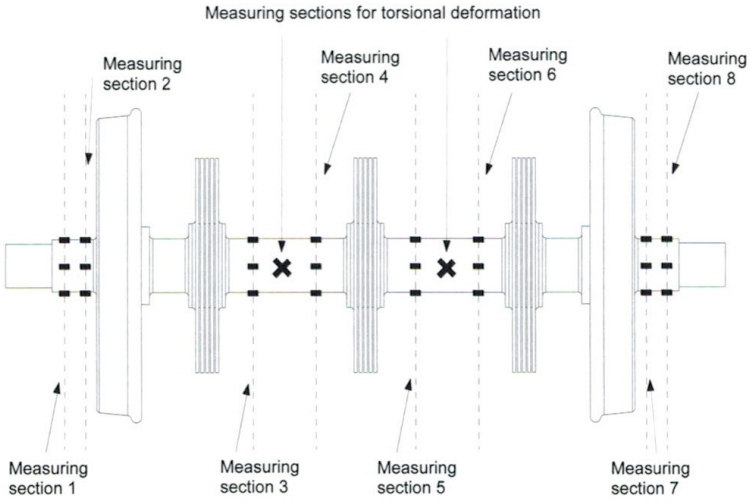

Figure 1.7: *Example of instrumented wheelset*

The basic assumption of the methodology is that there is a linear relation between the bending and torsional deformations of the wheelset and the contact forces. The instrumented wheelset has firstly to be calibrated, imposing a combination of lateral force, yaw angle and load transfer to the wheelset, then it can be mounted on a vehicle and travel along the line. Wheel-rail contact loads are derived, from strain gage measurements, given the knowledge of the axle's geometry. Load measurements are also a fundamental reference for the validation of multi-body models of the vehicle and their extension to different loading conditions, i.e. curve parameters, vehicle payloads and wheel profile.

1.3.2 Numerical approach by Vehicle Multi body simulation

A multi-body modeling approach for the study of the running behavior of railway vehicles was recently developed by the Dynamics Research Group at PoliMi [22]. The model, allowing to analyze the non-stationary running behavior both in straight and curved track of a single railway vehicle, is based on a multi-body schematization of the trainset, divided into elementary modules of the following types:

1. carbody, modeled as a single rigid or flexible body;

2. bogie assembly, connected by primary suspensions to the wheelsets;

3. secondary suspensions, modeled as a combination of lumped parameter viscoelastic elements, possibly including specific models with internal state variables to reproduce the frequency dependent behavior of special suspension components such as airsprings;

which can be combined in order to reproduce a wide range of vehicles. Each rigid body is assigned with 5 degrees of freedom: vertical and lateral displacements, yaw, pitch and roll rotations. For each flexible body, a modal superposition approach is adopted, by which the vibration of the body is described as the linear combination of the rigid and flexible modes of vibration of the free body.

The equations of motion of the vehicle take the form:

$$M_v\ddot{x}_v+C_v\dot{x}_v+K_vx_v = F_e(V,t)+F_i(V,t)+F_{nl}(x_v,\dot{x}_v)+F_{cv}(x_v,\dot{x}_v,x_t,\dot{x}_t,V,t) \quad (1.6)$$

where M_v, C_v and K_v are the mass, damping and stiffness matrices of the vehicle respectively, x_v is the coordinates vector, F_e is the vector of generalized forces produced in the secondary suspensions by the different motion of the moving references associated with the modules connected by the suspensions, F_i is the vector of inertial forces due to the non-inertial motion of the moving references, F_{nl} is the vector of non-linear forces due to non-linear elements in the suspensions and F_{cv} is the vector of generalized forces due to wheel-rail contact, depending upon the motion of the trainset x_v, $\dot{x}_v$ and upon additional coordinates x_t and $\dot{x}_t$, representing track motion and their time derivatives. The dynamic behavior of the track being negotiated by the train is represented by the additional equation:

$$M_t\ddot{x}_t + C_t\dot{x}_t + K_tx_t = F_{ct}(x_v,\dot{x}_v,x_t,\dot{x}_t,V,t) \quad (1.7)$$

where M_t, C_t and K_t are the track mass, damping and stiffness matrices, respectively, and F_{ct} is the vector of generalized forces acting on the track due to wheel rail contact forces. The model of wheel-rail contact is a pre-tabulated multi-Hertzian one, taking into account the contact angle and the wheel and rail profiles [23]. Full details about the calculation of wheel-rail contact forces are given in [24].

The contact forces are then transformed to the global reference system, and the vectors of generalized forces F_{cv} and F_{ct} of eqs.(1.6) and (1.7) are derived. Eq.(1.8), valid for both rigid and flexible wheelset models, is obtained applying the principle of virtual works:

$$F_{cv} = \sum_{j=1}^{n_w} \Phi_j^T F_j \quad (1.8)$$

where n_w is the number of wheelsets. The contact forces act as a coupling term between the vehicle equation of motion (eq.(1.6)) and the track equation of motion (eq.(1.7)); these two equations are simultaneously integrated using a modified Newmark time-step procedure, by which, at each integration step, convergence is reached iteratively.

In Figure 1.8 is shown an example of validation tests of the multi-body model here presented, carried out during the European WIDEM project [7, 25].

1.3.3 Evaluation of the spectra from time history loading

The rainflow-counting algorithm (also known as the 'rain-flow counting method') is used in the analysis of fatigue data in order to reduce a stress time history into a set of stress amplitudes. Its importance is that it allows the assessment of the fatigue life

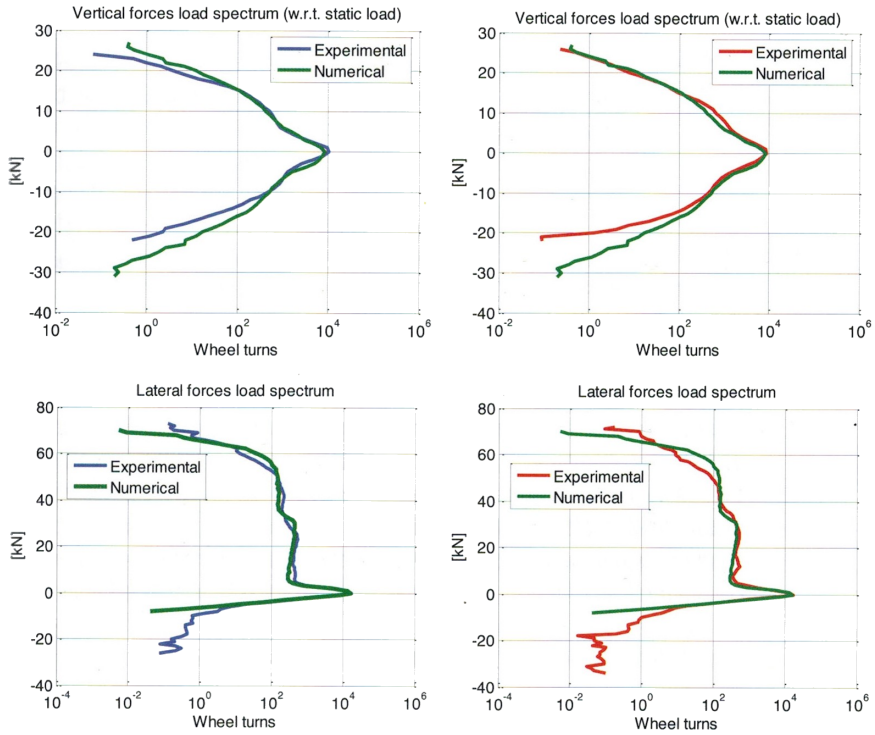

Figure 1.8: *Comparison between measured and simulated load spectra of the vertical and lateral contact force components for the two wheels on the Česká Třebová - Břeclav line [25]*

of a structure subject to complex loading. The problem of correctly counting the fatigue cycle a component was subjected to was firstly experienced in the aeronautical field, and led to the rainflow algorithm, proposed by Tatsuo Endo and M. Matsuishi in 1968 [26], for the evaluation of the spectrum. The stress spectrum is a schematic representation of the whole stress amplitudes experienced by the component: the plot, in a semi-logarithmic scale, reports, in a descending order, the stress amplitudes against the cumulative sum of the cycles. This permits to quickly recognize the maximum stress amplitude $\sigma_{a,max}$ and the total number of fatigue cycles N_{max}. The rainflow cycle-counting algorithms was included as one of many cycle-counting algorithms in ASTM E 1049-85 [27].

1.4 SIF evaluation

The Stress Intensity Factor (SIF) is the parameter characteristic of the local stress at the crack tip, function of the crack size a, the nominal stress σ and the adimensional shape function Y, only dependent upon the geometry of the cracked component, as shown in eq.(1.9). Given that the crack size is measurable and the nominal stress state can be evaluated from the loads estimation, the shape function Y is the only unknown parameter of eq.(1.9).

$$\Delta K = Y \Delta\sigma \sqrt{\pi a} \tag{1.9}$$

The carefully estimation of the SIF, which is a crucial operation in the frame of

the damage tolerant assessment, is so related to an accurate evaluation of the shape function Y, given the shape and dimension of the crack relatively to the component. The shape functions are usually evaluated adopting two families of methodologies: one based onto FE modeling of the cracked component, the other one onto an analytical calculation adopting the so-called weight's functions.

1.4.1 FE methodology

SIFs can be evaluated by dedicated FE models, carried out adopting commercial software; most of the commercial software available, in fact, have some plugin for the crack modeling; the evaluation of the stress intensity factors, along the crack itself, based on the J-integral determination, using the method of virtual crack extension and domain integrals [28]. Figure 1.9 [29] shows a typical finite element model used for the evaluation of the SIFs of a semi-elliptical crack inserted in the S-transition of a hollow axle.

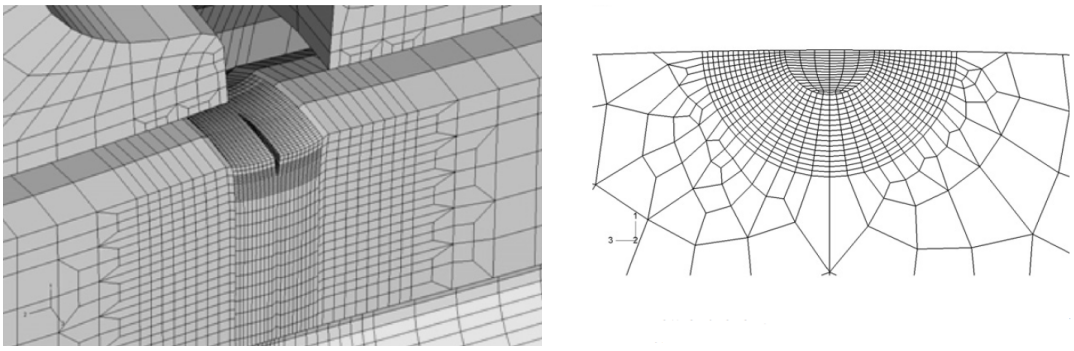

(a) Detail of the FE model

(b) Detail of the mesh refinement around the crack

Figure 1.9: *Example of FE model of a crack inserted in the 'S-transition' of a railway axle [29]*

Great care has to be put to the mesh refinement around the crack surroundings, as in the example of Figure 1.9b: the mesh have to be refined in the proximity of the transition regions, whereas a quite coarse mesh can be adopted elsewhere. This is of great importance, since the J-integral, adopting the domain integrals methodology, is evaluated at fixed contours around the crack tip; the convergence of the results can only be obtained adopting an opportunely refined mesh. Results from FE calculations, using several crack shapes and dimensions, are usually interpolated, in order to obtain an analytical solution for the SIF of a developing crack; an example of interpolation, including the effects of rotating bending and press-fit, is shown in [30].

1.4.2 Weight function methodology

The FE methodology, applied to the evaluation of the SIFs, gives very precise results, but the computational effort, due to the fact that several crack shapes and dimensions have to be modeled, is very high. Moreover, the FE methodology is not flexible: apart from the analyzed cracks, the results cannot be easily extended. There is the need to generate SIFs solutions by the meaning of more fast and flexible numerical tools, which

can be found in the weight functions, widely available in the literature [31] for different cracked components under various stress state.

The case of a cracked railway axle is not directly covered by the existing weight functions; what is usually done is considering a solution valid for a case similar in both the geometry and the loading conditions. The most adopted weight function, in the case of a cracked railway axle, is the Wang and Lambert approach [32] for a thick plate, represented in Figure 1.10.

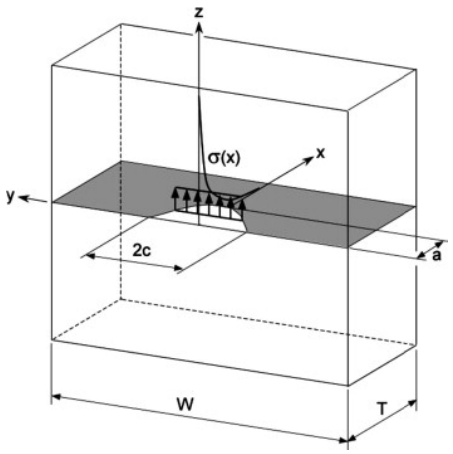

Figure 1.10: *Geometry for the weight function approach according to Wang and Lambert [32]*

The width of the plate (W) is fixed at the diameter D of the axle, while the thickness t is set as the diameter D, in the case of a solid axle, or as the wall thickness $D_e - D_i$ in the case of a hollow axle. The stress distribution, given all the contributions due to the stress concentration and the residual stresses due to press-fit, are approximated by a polynomial function, with a maximum exponent equal to 4, as in eq.(1.10).

$$\sigma(x) = \sum_{i=0}^{4} \sigma_i \left(1 - \frac{x}{a}\right)^i \tag{1.10}$$

The stress intensity factor K, given the stress field, is evaluated as:

$$K = \int_0^a \sigma(x) \cdot M(x, a) dx \tag{1.11}$$

where $M(x, a)$ are the weight functions suggested by Wang and Lambert and collected in [32]. This approach is applicable, in the original formulation, to cracks in the range $0 \leq a/T \leq 0.8$ and showing a low aspect ratio ($0 \leq a/c \leq 1$).

When the application is transferred to cracks in railway axles, the applicability range slightly changes, as was proved in [30]. The stress intensity factor at the deepest point of the crack was well represented in all the considered cases; on the contrary, SIFs at the surface points were correctly evaluated only for cracks with a/c ratios close to one, while for flatter cracks the approach overestimated the results obtained from FEM. It has to be remarked that cracks initiated from ballast impacts usually show an a/c ratio lower than the unity [33]; the approach, in this case, is conservative regarding the predicted lifetimes.

1.4.3 Effect of the rotary bending onto SIFs

As shown in Figure 1.11, the relative position of the surface crack, against the maximum bending moment, changes during one cycle, due to the rotation of the axle. The stress intensity factor at point B (K_B) is higher in rotating bending than in reverse plane bending, reaching the maximum value at the angle θ_0, which depends on the crack size.

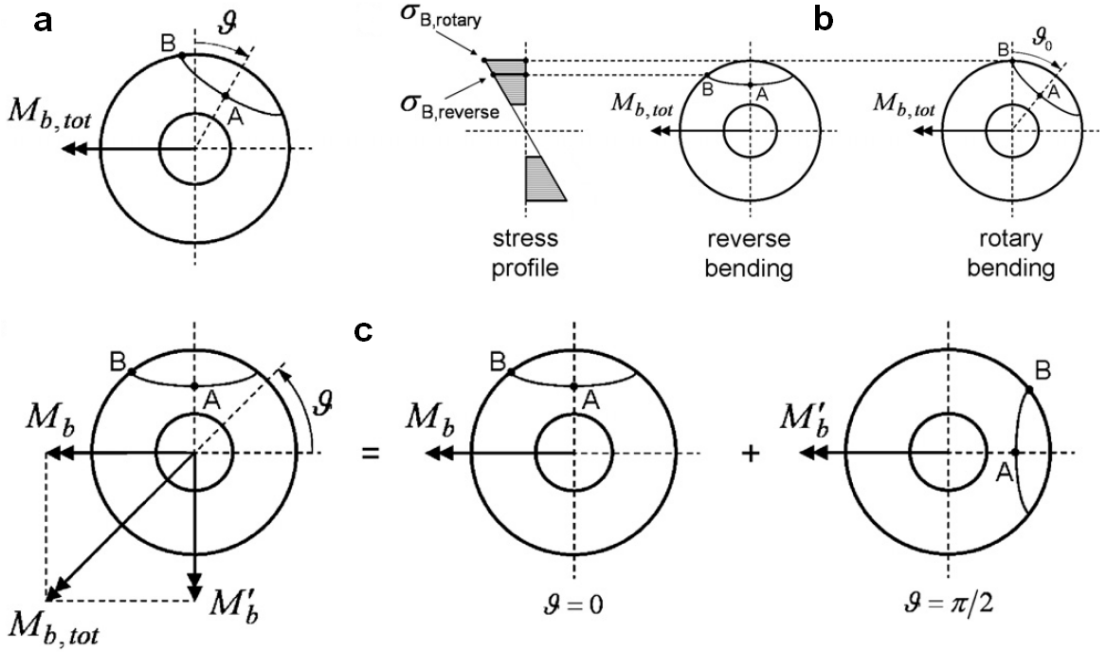

Figure 1.11: *Schematic of rotary bending: a) rotation of the axle; b) difference between reverse and rotary bending; c) decomposition of the $M_{b,tot}$ in the two components M_b (crack at $\theta = 0$) and M'_b ($\theta = \pi/2$) [29]*

An analytical approach, considering the effect of rotary bending onto SIF evaluation at the crack tip, was proposed, for a generic cracked rotating shaft, by Carpinteri [34], who derived the solution by superposition of the two SIFs evaluated at point B in the two plane bending positions at $\theta = 0$ and $\theta = \pi/2$ visible in Figure 1.11c, according to eq.(1.12):

$$\begin{cases} K_A = (F_A \cdot \sigma_{nom} \cdot \sqrt{\pi a})\, cos\theta \\ K_B = (F_B \cdot \sigma_{nom} \cdot \sqrt{\pi a})\, cos\theta + (F'_B \cdot \sigma_{nom} \cdot \sqrt{\pi a})\, sin\theta \end{cases} \tag{1.12}$$

where F_A and F_B are evaluated at $\theta = 0$ and the term F'_B is evaluated at $\theta = \pi/2$. When the crack overcome a given size (typically 15% of the diameter of the axle D), the difference between plane and rotary bending become important, with K_B values significantly higher in the rotary bending condition. The correct evaluation of the K_B stress intensity factor is of crucial importance, because the crack shape changes from the plane bending condition; as was confirmed by experimental investigations [35, 36], rotary bending leads to a flattening of the crack.

1.5 Residual stresses

Another crucial point in the SIF evaluation of a crack inserted in a railway axle is the effect of the residual stresses, typically generated from press-fitting of the wheels, disks and gears. A transition is required (T-transition for wheels and disks and S-transition for gears [37]) close to the seats of the axle, generating a stress concentration due to the local geometry; due to the stress concentration factor, a higher probability of developing a crack arises in these areas, also affected, moreover, by the tensile stress state due to the press-fit contribution.

The contemporary effect of rotating bending and press-fit onto a crack in a railway axle was analytically studied by Madia et al. [29], who improved the solutions proposed by Carpinteri [34], already taking into account the rotating bending effect, by adding a mean contribution to the SIFs at the points A and B ($\bar{K}_A$ and $\bar{K}_B$), due to press-fit, as in eq.(1.13). The methodology was based onto FE models of the cracked axle.

$$\begin{cases} K_A = \left(K_A - \bar{K}_A\right) cos\theta + \bar{K}_A \\ K_B = \left(K_B - \bar{K}_B\right) cos\theta + \left(K'_B - \bar{K}_B\right) sin\theta + \bar{K}_B \end{cases} \tag{1.13}$$

The effect of the tensile residual stresses onto the SIF of the crack is smaller than the effect of rotating bending, which contributes the most; this is due to the fact that the maximum tensile stress due to press-fit is much lower than the stress due to rotating bending. In particular cases, especially when the stress concentration is very severe (i.e. in the S-transitions [37]), the effect of press-fit, which, as shown in Figure 1.12a, acts as a mean stress, is not negligible.

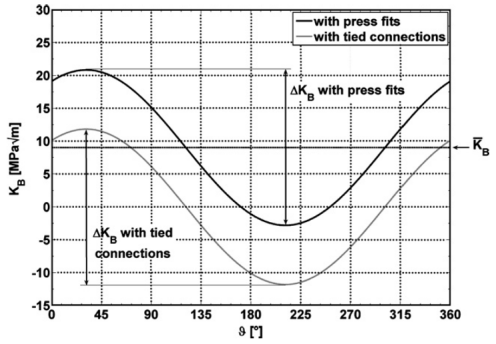

(a) Influence of the press fits on the crack front loading during crack growth, compared to the condition with simple tied connections

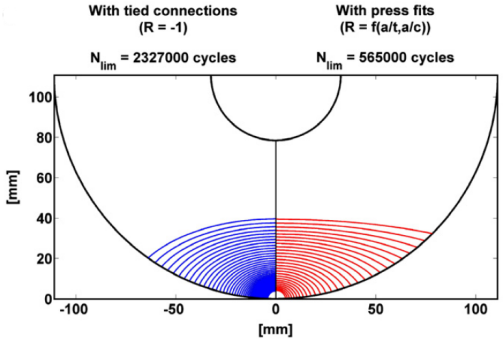

(b) Influence of the press fits on the propagation of a initially semi-circular crack with a/t = 0.05: evolution of the crack shape

Figure 1.12: *Effect of rotating bending and press-fit onto SIFs and crack shape [29]*

More than the detrimental effect to crack propagation, reducing the residual lifetime, due to the presence of a residual tensile stress field, the opposite case is of more practical interest, for a mechanical component; the presence of compressive residual stresses, in fact, can increase lifetime by reducing the SIFs experienced by the crack. In fact, considering methods to improve the crack growth life of mechanical components subjected to fatigue, several surface mechanical procedures, such as shot peening, have

been more and more adopted [38–40] over the last few decades, to increase their service durability and reliability. The beneficial effects onto fatigue life of the compressive residual stresses, due to surface technological treatments, is well known from the literature [41–44]. From a fracture mechanics point of view, a few investigations, trying to quantify the effect of retardation onto cracks in specimens made of aluminum and steel, are available in literature [45–47], while no investigations have been found about the effects of compressive residual stresses onto fatigue crack growth in real components.

Especially considering railway axles, the technological process traditionally adopted by axle producers for the life extension is deep-rolling [48]; the roller translates along the whole surface of the axle or just along those regions where compressive residual stresses are required. The relevant technological parameters, depending on the desired magnitude of residual stresses and their maximum depth, are the geometry of the roller at the contact region, the longitudinal feed (i.e. the step of advancement along the axle) and the applied contact force [48].

A complete set of solutions was presented by Madia et al. [30] for solid and hollow axles, presenting cracks at the T- and S-transitions; solutions, based on eq.(1.13), were compared against other solutions from literature.

Another recent work of Lebahn et al. [49] compared different approaches for the evaluation of the stress intensity factors in the case of railway axles; several solutions were prepared, by different partners, adopting both methods based onto FE and weight functions. In particular, the Shiratori weight functions, that will be adopted during the present research, were successfully compared against the other methodologies, returning in a good agreement.

1.6 Stable propagation of fatigue cracks

In the case of ‘long cracks’, where long means that the dimension of the crack is much higher than the plastic radius at the crack tip, the Linear Elastic Fracture Mechanics (LEFM) is applicable, otherwise, for ‘short cracks’, the Elasto-Plastic Fracture Mechanics (EPFM) [50] is required. The focus is here pointed only onto the LEFM approach, since, usually, the considered dimension, for cracks included in a railway axle, corresponds to long cracks, with dimension of few millimeters, in dependence of the considered non-destructive technique (NDT) for crack detection in service.

1.6.1 Crack closure phenomenon

At the end of the sixties, Elbert [51] discovered that the two faces of a crack, subjected to fatigue loading, closed before the load went to zero, i.e. the crack was already closed when the stress was still positive in tension. This phenomenon, schematized in Figure 1.13, which could not be explained by the theory of elasticity, could be explained by thinking that a local plastic deformation arises at the crack tip, due to loading conditions.

The plastically deformed area is formed at the crack tip, leaving a wake of plastically deformed zone along the crack length; this zone shows residual compressive stresses, induced by the elastic and plastic deformation of the material during unloading. During the following cycle, while loading, the crack tip does not open unless the applied load

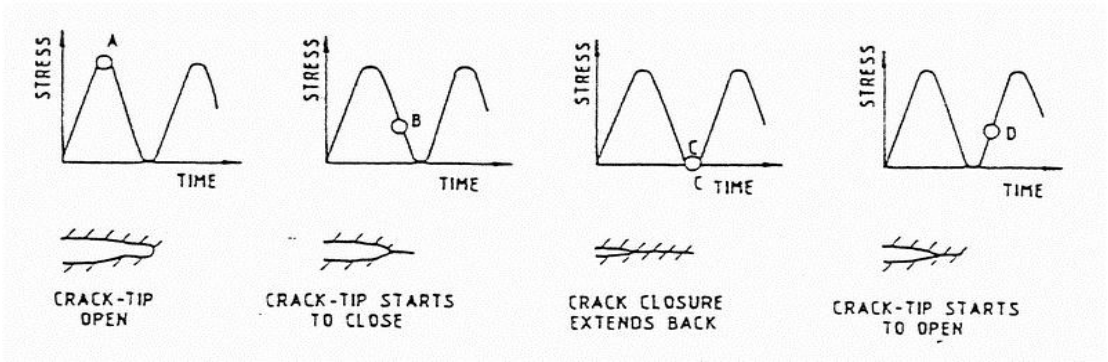

Figure 1.13: *Plasticity induced crack closure [52]*

is high enough to overcome the residual compressive stress present in the plastic wake zone.

Since the crack tip resents of the stress intensity factors only if the crack is fully open, Elbert proposed an 'effective' amplitude of the stresses (or of the SIFs), considering only the portion of the cycle in which the crack was fully open, as in eq.(1.14).

$$\Delta S_{eff} = S_{max} - S_{op} \quad \Longleftrightarrow \quad \Delta K_{eff} = K_{max} - K_{op} \tag{1.14}$$

This equation intrinsically takes into account the stress ratio R, since the reversed plastic zone, at the crack tip, depends upon the minimum stress S_{min}. Moreover, the S_{op} value does not depend on the crack length, but only on the cyclic stress applied; Elbert proposed the U parameter, in eq.(1.15), which represents the percentage of the SIF (or stress) range during which the crack is fully open.

$$U = \frac{\Delta K_{eff}}{\Delta K} = \frac{\Delta \sigma_{eff}}{\Delta \sigma} \tag{1.15}$$

The most adopted formulation of the U parameter is due to Schijve [53], who proposed the formulation of eq.(1.16) in order to take into account the effect of crack closure at negative stress ratios; this equation is valid in the $-1 \leq R \leq 0.54$ range.

$$U = 0.55 + 0.33R + 0.12R^2 \tag{1.16}$$

It can be deduced that the higher the closure effect, the lower is the U value, and the lower is the crack growth rate, since the crack remains open for a lower portion of the cycle. The plastic wake, and consequently the crack closure are influenced by the stress ratio: above R=0.54, U tends to one, and for R $\geq$ 0.75 it can be said that the crack is fully open during a load cycle. Following Elbert's concept, the fatigue crack growth rate is a function of the effective SIF only (ΔK_{eff}); adopting ΔK_{eff} instead of ΔK, crack growth curves at different stress ratios collapse onto the 'effective' one, as shown in Figure 1.14.

Many other mechanisms exist besides plasticity-induced crack closure (i.e. roughness-induced, oxide-induced and many other [37]), which can play a significant role especially in the near-threshold region.

The most commonly used methods for experimentally evaluate the crack closure can be divided in two main categories: 'global compliance' methods and 'local compliance'

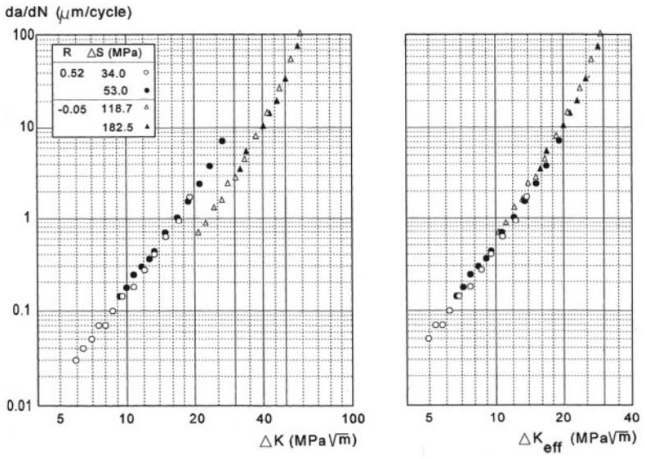

Figure 1.14: *Crack propagation curves, for an aluminum alloy at different stress ratios, represented as function of ΔK and ΔK_{eff} [54]*

ones. Among the first methods are the measurements by Clip-Gage at the crack mouth or Back Face Strain Gage (BFS) [55], as in Figure 1.15, while the latter are based onto a more precise evaluation of the local strain field, measured by dedicated strain-gages in the vicinity, or across the crack tip; examples of this methods can be found in [56, 57].

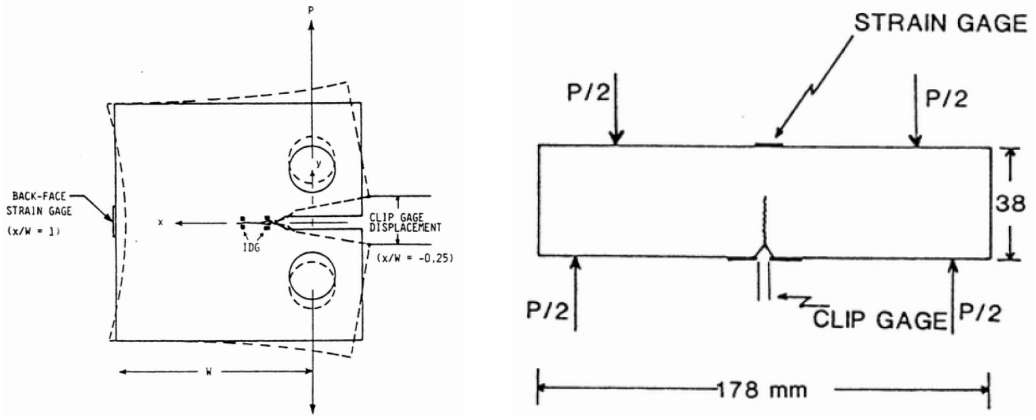

(a) C(T) geometry (b) SE(B) geometry

Figure 1.15: *Measurements taken from Back-Face Strain-Gage (BFS) or Clip Gage across the crack mouth [55]*

Numerical procedures for the crack closure measurement are shown in Figure 1.16. In particular, Figure 1.16a reports the evaluation of the closure by the global load-strain method, as in [55], Figure 1.16b shows the calculations carried out adopting the proposed 'compliance offset method', explained in [58], while the remaining two plots are relative to the 'local methodology', where the load-strain hysteresis cycle at the crack tip (Figure 1.16c) is conveniently amplified into a load-strain offset one (Figure 1.16d), for a more precise crack closure evaluation [59].

Regarding the 'global' methods, the P_{op} value (which is easier to determine than the opening stress value S_{op}) is evaluated by noticing that the load-strain curve behavior

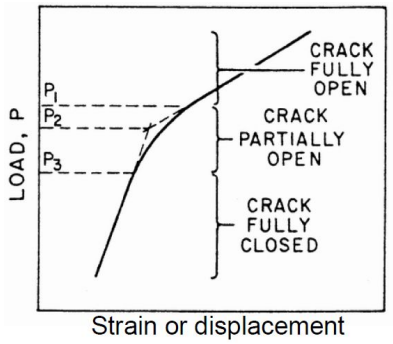

(a) Load-strain curve by 'global' method [55]

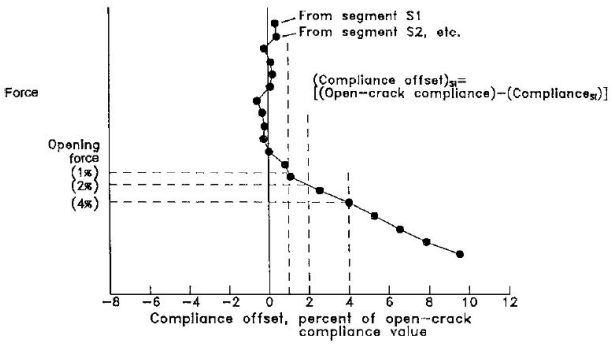

(b) Compliance Offset method (global method) [58]

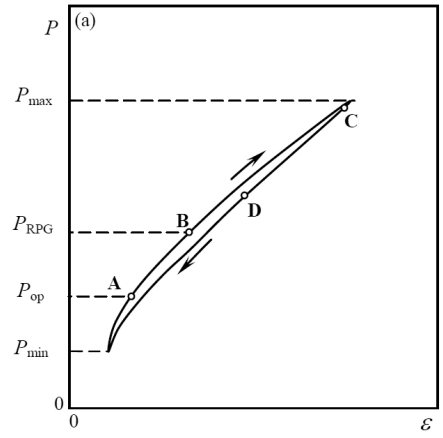

(c) Load-strain cycle by 'local' method, adopting strain gages [59]

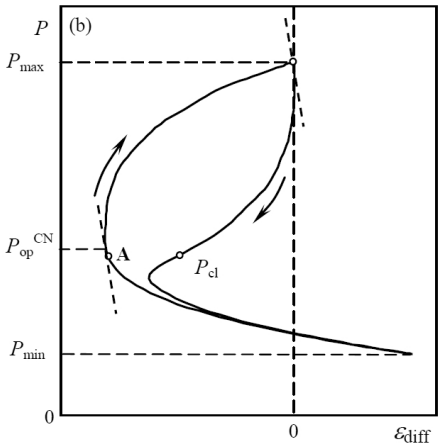

(d) Load-strain Offset cycle [59]

Figure 1.16: *Crack closure measurements*

is linear when the crack is fully open and non-linear when it starts to close; regarding the compliance offset method, the crack is conventionally marked as 'open' at the force value in which the line assumes a value of compliance offset equal to the offset criterion (usually at 2%). Regarding the 'local' methods, the original procedure by Chen and Nisitani [59] was conveniently modified by Toyosada and Niwa [60], for the evaluation of the opening (P_{op}) and closing (P_{cl}) points of the cycle: P_{cl} is evaluated as the flexing point of the unloading branch of the hysteresis load-strain offset curve, while P_{op} is the point, in the loading branch of the curve, showing the same slope of the closing point, as in Figure 1.16d.

More than these mainly adopted methods, for the crack closure evaluation, based onto a load-strain cycle, other methodologies have been adopted in the years. Among them it is worth remembering methods based onto optical interferometry [61], thermography [62] or ultrasonic measurements [63].

1.6.2 The Nasgro equation

The state of the art, for the crack growth rate evaluation, is represented by the so-called Nasgro equation, initially documented by Forman and Mettu [64]; the equation,

representing all the three regions of the FCG diagram, is:

$$\frac{da}{dN} = C\left[\left(\frac{1-f}{1-R}\right)\Delta K\right]^n \frac{\left(1-\dfrac{\Delta K_{th}}{\Delta K}\right)^p}{\left(1-\dfrac{K_{max}}{K_c}\right)^q} \tag{1.17}$$

where N is the number of applied fatigue cycles, a is the crack length, R is the stress ratio, ΔK is the stress intensity factor range, C, n, p, and q are empirically derived constants, $\Delta \mathrm{K}_{th}$ is the threshold stress intensity factor and K_c is the critical SIF. The parameter f, taking into account the plasticity-induced crack closure, was defined by Newman [65] as:

$$f = \frac{K_{op}}{K_{max}} = \begin{cases} max\left(R, A_0 + A_1 R + A_2 R^2 + A_3 R^3\right) & \text{if } R \geq 0 \\ A_0 + A_1 R & \text{if } -2 \leq R < 0 \end{cases} \tag{1.18}$$

where the coefficients are evaluated as:

$$\begin{aligned} A_0 &= \left(0.825 - 0.34\alpha + 0.05\alpha^2\right)\left[cos\left(\frac{\pi}{2}\frac{S_{max}}{\sigma_0}\right)\right]^{1/\alpha} \\ A_1 &= \left(0.415 - 0.071\alpha\right)\frac{S_{max}}{\sigma_0} \\ A_2 &= 1 - A_0 - A_1 - A_3 \\ A_3 &= 2A_0 + A_1 - 1 \end{aligned} \tag{1.19}$$

In these equations, α is the plane stress/strain constraint factor, and S_{max}/σ_0 is the ratio of the maximum applied stress against the flow stress, typically assumed to be constant. The use of this parameter as a constant has been shown to produce acceptable results for positive stress ratios, where the effect of S_{max}/σ_0 on the crack opening function is relatively small [64]. For most of the materials, a value $S_{max}/\sigma_0 = 0.3$ is adopted, chosen as an average value obtained from fatigue crack growth experiments, adopting different geometries for the specimens.

The threshold stress intensity factor range, $\Delta \mathrm{K}_{th}$ of eq.(1.17), is approximated by the following empirical equations:

$$\Delta K_{th} = \begin{cases} \Delta K_1 \cdot \sqrt{\dfrac{a}{a+a_0}} \cdot \dfrac{\left(\dfrac{1-R}{1-f}\right)^{\left(1-RC_{th}^m\right)}}{\left(1-A_0\right)^{\left(C_{th}^p - RC_{th}^m\right)}} & \text{if } R < 0 \\ \Delta K_1 \cdot \sqrt{\dfrac{a}{a+a_0}} \cdot \dfrac{\left(\dfrac{1-R}{1-f}\right)^{\left(1-RC_{th}^p\right)}}{\left(1-A_0\right)^{(1-R)C_{th}^p}} & \text{if } R \geq 0 \end{cases} \tag{1.20}$$

where ΔK_1 represents the threshold stress intensity factor for $\mathrm{R} \rightarrow 1$, C_{th}^m and C_{th}^p are interpolating parameters for negative and positive stress ratios respectively and a_0

is El-Haddad's parameter for small cracks [66]. An equivalent formulation, for the thresholds, is:

$$\Delta K_{th} = \Delta K_{th0} \frac{\sqrt{\frac{a}{a+a_0}}}{\left[\frac{1-f}{(1-A_0)(1-R)}\right]^{(1-C_{th}R)}} \tag{1.21}$$

where ΔK_{th0} is the threshold stress intensity factor at R=0 and C_{th} is an interpolating parameter valid along the whole stress ratio range. This formulation is being replaced by the one of eq.(1.20).

The choice of the S_{max}/σ_0 parameter, which can considerably affect the predictions, will be discussed in Appendix A.

1.6.3 The effect of experimental methodology onto threshold ΔK_{th} determination

The traditional experimental procedures used to generate thresholds, reported in the ASTM E647 standard [58], are known as 'ΔK-decreasing' and 'constant K_{max}'. Such procedures have been challenged [67–70] because it seems they influence the generated experimental results. One of the most popular evidence of this fact is the observation that small cracks propagate at SIF levels below the long crack thresholds derived by means of these traditional procedures, which does not converge to the value extrapolated from the Kitagawa diagram, as in Figure 1.17 [71].

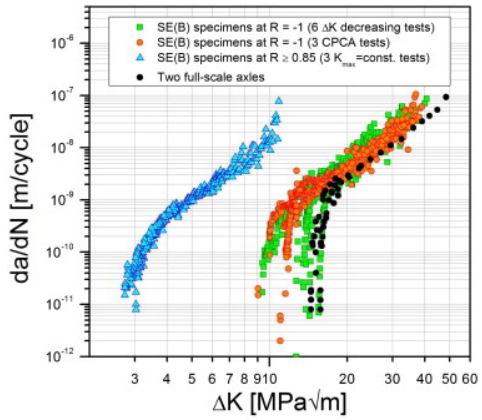

(a) Constant amplitude loading growth curves obtained from SE(B) specimens

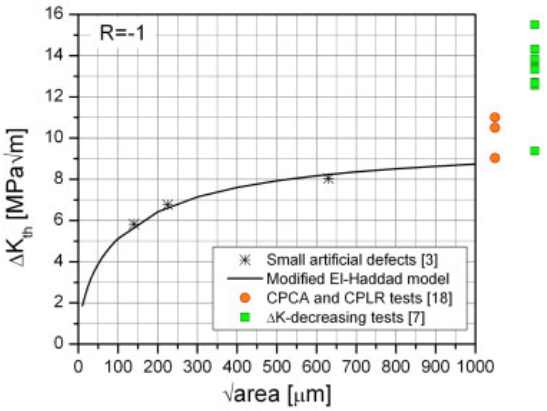

(b) Thresholds obtained by different methods

Figure 1.17: *Propagation data from A1N steel grade [71]*

In particular, the ΔK-decreasing has shown, for some materials, a sensibility to the growth rate reached by the crack at the beginning of the load reduction procedure: the ASTM E647 standard [58] suggests to begin such procedure at 10^{-8} m/cycle, but references [68–70] have shown that such growth rate happens usually at a SIF level high enough to introduce significant load interaction effects (mainly due to plasticity-induced crack closure [51]) and, consequently, to arrest growth too early, so generating

high and non conservative threshold values. Considering, instead, constant K_{max}, the sensibility seems to be related to the maximum applied SIF: in this case, depending on the considered material, the higher is the applied constant K_{max}, the lower is the generated threshold.

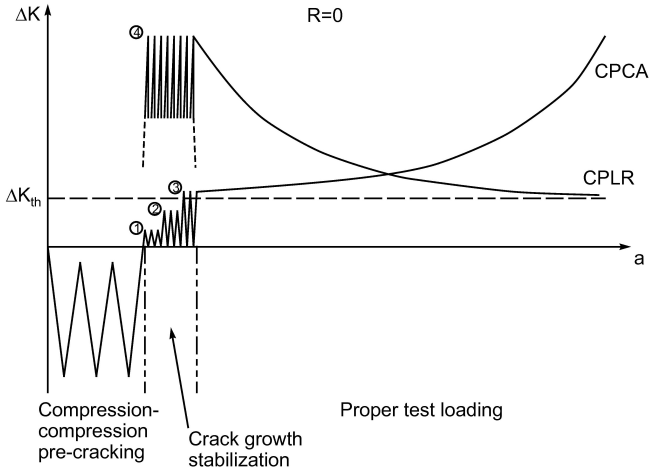

(a) Schematic of the experimental procedures at R=0

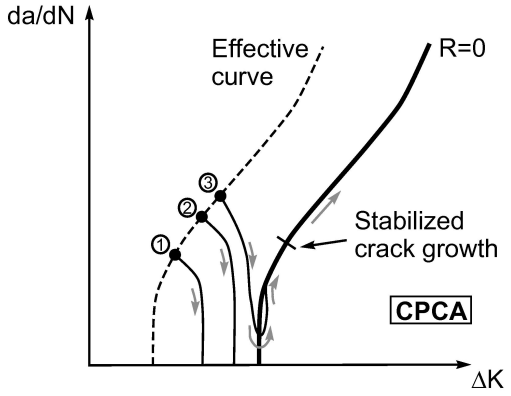

(b) Compression pre-cracking constant amplitude (CPCA)

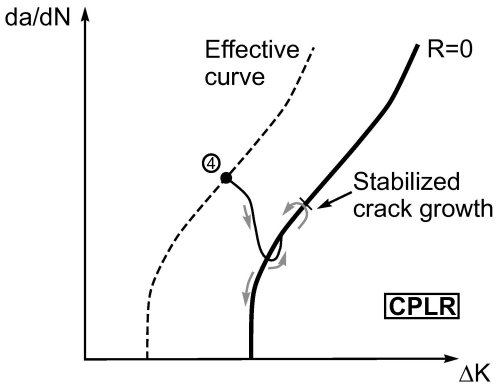

(c) Compression precracking load reduction (CPLR)

Figure 1.18: *Compression-compression pre-cracking methods to experimentally generate thresholds [72]*

A different experimental procedure [67] is being more and more adopted, in order to overcome these problems, based on a pre-cracking stage of fracture mechanics specimens obtained by the growth of short cracks under cyclic compression [73], followed by a stabilization step of crack growth and then proper load programs able to generate threshold values in condition where load interaction effects are absent or minimal. Such proper load programs are: i) 'compression pre-cracking constant amplitude' (CPCA) [67]; ii) 'compression pre-cracking load reduction' (CPLR) [74], where the load reduction technique is carried out so to minimize the interaction effects. Figure 1.18 shows a schematic of the compression-compression pre-cracking methods for experimentally generate thresholds. In particular, the first load cycle causes the material to yield in compression in the region of the notch, resulting then in a tensile notch-tip

residual stress field when the specimen is unloaded [75]. Subsequent compression-compression fatigue loading nucleates the pre-crack, which propagates making the tensile residual stresses to gradually relax until the local driving force diminishes below the crack growth threshold and the pre-crack finally arrests. In this way, a closure-free and naturally non-propagating crack is generated at the notch-tip of the specimen.

The pre-crack must then be grown several compressive plastic zone sizes in order to stabilize crack propagation by eliminating the influence of both the stress concentration of the notch and the tensile residual stresses [70]. Since the obtained pre-crack is closure-free, crack growth stabilization is required in order to naturally develop the proper closure mechanisms, at the crack tip, and to move from the effective crack growth curve to the one of the considered stress ratio (Figures 1.18b and c). In the case of CPLR, the positive applied load cycles are characterized by an amplitude higher than the threshold (case 4 in Figures 1.18a and c): when the crack tip is far enough from the notch-tip and the crack growth is stabilized, a ΔK-decreasing procedure is applied in order to generate the threshold. Such load reduction can so be applied from growth rates significantly lower (10^{-9} m/cycle or lower) than those suggested in the ASTM E647 standard, so minimizing load interaction effects. Theoretically, CPCA is the best procedure and should be preferred because load interaction effects are completely absent during the whole experimental test, but, since CPCA tests are in the 10^8 and more cycles range, and the crack growth curve in the threshold region is quite steep, so it can be easily completely missed increasing the load amplitude from a step to the subsequent one during a CPCA test, the CPLR procedure is being more and more adopted.

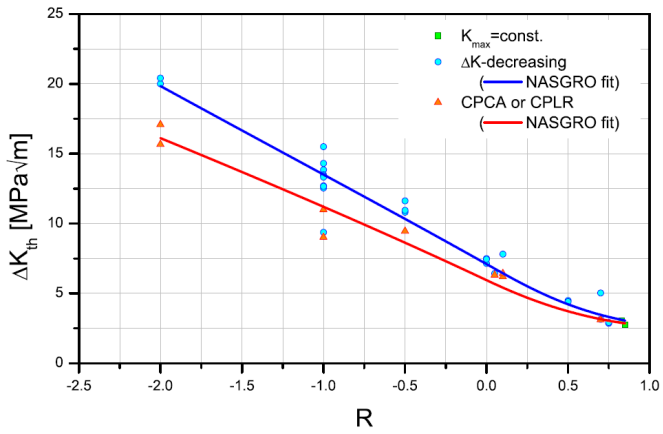

Figure 1.19: *Comparison of threshold trend with the stress ratio R, for A1N steel, by adoption of the two ΔK-decreasing and CPLR methods [72]*

Figure 1.19 shows the difference in the evaluated thresholds in dependence of the adopted methodology [72], relatively to the A1N steel grade. As can be seen, the traditional approaches yield higher thresholds in respect to the CPLR methodology: the differences increase decreasing the stress ratio (till reaching a difference of about 25% at R=-2). It is worth remarking that CPLR results are in the conservative direction, and tend to coincide with extrapolation of thresholds from the Kitagawa diagram (1.17b).

1.6.4 Load interaction effects

Even if the load spectrum is widely adopted for the fatigue calculations, it lacks the important information of the load sequence, which leads to the retardation or acceleration effect, well-known from the literature [50, 76, 77], due to the change of the plastic zone ahead the crack tip and the plastic wake.
Referring to a constant loading with a single overload [77], the interaction mechanisms can be summarized as:

1. Crack tip blunting: a shallow crack tends to the shape of a notch when overloaded; crack retardation is related to the amount of cycles required to nucleate and propagate a new fatigue crack out of the notch;
2. Residual stresses: after an overload, compressive residual stresses, close to yielding, arise ahead of the crack tip; since the characteristic plastic radius generated by an overload is bigger than the one generated by constant loading, several fatigue cycles are required in order to let the crack exit of the plastic radius and continuing propagating;
3. Plasticity induced crack closure: the plastic wake is responsible for crack retardation, in comparison to the effective FCG, associated to the stress ratio; an overload causes a sudden increasing in the plastic wake thickness, leading to an additional retardation effect;
4. Strain hardening: the high plastic strains cause a hardening of the region behind the crack tip, not allowing the crack tip to open and, thus, retarding the propagation.

Plasticity induced crack closure is by far the mechanism affecting the most crack growth retardation. Several models are available in the literature, for the characterization of the retardation effect onto crack propagation due to VA loading. They can be grouped in three main categories [78]: models based on the plastic wake, statistical models and models based onto crack closure. Models based on the plasticity induced crack closure are the ones which can predict at best the load interaction effect [79], and are widely implemented in commercial softwares [80, 81].

Regarding an axle in service, it is always subjected to a variable amplitude loading, so, load interaction should be considered in the lifetime predictions. But, depending on the involved material and S_{max}/σ_o ratio, the behavior at VA can be different. For example, in [71], experimental results on A1N steel under Time History loading didn't show a significant amount of retardation, while the software predicted it. In [82], with results reported in Figure 1.20, are reported studies of retardation, due to a single overload, onto A4T steel: a negligible load interaction effect was recorded applying high ΔK values, corresponding to high S_{max}/σ_o ratios, while a large retardation effect happened when testing the same material at low ΔK values, corresponding to low S_{max}/σ_o ratios.

Experiments onto full-scale specimens are quite rare, due to the complexity and cost of the tests, so only a few works are present in literature. It's worth remarking the work carried out at DB Germany by Mädler in 2013 [83]: the amount of retardation onto full-scale specimens made of A4T and 34CrNiMo6 was shown and related to the load sequence.

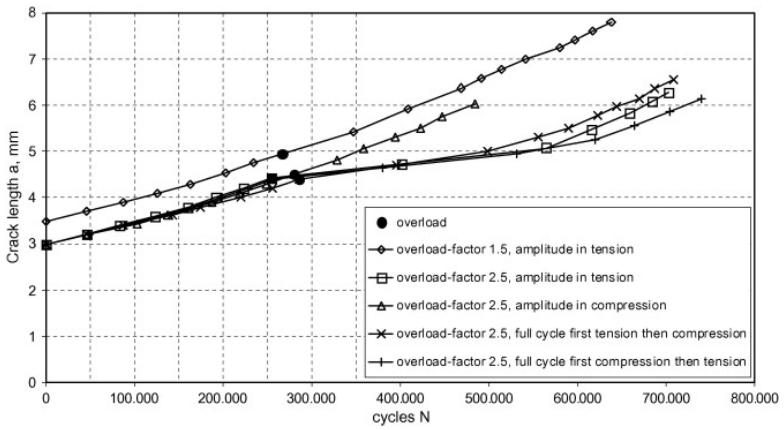

Figure 1.20: *Crack propagation behavior at constant amplitude loading at R = -1 with single overloads [82]*

No final results can be univocally stated; the usual practice in the railway axle design is therefore to ignore the retardation effects, so producing lifetime predictions with a large amount of conservatism. Further studies are required in order to carefully assess the retardation effect and predict residual lifetimes with better agreement to the experimental evidence.

1.6.5 The Strip-Yield model

The main feature of the Dugdale Strip-Yield model [84] is that it approximates the elastic-plastic behavior, at the crack tip, by superimposing two elastic solutions, as shown in Figure 1.21: a crack under remote tension plus a crack with closure stresses only, representing plasticity, at the crack tip.

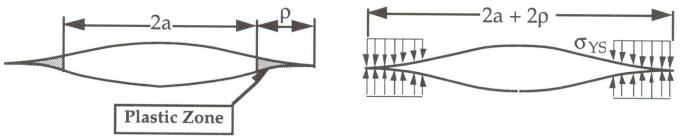

Figure 1.21: *Crack model in the original SY model proposed by Dugdale [84]*

The Strip-Yield model firstly proposed by Dugdale, found its maturity in the Newman's model [52], which modified the original algorithm in order to leave plastically deformed material in the wake of the crack during the propagation and to account for three dimensional constraint effects. The Newman's model is based upon an infinite plate containing a crack, having semi-length a, subjected to a constant stress orthogonal to the crack. In particular, the ρ plastic zone extension is evaluated as for Dugdale, and discretized into 'strips', having small width, which break and plastically deform during fatigue crack growth, thus generating the 'plastic wake'.

The crack can be divided into the three regions shown in Figure 1.22:

1. a linear elastic region, having fictitious semi-length $d = a + \rho$;
2. a plastic region ρ, divided into perfectly plastic strips, with σ_0 flow stress;

3. the contact region, where elements are already broken and in contact with the adiacent face, representing the crack closure phenomenon.

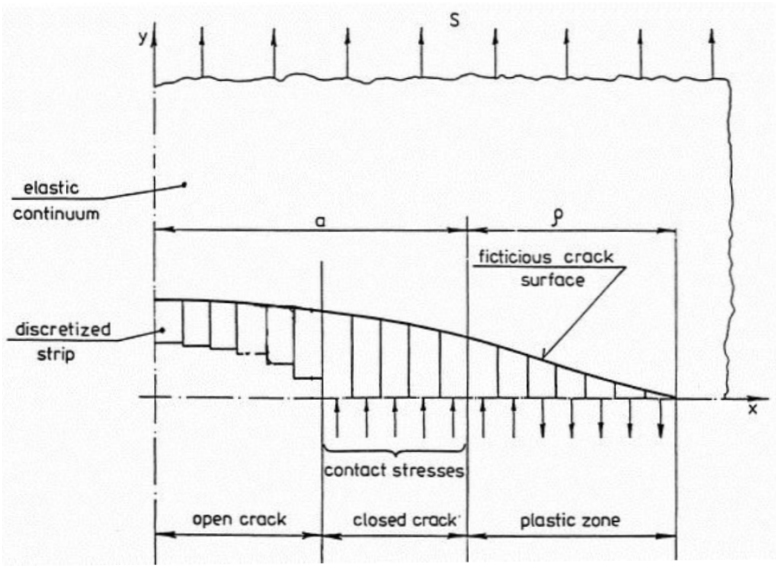

Figure 1.22: *Three regions, at the crack tip, represented by the Newman's model [52]*

The α constraint factor is adopted in the SY model, increasing the effective flow stress value as $\alpha\sigma_0$, where α is typically assumed as one in the case of plane-stress and three in the case of plain-strain condition. One of the strong points of the model is that with a simple parameter α is possible to describe a three dimensional problem, simplifying the analytical formulation; on the contrary, since the α parameter has to be carefully identified (experimentally or by FE approach), the application of the SY model is not straightforward.

1.6.6 Global constraint factor

Crack propagation tests on full-scale railway axles are usually carried out by three point rotating bending or resonant facilities, applying rotating bending by an eccentric rotating mass on top of the axle. When comparing results of crack propagation against similar tests carried out onto small-scale specimens (typically SE(B) [58], since a negative stress ratio has to be applied), a 'scale effect' appears, as in the already shown Figure 1.17a, relative to the A1N material. This effect, reducing the FCG by factor of about 2.5 [71], is due to the different constraint, at the crack tip, experienced by full-scale and SE(B) specimens. A dispersion in the evaluated FCG, related to both the constraint at the crack tip and the plasticity induced crack closure, is known in the literature [85–88], and was directly observed from the author [89]. The evaluation of a global constraint α represents a typical approach in the assessment of the fatigue-crack growth in metallic materials, as it is influenced by constraint variation around the crack front. The plane stress/strain constraint factor, α, is usually treated as a constant for the purposes of fitting the crack growth curves [80]. Values range from 1, which corresponds to a plane stress condition, to 3, which corresponds to a condition of plane strain. Materials such as high-strength steels, for which the K_{Ic}/σ_{ys} ratio is fairly

low, are assigned relatively high α values (2.5 or higher), while materials with higher K_{Ic}/σ_{ys} ratios usually exhibit α values ranging from 1.5 to 2.0. While better correlation with experimental results may be obtained by allowing α to vary with K_{max} [65], good agreement has been obtained by using it as a fixed fitting parameter.

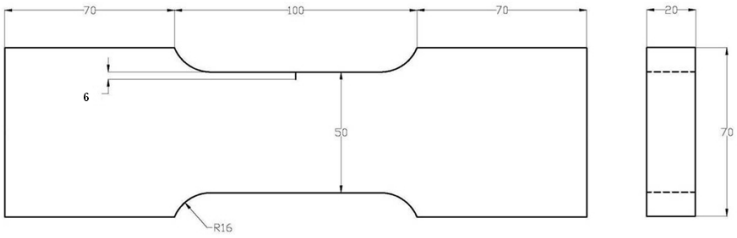

Figure 1.23: *Companion specimen of full-scale axles: modified SE(T) geometry [90]*

A novel geometry of specimen was designed [90], in order to better represent the constraint at the crack tip of a crack inserted in a full-scale axle, permitting to see these geometry as 'companion specimens' [91] of railway axles. The idea arose from the observation that SE(B) specimens have a small thickness and a very high a/W ratio, while railway axles show an opposite trend, having high thickness and small a/W ratio; the developed SE(T) specimen, in Figure 1.23, with increased thickness and width (20x50mm) could better represent the constraint of a crack in a full-scale axle.

1.7 Summary of the open points that will be covered

Among all the arguments related to the design of railway axles, the following points are still under discussion, and will be considered during the research activity of this phD thesis:

1. assessment of the allowable damage sum, regarding the safe-life design method, representative of the useful lifetime of the railway axles;
2. comparative application of the design methodology presently adopted by the current regulations, representing the infinite life concept, against the damage sum calculation, representing safe life, and the damage tolerant approaches;
3. effect of the compressive residual stresses onto crack propagation, and verification of the commonly adopted algorithms to correctly evaluate lifetime predictions;
4. effect of the load interactions, due to the load sequence, onto crack propagation, regarding companion and full-scale specimens; the verification of the no-interaction model and a calibration of the α parameter, for the strip-yield model have to be carried out, as well as a comparison of the crack growth algorithms.

CHAPTER 2

Variable amplitude fatigue assessment onto small-scale specimens

2.1 Introduction

When performing lifetime assessments, under VA loading, adopting the Miner's rule, or other damage assessment methods derived from this one, the choice of the allowable damage sum is one of the most critical points, since it can affect the results in a large way. For the calculations, the more advanced current regulations [3] consider the Miner Konsequent rule, with an allowable damage sum D lower than the unity and the 2.5% percentile of the fatigue curve as reference. The objective of this part of the research was to verify this choice of D, and to compare the Haibach's rule [5] against the more complex Miner Konsequent one. In the frame of the Euraxles european project [92], three batches of 25CrMo4 material (A4T) in the shape of small-scale specimens, produced by three partners across Europe, were firstly tested at CA loading, in order to derive the fatigue limit of the material and the finite life region of the Wöhler diagram. Then, seven VA loading tests were carried out applying block loading derived from a given load spectrum. The results of VA loading were finally compared to predictions carried out adopting both the Haibach's rule and the Miner Konsequent approach [3]. Several lifetime calculations were carried out, assuming different values of the allowable damage sum D, in order to find the best approximation of the experimental evidence.

2.2 Characterization of the fatigue properties of the A4T tested material

The characterization of the A4T material [1, 2] against fatigue was focused onto the determination of the Fatigue limit of the material, from a staircase testing sequence,

and of the Wöhler diagram, for characterizing the finite life region.

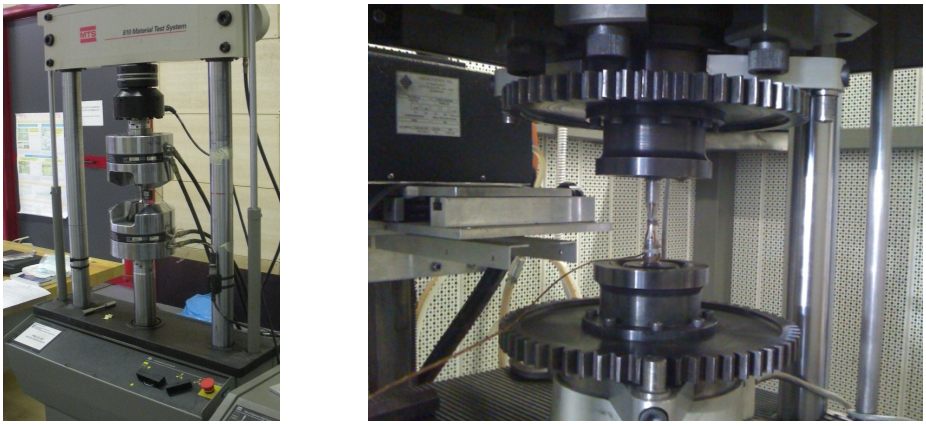

(a) Servo-hydraulic facility (b) Rumul resonant facility

Figure 2.1: *Experimental setup adopted for the characterization of the material to fatigue*

Two setups were adopted for the HCF characterization: a setup on MTS mono-axial servo-hydraulic facility, equipped with a 100 kN load cell, in Figure 2.1a, and another one on Rumul mono-axial resonant facility, equipped with a 100 kN load cell, in Figure 2.1b; the reason of the two setups was because, while the tests onto a resonant machine are faster, running at about 100 Hz, depending on the material and specimen's geometry, not all the stress range can be covered, due to the non-linear response of the material in the upper stress range, where some plasticity occurs. The upper part of the Wöhler diagram was covered by the servo-hydraulic facility, working at 25 Hz. Some stress levels were repeated on both machines, in order to check the results. The adopted specimen's geometry, for both the adopted facilities, is shown in Figure 2.2; specimens were supplied by three different producers across Europe, here named as 'A', 'B' and 'C'.

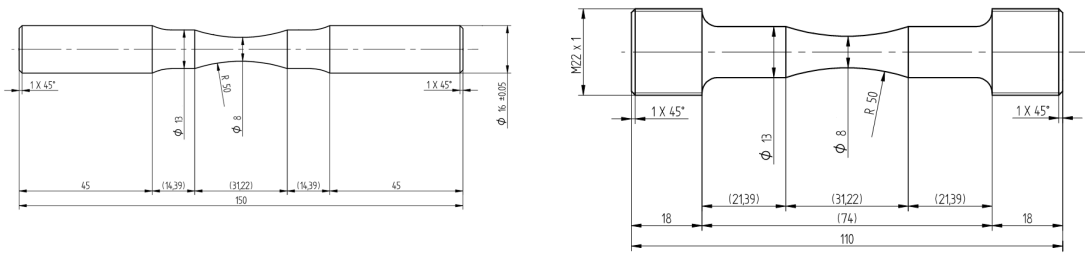

(a) For servo-hydraulic facility (b) For rumul resonant facility

Figure 2.2: *Specimen's geometry*

The results of the carried out fatigue tests, normalized, for privacy reasons, against the fatigue limit evaluated from the Stair-case sequence, leaded to the S-N diagrams of Figure 2.3, evaluated adopting the log-likelihood method [93]; each batch of A4T specimens was tested independently, then all the experiments were considered together,

in order to derive the global fatigue diagram, in Figure 2.4, representative of the whole A4T production across Europe.

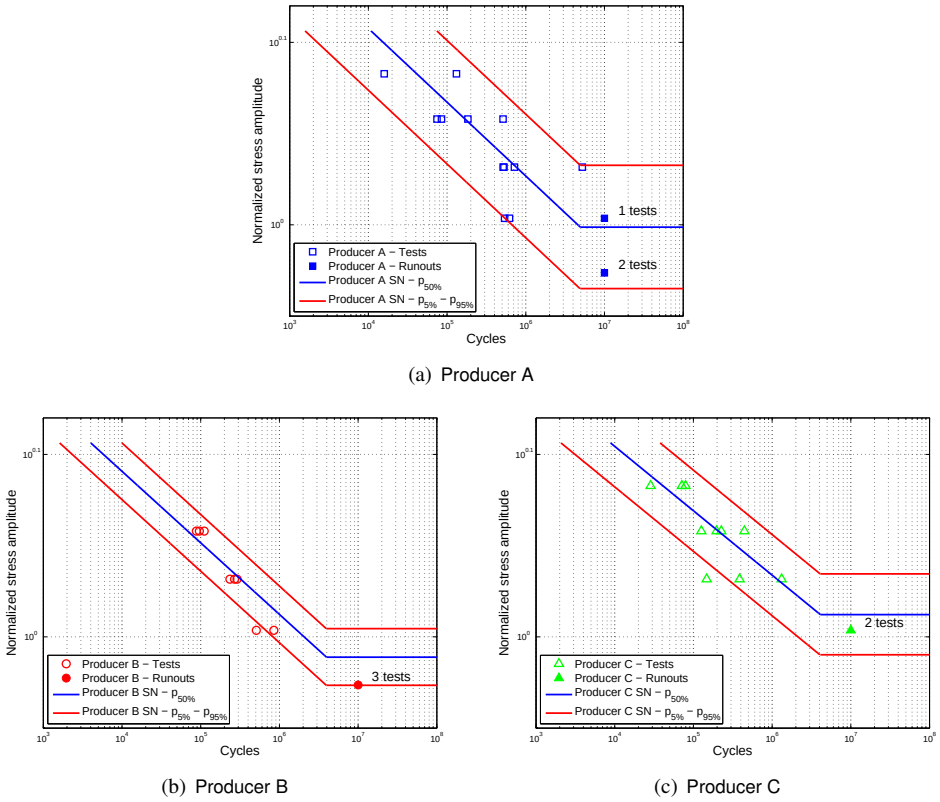

(a) Producer A

(b) Producer B

(c) Producer C

Figure 2.3: *Normalized S-N diagrams of each producer*

Batch	Normalized S_{lim}	σ_{logS}
whole A4T	1	0.021
A	0.997	0.018
B	0.975	0.013
C	1.029	0.016

Table 2.1: *Comparison of the fatigue limits evaluated for the different batches*

As can be seen from the three diagrams of Figure 2.3, batch C has a fatigue limit slightly higher than the average value, while batch B shows an opposite trend and batch A is in-line with the global behavior, but shows the highest statistical dispersion. The normalized fatigue limits are compared in Table 2.1.

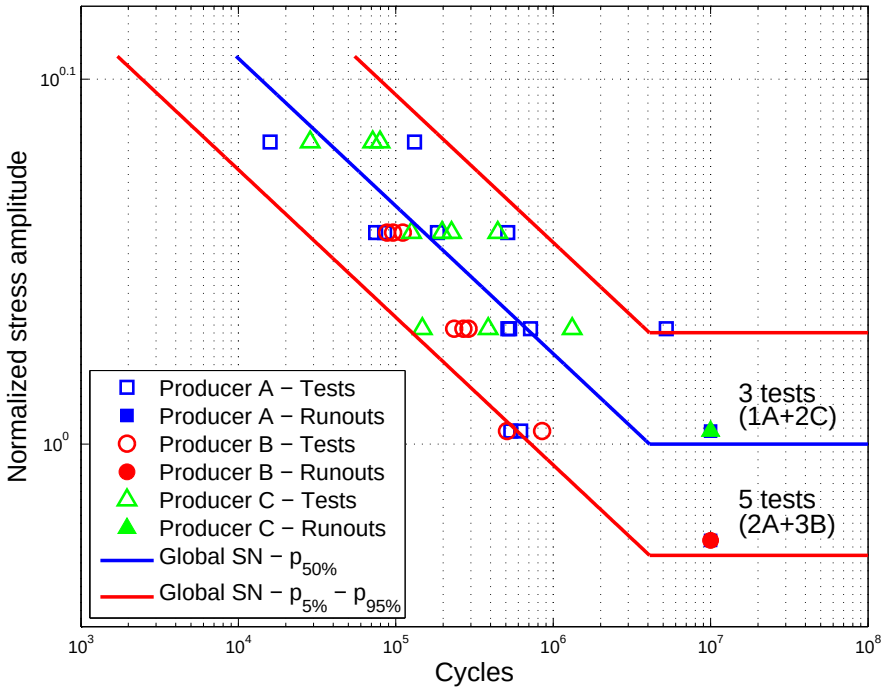

Figure 2.4: *Normalized S-N diagram of the whole A4T material tested*

2.3 Variable amplitude loading tests

A total of seven specimens, from the three batches, were tested under VA loading, in order to verify the Konsequent Miner's rule against the Haibach's rule.

2.3.1 Evaluation of the loading spectrum for VA testing

The load spectrum adopted for the fatigue tests at VA was given as normalized, as shown in Figure 2.5a. It was firstly discretized in blocks, each 5% in amplitude, then translated to the right, in order to have a minimum block length of 1000 cycle, since this was the minimum block length accepted by the Rumul resonant facility adopted. Finally, the block sequence was randomized, as shown in Figure 2.5b; each of the tested specimen was subjected to the same sequence, rescaling the maximum amplitude to the desired value.

Firstly, in order to check the feasibility of the VA tests, specimen A9, from Producer A, was instrumented with a strain-gage, as shown in Figure 2.6a, in order to measure the effective load spectrum received by the specimen, against the given command. A loading spectrum, having $\sigma_{max} = 200$MPa, was applied to this instrumented specimen; the maximum stress level was chosen in order not to break the specimen, letting the possibility of re-testing it at a reasonable stress amplitude. During a single spectrum repetition the time history coming from the strain gage was recorded through a HBM Spider central unit, then, at the end of the measurement, the recorded time history was processed using the Rainflow algorithm [27], in order to evaluate the effective spectrum experienced by the specimen. Measurements were successfully compared to the command, as shown in Figure 2.6b: the imposed loading spectrum is well followed

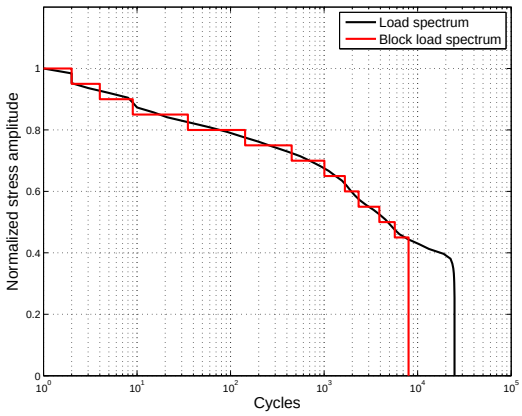

(a) Load spectrum

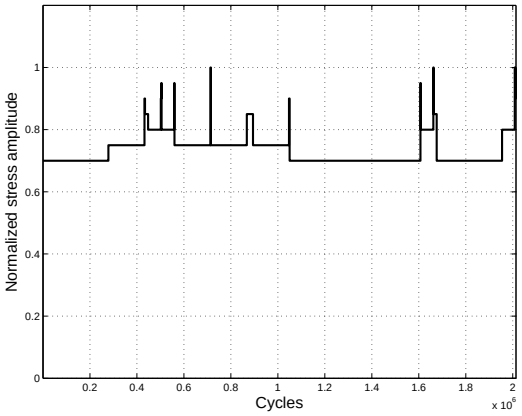

(b) Applied block load sequence, derived from the load spectrum in (a)

Figure 2.5: *Normalized VA loadings, in the shape of load spectrum and block loading sequence derived from real service*

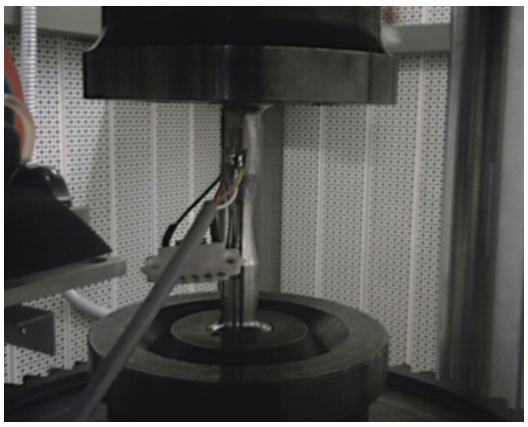

(a) Instrumented specimen

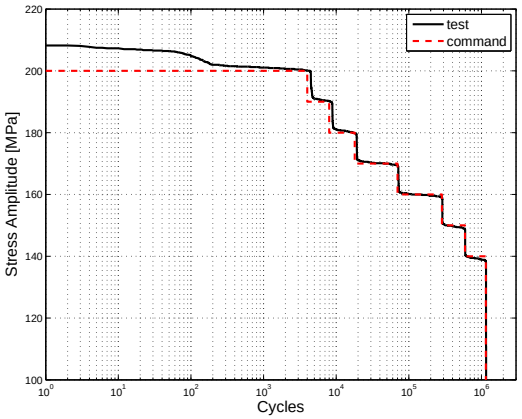

(b) Comparison between the load spectrum imposed to the specimen (dotted red line) and the one effectively experienced (black line)

Figure 2.6: *Verification of the load spectrum applied during the tests*

by the facility; only a few cycles at higher stress level were recorded, but the difference is almost negligible.

2.3.2 Probabilistic analysis of the results from testing

All the carried out tests at VA are summarized in Table 2.2. The spectrum amplification, through the parameter σ_{max}/FAT, where FAT indicates the estimated fatigue limit of the material, is shown, as well as the number of cycles each specimen afforded. Moreover, the 'Damage Index' is indicated, calculated as the ratio between the cycles to failure and the estimated lifetime, as for the Miner Konsequent rule [3]; the latter was estimated fixing the allowable damage sum D at the value one, and adopting the

S-N diagram having probability of failure 50% ($p_{50\%}$), in Figure 2.4.

Specimen	Producer	σ_{max}/FAT	Cycles	Damage Index ($D = 1$, $p_{50\%}$)
A5F	A	1.129	102714000 (not broken)	3.464
A9	A	1.183	1369100	0.232
HR04	B	1.143	920800	0.074
HR07	B	1.076	100942000	1.733
HR09	B	1.143	1405700	0.113
CF4	C	1.183	13072000	1.185
CF8	C	1.183	4891300	0.444

Table 2.2: *Carried out VA tests*

In order to compare tests carried out at different stress level, the results were normalized in terms of the gaussian standardized variable $z = (cycles - \mu_{MK})/\sigma_{logN}$, being μ_{MK} the lifetime prediction, as for the Miner Konsequent rule, and σ_{logN} the standard deviation of the Wöhler diagram in the cycles direction; an example of such procedure, applied to specimen $A9$, is shown in Figure 2.7.

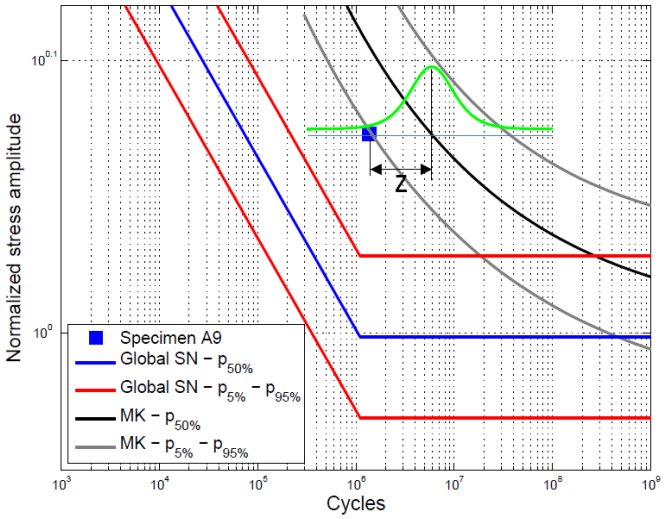

Figure 2.7: *Evaluation of the gaussian standard variable* $z = (cycles - \mu_{MK})/\sigma_{logN}$

Figure 2.8 reports the calculations carried out considering an allowable damage sum equal to one and the mean estimated fatigue life ($p_{50\%}$); all the gaussian standardized variables were compared against the normal standardized distribution in Figure 2.8a, while in Figure 2.8b the probability chart is shown, comparing the experimental evidence (red dotted line), evaluated on the carried out tests, to the expected trend (black dotted line). As can be seen from Table 2.2, specimen $A5F$ was stopped, after more than 100 million cycles, prior to breaking; it was considered as broken, for the calculations, resulting in conservative considerations.

As can be seen from Figure 2.8a, the experimental results are not centered under the gaussian plot, but stay on the left side, meaning that the lifetime predictions are not conservative. The same evidence clearly appears from Figure 2.8b: even if the theoretical mean life prediction is included inside the 95% confidence band of the experiments,

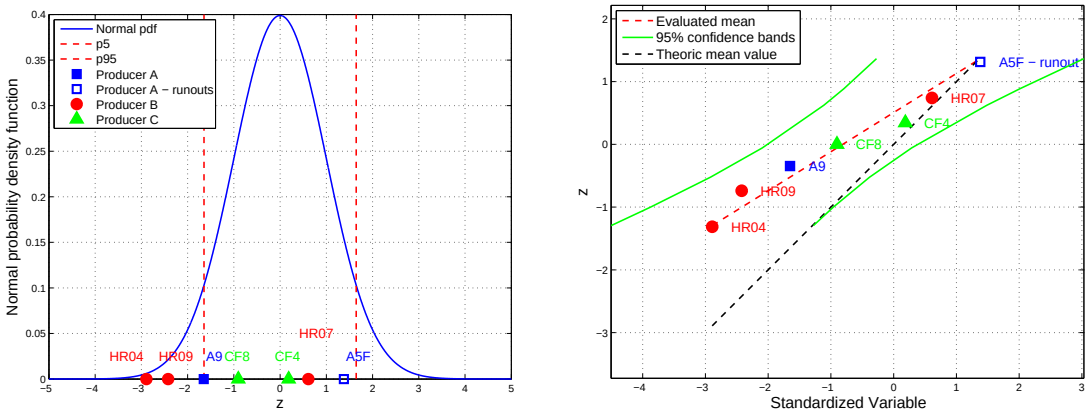

(a) Standardized normal distribution of the VA tests carried out

(b) Gaussian probability chart referred to (a)

Figure 2.8: *Results of the normalized VA tests, calculated adopting an allowable damage sum $D = 1$, evaluated on the $p_{50\%}$ fatigue curve*

it is not centered, but stays on the lower part. A correction on the lifetime evaluation has to be carried out.

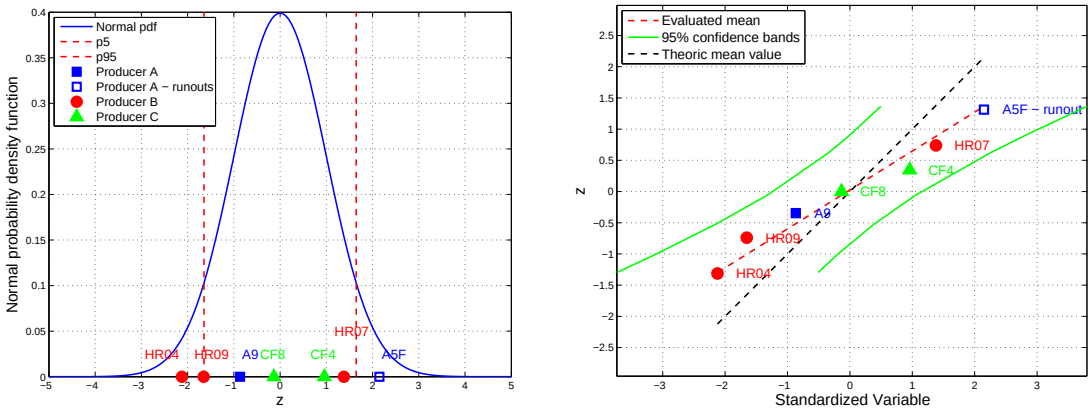

(a) Standardized normal distribution of the VA tests carried out

(b) Gaussian probability chart referred to (a)

Figure 2.9: *Results of the normalized VA tests, calculated adopting an allowable damage sum $D = 0.5$, evaluated on the $p_{50\%}$ fatigue curve*

Figure 2.9 reports the standardized normal distribution, and probability chart, calculated onto the experimental results when adopting an allowable damage sum equal to 0.5 and the mean S-N diagram ($p_{50\%}$). As can be seen, lowering the allowable damage sum from the typical value 1 [4] to 0.5, permitted to better represent the experimental evidence. The theoric mean value and the evaluated one cross at the zero value, and the theoric line is well centered inside the 95% confidence bands.

2.3.3 Comparison of the results with the predictions as for Haibach

Similar conclusions could be drawn when adopting the Haibach's rule [5] instead of the Miner Konsequent one. Figure 2.10 shows the gaussian probability charts calculated onto the experimental results, adopting the Haibach's rule on the mean Wöhler diagram ($p_{50\%}$) with damage sum $\sum n/N = 1$ (Figure 2.10a) and 0.5 (Figure 2.10b) respectively. As can be seen, these charts are very close to the ones evaluated adopting the Miner Konsequent rule (Figures 2.8b and 2.9b): the lifetime predictions, with damage sum equal one were not conservative, while better agreement could be found when adopting a damage sum equal 0.5.

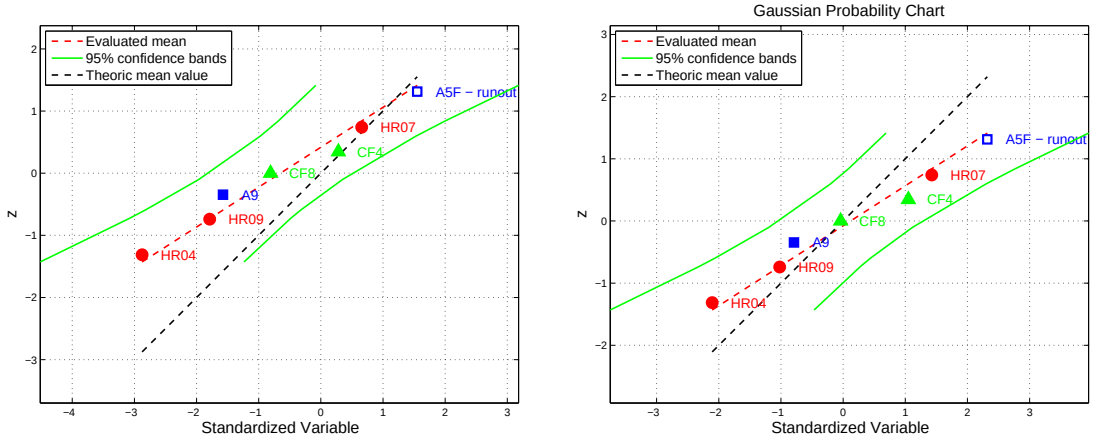

(a) Damage sum $\sum n/N = 1$

(b) Damage sum $\sum n/N = 0.5$

Figure 2.10: *Gaussian probability charts obtained from Haibach's calculation [5]*

Specimen	Life predictions according to Haibach	Life predictions according to Miner Konsequent
A5F	25393226	29655853
A9	5501920	5891367
HR04	12292689	12471706
HR07	55784881	58203833
HR09	7054111	7143285
CF4	10128433	11028620
CF8	10128433	11028620

Table 2.3: *Life predictions comparison, according to both Miner's rule and Miner Konseqent, with* $D = 1$

Lifetime predictions carried out by the two methods, Haibach and Miner Konsequent, are shown in Table 2.3; as can be seen, predictions, evaluated with the same parameters, are nearly identical. This evidence demonstrates that the interaction effects are nearly absent in the tested specimens, probably due to the fact that the stresses, in the load spectrum, are high when compared to the fatigue limit.

A last calculation was performed, adopting the indications of the FKM guidelines [3]: the allowable damage sum was set to 0.3, with calculations performed on the $p_{2.5}$

percentile of the fatigue curve. As can be seen from the plot of Figure 2.11, most of the specimens show a z value higher than zero, except the shorter experiment, specimen $HR04$, which is slightly lower than zero. This means that the predictions carried out as for the FKM guidelines give conservative predictions, but not too conservative if adopted as design criterion.

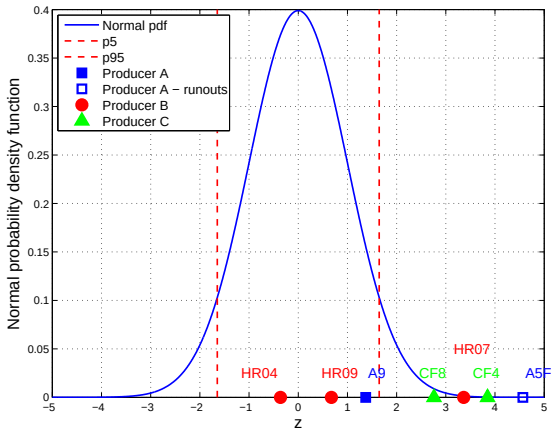

Figure 2.11: *Standardized normal distribution of the VA test, calculated adopting an allowable damage sum* $\sum n/N = 0.3$*, evaluated on the* $p_{2.5}$ *fatigue curve*

2.4 Concluding remarks

The fatigue behavior of the A4T material, under VA loading, was considered in this part of the research, against the lifetime predictions carried out by the meaning of the haibach's rule or the more complex Miner Konsequent one. From the carried out experiments and calculations, the following considerations could be drawn:

- an allowable damage sum equal to one, with calculations performed on the mean S-N diagram, is not conservative, in respect to the experiments;
- an allowable damage sum equal 0.5 seemed to be adequate to represent the experimental outcomes, adopting the mean S-N diagram for the calculations;
- calculations as for the FKM guidelines exhibit lifetime predictions on the safe side; the suggested parameters, set as $D = 0.3$ onto the 2.5% percentile of the fatigue life ($p_{2.5\%}$) seems to be adequate as design criterion;
- calculations performed adopting the Haibach's rule, or the more complex Miner Konsequent approach resulted in nearly identical lifetime predictions, not justifying for the increase of computational effort of the latter methodology;
- a comparison between lifetime calculations performed by a damage sum and the fracture mechanics approach has yet to be explored.

CHAPTER 3

Fatigue Assessment of Axles with Old Design

3.1 Introduction

The rules for axle design presently in force in Europe [1, 2] ensure railway axles to meet the required levels of safety and reliability. However, due to the long service life of these components, and to the different axle design approaches used in the past, a significant number of old axles are still in service, some of which are not fully compliant with the current design criteria. Even if no failure of these axles happened during their service, the purpose of this part of the research was to propose an approach aimed at supporting life extension of 'old' axles, not complaint with the current regulations, allowing them to reach the end of their service life fully meeting safety and reliability requirements. The proposed approach was based on a damage tolerance approach [14] and relies on the use of multi - body simulations for the accurate quantification of service loads based on the real wheelset service scenario, with the final aim of defining appropriate intervals for the non-destructive inspection of railway axles [82] which allow to operate railway axles in safe conditions. The approach foresees a partitioning of the whole mission of the vehicle into a discrete number of running conditions, considering all relevant service conditions such as vehicle speed, track curvature, cant deficiency track irregularity levels, traction and braking. For each considered running condition, the time history of wheel/rail contact forces were obtained by means of multi-body simulation, hence the time history of bending and torsion moments in the critical sections of the axle are then derived considering also the effect of traction/braking torques by means of a realistic modeling of the breaking/traction profile. Then, FE analyses were performed on the axle and used in combination with the results of Multi-Body simulations to determine the acting stresses in the free surface and selected cross-sections (fillet and shaft) of the axle. Based on these results and using appropriate crack-propagation models, a procedure for a numerically supported derivation of

inspection intervals was proposed and its implementation was discussed. An attempt to extend the evaluated results to other non-complaint axles, not considered in this part of the research, was carried out by proposal of a simple parameter, as indicator of the working conditions of the axles against its design limits. Moreover, the application limits of the current regulations were discussed.

3.2 Test Cases Definition

Two test cases were considered as representative of a different series of old railway axles, for urban people transportation, that were no longer compliant to the current European Standards [1, 2]; all the axles involved were made of high strength steel 30NiCrMoV12. The first axle considered, in the following marked as 'Case A', in Figure 3.1, was a motor axle not fulfilling the modern design standard requirements for the transitions to wheelsets; these transitions were almost flat, showing a high stress concentration factor, with a SCF value close to 2, considerably higher than the typical values of the EN13261 [37], where a stress concentration factor of approx 1.2 arose at the body-press-fit transition.

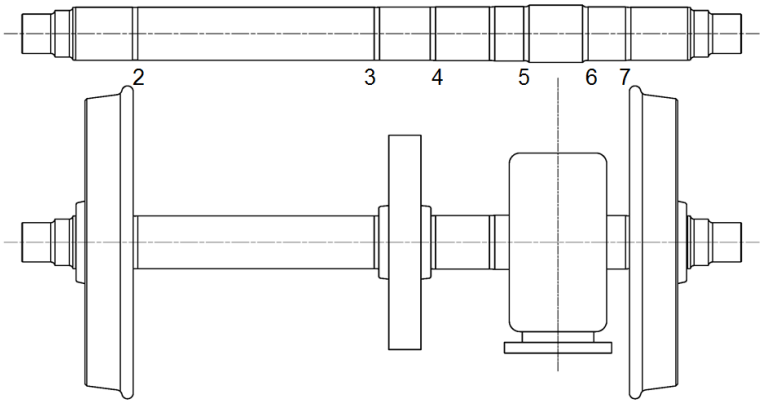

Figure 3.1: *Axle denoted as 'Case A'*

The second considered axle, in the following 'Case B', in Figure 3.2, was again a motor axle of an urban railway vehicle. It was chosen because its transitions numbered as 5 and 7 in Figure 3.2, under the gear box seats, had a shape which was not considered by the current standards. A third axle, fully compliant with the current regulations, was taken into account only for comparing the relevant parameters derived; this axle will be called 'Case C' in the following.

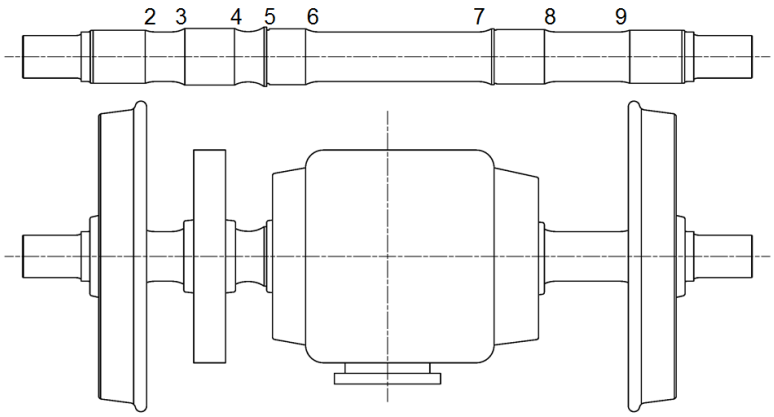

Figure 3.2: *Axle denoted as 'Case B'*

3.2.1 FE Analyses

FE analyses were carried out, for each test case analyzed, in order to evaluate the stress state onto the axles; the effects of the rotating bending moment, due to the applied loads at the journal bearings, and the interference from press-fitting of wheels and hubs were taken into account.

Only half of the axle and the hubs were modeled and structurally meshed adopting 20-node hexahedral elements with reduced integration (C3D20R), having global dimension 10 mm but reduced to about 1 mm along the transitions close to press-fit seats, where the stresses had to be carefully measured; the material was idealized as a linear-elastic steel, having Young's modulus $E = 210$ GPa and Poisson's ratio $\upsilon = 0.3$. The implemented model is represented in Figure 3.3a. Axle and auxiliaries were modeled separately, and joined through a surface to surface coupling, including the interference fit option, for taking into account the stresses from press-fit; the mean value of the interference, and 0.3 as friction coefficient, were adopted. The boundary conditions of the assembly were introduced by a hinge-roller at the contact points between wheels and rails; loads were applied at the bearing journals. Two separate steps were adopted for the application of the loads: during the first step, only the non-linear contact with interference fit option was applied, then, in the second step, the forces at the bearing journals were added. Results, as in the details of Figure 3.3b-e, are here shown as the nodal average of the values extrapolated from Gauss quadrature points; in particular, for sake of clarity, only one section of each axle is here shown, representing the more dangerous point of the two considered Test Cases: section 2, regarding 'Test Case A', and section 5, regarding 'Test Case B'. For both sections, the maximum stress from the rotating bending (Figure 3.3b and d) and press-fit (Figure 3.3c and e) conditions are shown.

Since press-fit leads to an increasing of the mean stress, but has no influence onto the alternate component, the stress concentration factors were evaluated in the pure bending configuration, along each fillet of the two test cases considered; the estimated values are reported in the graph of Figure 3.4, and compared against the typical SCF value (1.2) of a transition which design is fully complaint with the Current Regulations [1,2]. As can be seen from Figure 3.4, the SCFs of the two test cases considered are higher than expected; especially at the bottom point of transition 5 of the 'Case B' axle, a SCF

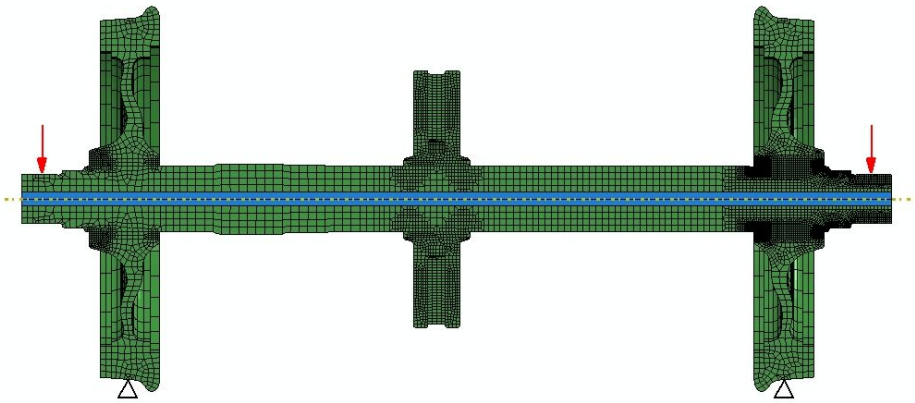

(a) Global 3D model for the 'case A' axle

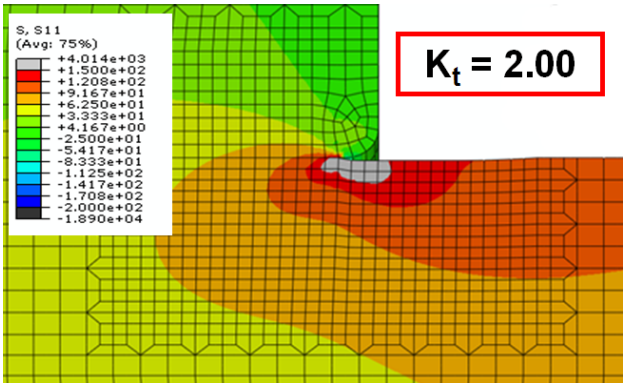

(b) 'Case A' section 2: longitudinal stresses from rotating bending

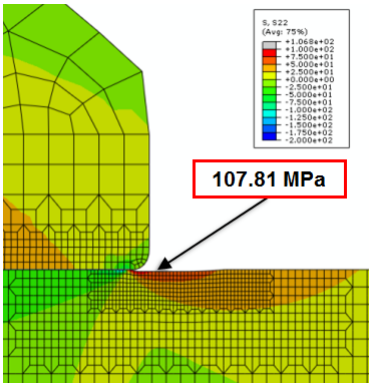

(c) 'Case A' section 2: longitudinal stresses due to press-fit

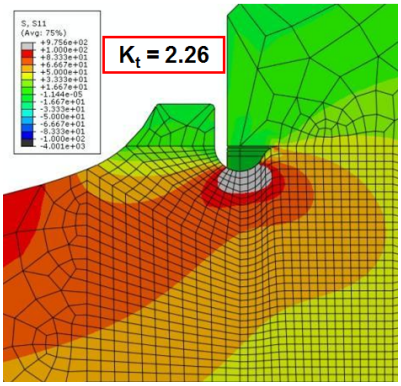

(d) 'Case B' section 5: longitudinal stresses from rotating bending

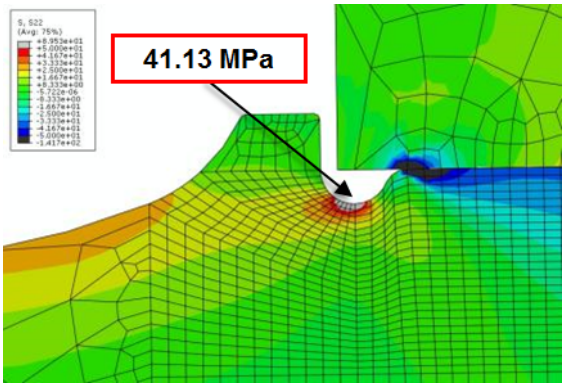

(e) 'Case B' section 5: longitudinal stresses due to press-fit

Figure 3.3: *Typical results of the carried out FE analyses for test Cases 'A' and 'B'*

value of 2.26 was found.

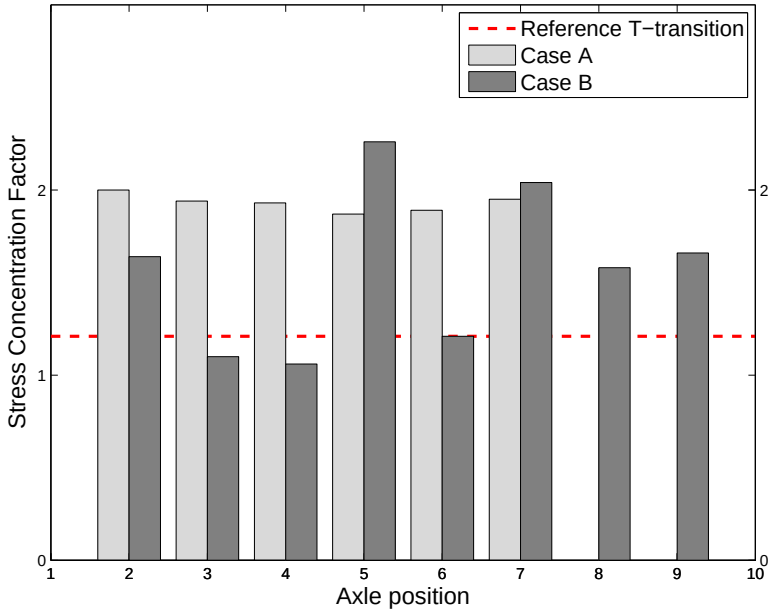

Figure 3.4: *Stress Concentration Factors evaluated as in the current regulations for the two 'Case A' and 'Case B' axles*

3.3 Assessment of the Axles according to the Current Regulations

The presented axles were firstly verified following the indications of the active Current Regulation EN13104 [2], relative to the motor axles. A simplified calculation process is adopted by the standard, considering, for a generic geometry of axle, the equilibrium of the forces in the vertical and lateral direction, at the contact between wheel and rail, and due to the inertia of the vehicle traveling in a curve (relevant parameters: mass of the vehicle and barycenter position); in addition, traction and braking action are considered (relevant parameters: maximum deceleration).

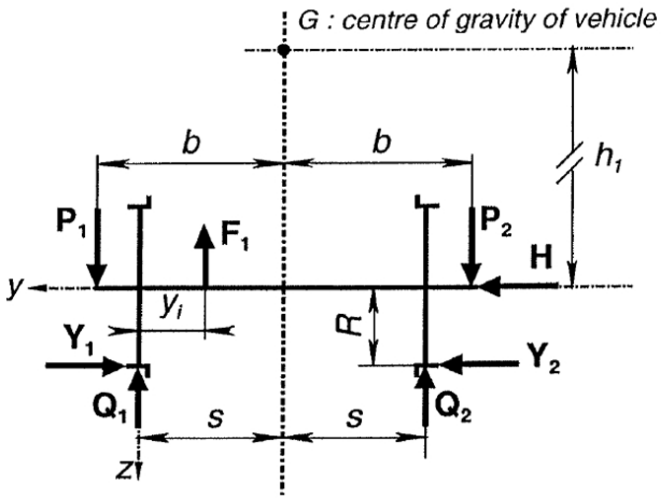

Figure 3.5: *Schematization of the wheelset and application of the loads as in the Current Regulations*

Figure 3.5 illustrate the application of the forces to the wheelset, as in the Current Regulations; the calculation of the forces has to be done in accord to the formulas of eq.(3.1):

$$\begin{aligned}
P_1 &= (0.625 + 0.0875 h_1/b)\, m_1 g \\
P_2 &= (0.625 - 0.0875 h_1/b)\, m_1 g \\
Y_1 &= 0.35 m_1 g \\
Y_2 &= 0.175 m_1 g \\
H &= Y_1 - Y_2 = 0.175 m_1 g \\
Q_1 &= \frac{1}{2s}\left[P_1(b+s) - P_2(b-s) + (Y_1 - Y_2)R - \sum_i F_i(2s - y_i)\right] \\
Q_2 &= \frac{1}{2s}\left[P_2(b+s) - P_1(b-s) - (Y_1 - Y_2)R - \sum_i F_i y_i\right]
\end{aligned} \tag{3.1}$$

In particular, the EN13104 active standard, requires:

- all the contributions to the bending moment, from masses, braking and traveling in curve, have to be considered; forces in the longitudinal direction and at contact can be neglected;
- the Fatigue Limit is different for the 'Axle Body' and 'Wheel Seat' spots;
- the Safety Factor η is equal to 1.5 for motor axles and 1.2 for non-powered axles;
- results are presented as 'Security Factors', evaluated as ratios between the acting stresses and the Fatigue Limit, already reduced by the η Safety Factor: by this calculation, all the values below one denote an inadequacy of the design of the axle;
- both directions for traveling the curve (left and right) have to be considered; only the worst condition is considered for the calculation of the 'Security Factor'.

3.3.1 Fatigue limit of the material

Since the material adopted was not one of the two materials, EA1N and EA4T, whose fatigue limits are standardized by [1, 2], the Standard itself provided the corrections to be applied to the generic fatigue limit of the base material in order to obtain the reference fatigue limits for both the seats and the transitions, as in eq.(3.2):

$$\eta = \eta_{A1N} \cdot \frac{R_{fL_{30NiCrMoV12}}/R_{fE_{30NiCrMoV12}}}{R_{fL_{EA1N}}/R_{fE_{EA1N}}} \tag{3.2}$$

where η_{A1N} is the safety factor for A1N material (1.5 for motor axles and 1.2 for non-motor axles), and R_{fL} and R_{fE} are the fatigue limits under rotating bending at 10^7 cycles for smooth and notched specimens respectively. For privacy reasons, these fatigue limits cannot be revealed; anyway the Safety Factors for the 30NiCrMoV12 material, corrected in order to take into account the higher notch sensitivity in eq.(3.2), become $\eta_{30NiCrMoV12_{motor}} = 1.814$ and $\eta_{30NiCrMoV12_{non-motor}} = 1.451$.

3.3.2 Application of the Current Regulations to the test case axles

The application of the Current Regulations to the test case axles will be here discussed; due to privacy reasons, no data relative to the axle or vehicle will be shown.
Points 2 to 7 of Figure 3.1 and 2 to 9 of Figure 3.2 were treated as transitions, where a Stress Concentration Factors is present, due to the change of diameter and the local geometry; the Fatigue Limit in these points was corrected by the parameter η of eq.(3.2); the SCF had to be evaluated as in Figure 3.6 [1, 2], which corresponds to the case of a simple transition geometry close to a single press-fit. The four seats (wheels, brake disk and gearbox), on the other hand, were treated as press-fits; also in these points the Fatigue Limit was corrected by the parameter η of eq.(3.2).

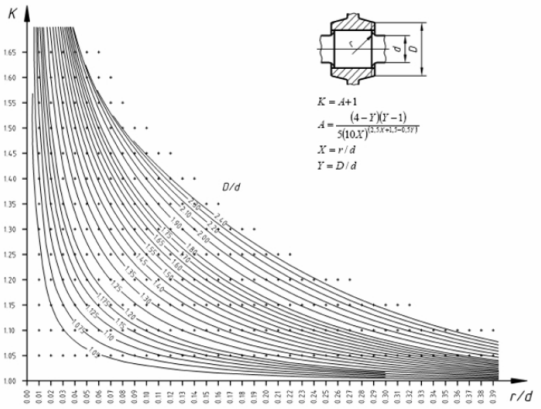

Figure 3.6: *Definitions of the SCF for the simple transition under the seats.*

The final Security Factor, for each considered section, was evaluated as the ratio between the Fatigue Limits, already reduced by the adequate security factor, and the maximum stress, evaluated according to the Current Regulations, in the investigated section, as in eq.(3.3); all the values lower than the unity represented a potential risk for the railway axle.

$$SF_{section} = \frac{FAT}{\sigma_{section}} \tag{3.3}$$

The two Tables 3.1 and 3.2 collect the Safety Factors evaluated, for the two 'Case A' and 'Case B' axles, along all the transitions close to the seats, where a SCF arises; the Stress Concentration Factor, calculated from the dedicated FE campaign, is reported as well.

Despite some of the evaluated Safety Factors are lower than the unity, meaning a potential failure, it is worth remarking that the railway axles here considered never failed, during more than 30 years of continuous service. This means that the current European Standard EN13103/04 [1, 2], are too much conservative; a novel calculation approach, based onto damage tolerance, is here considered.

Position	Safety Factor EN13103/04	SCF from FEM
[2] transition left wheel	0.826	2.00
[3] brake transition (left)	0.777	1.94
[4] brake transition (right)	0.824	1.93
[5] transmission transition (left)	0.992	1.87
[6] transmission transition (right)	0.992	1.89
[7] transition right wheel	0.906	1.95

Table 3.1: *'Case A' axle - Safety Factors evaluated as in the Current Regulations and SCF from FEM*

Position	Safety Factor EN13103/04	SCF from FEM
[2] transition left wheel	1.092	1.64
[3] brake transition (left)	1.074	1.10
[4] brake transition (right)	1.128	1.06
[5] transmission transition A (left)	0.739	2.26
[6] transmission transition A (right)	1.116	1.21
[7] transmission transition B (left)	0.776	2.04
[8] transmission transition B (right)	1.246	1.58
[9] transition right wheel	1.253	1.66

Table 3.2: *'Case B' axle - Safety Factors evaluated as in the Current Regulations and SCF from FEM*

3.4 Fatigue Analysis and Crack Propagation Assessment

The flowchart represented in Figure 3.7 illustrates the procedure adopted for the lifetime assessment of the considered axles. The stress history acting on the axles, section by section, was the starting point of the calculations; dedicated simulations of the track, together with the evaluation of the SCF from dedicated FE simulations, led to the knowledge of the loading spectra at each considered point. Two different calculations were then performed: the first and simplest calculation was the Fatigue Analysis adopting the Miner's rule [4], while the second one was the damage tolerant lifetime assessment downright, based onto crack propagation simulations; from the lifetime predictions carried out, opportune inspection intervals will be defined, based on the knowledge of the performances of the adopted NDT.

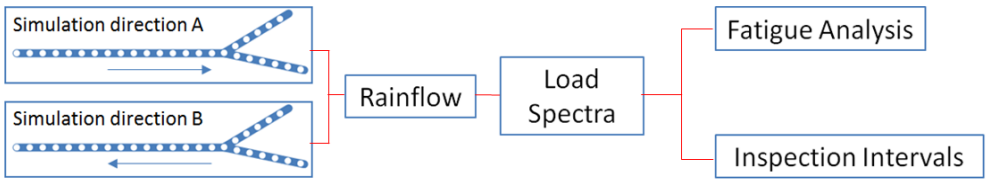

Figure 3.7: *Flow chart of the performed analyses*

3.4.1 Numerical Evaluation of the Axle's Load Spectra

In this section, an approach based on numerical simulation was adopted for the evaluation of the load spectra for the axle [94–96], which are essential to perform the fatigue assessment and the damage tolerant calculations.

For each of the two Test Cases 'A' and 'B' considered, a multi-body model of the whole vehicle, incorporating the axle under examination, was defined by means of the simulation package ADTreS, developed at Politecnico di Milano, Department of Mechanical Engineering [22,96]. The simulation code allowed to analyze the dynamic behavior of the train running in straight track and curve, on irregular track, considering the vertical and lateral running dynamics of the vehicle, but neglecting longitudinal dynamics. The models used for the purpose of this part of the research, were based on a rigid body schematization of the carbody, bogies and wheelsets. Track flexibility was considered according to a simplified approach based on a sectional model [97,98]. Wheel-rail contact forces were represented using a non-linear multi-Hertzian contact model [24], considering measured or theoretical profiles.

Excitation from track irregularity was introduced in the simulation by considering a time history of vertical and lateral displacements applied in the wheel-rail contact points, according to a measured or randomly generated irregularity profile.

For the urban railway application considered here, trains are operated on a single line which is run back and forth by trains. Therefore, with the aim of obtaining a reliable evaluation of the load spectra, the specific geometry of the line was considered. Each curve in the line was simulated, considering the actual geometric properties in terms of radius, cant, length of the transitions and of the whole curve.

The results of all numerical simulations were then evaluated in terms of time histories of the wheel-rail contact forces, and the bending and torsional moments arising in the axle as a consequence of the contact forces were computed according to the quasi-static procedure described in [94–96].

For the application considered here, the stresses produced by braking efforts represent a relevant contribution to the axle's load spectra and therefore need to be taken into account. Differently from the simplified approach proposed by standard EN13103/04 [1,2], which envisages the application of the maximum admissible braking acceleration as a constant value, the actual braking efforts were here considered, based on the measured speed profile of the vehicle; the total braking effort partitioned into a component due to regenerative braking (actuated by means of the vehicle motors) and another one due to pneumatic/mechanic braking (actuated by means of disk brakes). According to the braking strategy adopted for the considered vehicle, regenerative braking is applied until the vehicle speed is slowed down to 10 km/h, whereas at lower speeds mechanical braking takes place.

Finally, the time histories of the regenerative and mechanical braking efforts were converted into a time history of the bending and torsional stresses generated in the axle. To this end, the actual position of the gear-box and brake disk press-fits needed to be taken into account. The procedure was exemplified with reference to the test case 'A' axle which was equipped with one brake disk and a gearbox with two press-fits. This resulted in different bending moment diagrams for regenerative and mechanical braking, as shown in Figure 3.8. For mechanical braking, the maximum value of the bending moment was obtained in correspondence of the brake press-fit, whereas for

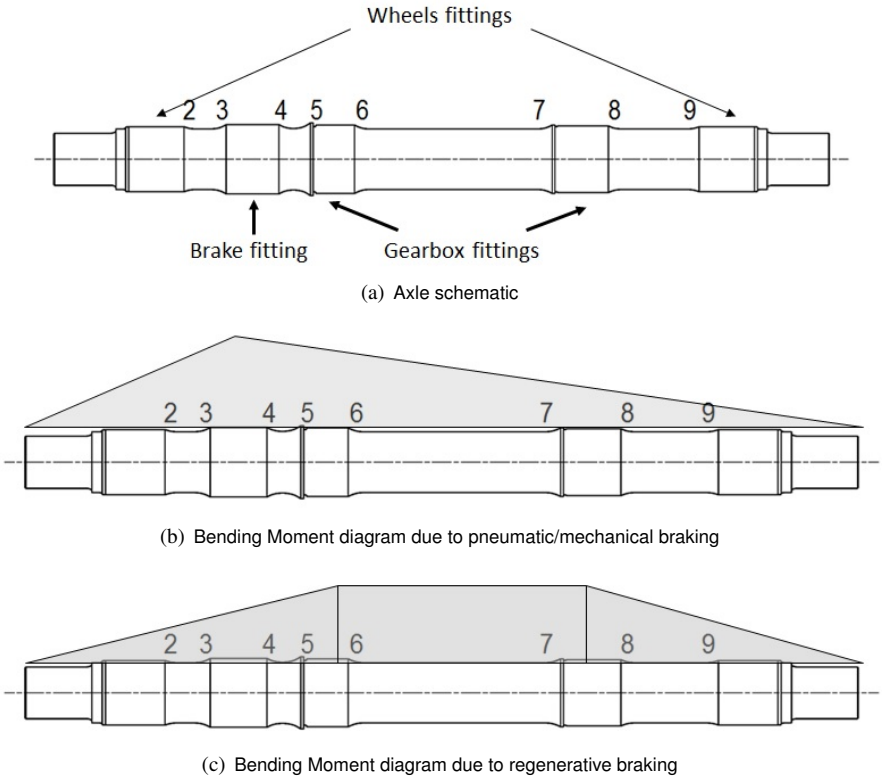

(a) Axle schematic

(b) Bending Moment diagram due to pneumatic/mechanical braking

(c) Bending Moment diagram due to regenerative braking

Figure 3.8: *Method for application of braking force*

regenerative breaking it took place in the section of the axle enclosed between the two gearbox press-fits.

3.4.2 Evaluation of the Stress Spectra from the evaluated Time Histories

The contact forces time histories were then converted into the equivalent stress spectra, through the 'Rainflow' algorithm [27], taking into account the local geometry of the axles section by section; an example of the spectrum resulting from the calculation is reported in Figure 3.9, for the most critical section of 'Case A' and 'Case B' axles, respectively. These two graphs show the comparison between spectra evaluated considering different braking scenarios: the red curves represent the case of only pneumatic braking, while the black ones represent the case of braking action distributed between disk and gears. The effect of the braking have a big influence onto the loading spectra; this will have, consequently, an effect onto the lifetime predictions.

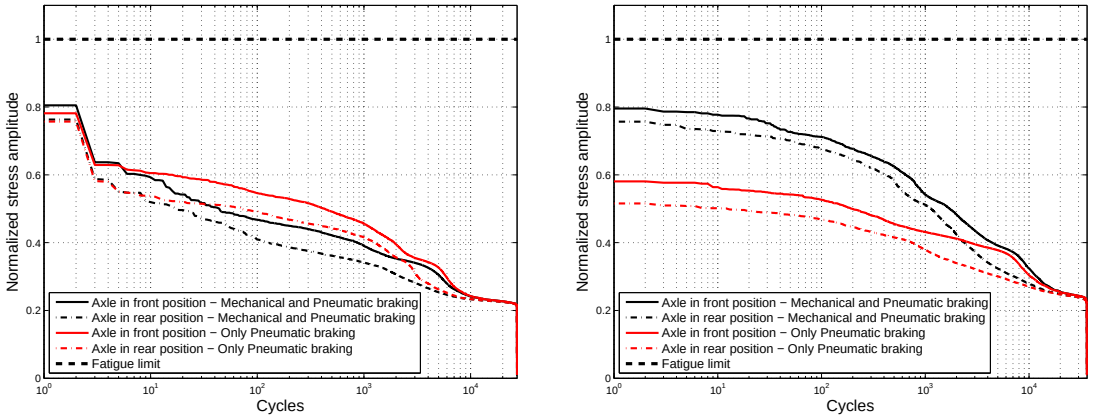

(a) Load spectrum for section 2 of the 'Case A' axle

(b) Load spectrum for section 5 of the 'Case B' axle

Figure 3.9: *Example of the evaluated loading spectra, normalized against the fatigue limit*

3.5 Lifetime assessment by a damage sum approach

Regarding the Miner calculation, illustrated in Figure 3.10, dividing the evaluated spectrum in k stress classes σ_i ($1 \leq i \leq k$), each contributing $n_i(\sigma_i)$ cycles, if $N_i(\sigma_i)$ is the total number of cycles to failure under the specific stress σ_i, failure occurs when:

$$\sum_{i=1}^{k} \frac{n_i}{N_i} = D \tag{3.4}$$

The fatigue curve shown in Figure 3.10 was deduced from previous activities, since EN13104 only allows to calculate the fatigue limit; the knee of the curve was set at $2 \cdot 10^6$ cycles, with slopes m in the finite life region and $2m - 1$ in the 'infinite one' (according to Haibach [5]). Both the load spectrum and the fatigue curve were normalized against the corrected fatigue limit.

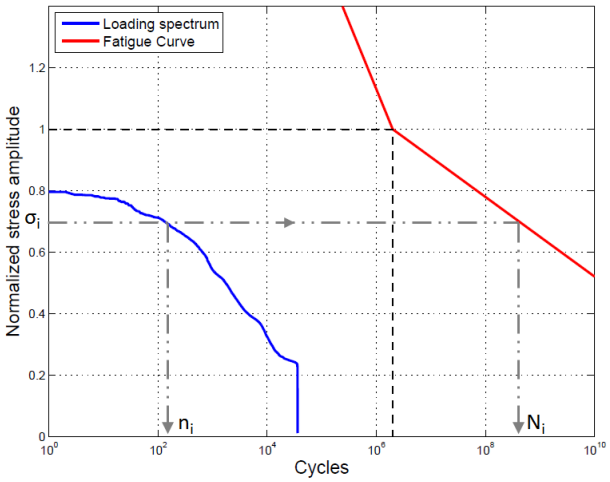

Figure 3.10: *Application of the Miner's rule of eq.(3.4)*

In accordance to [3, 6], the cumulative damage index D, in eq.(3.4), was here set to 0.3; this is also in agreement with the conclusions drawn in chapter 2, regarding the allowable damage sum.

Results of the Fatigue Evaluation as for the Miner's rule are shown in Figure 3.11, for all the transitions and the press-fit sections of the two test cases axles. For each transition, the considered stress amplitude spectrum was the 'local one', obtained multiplying the nominal spectrum of the section by the acting SCF.

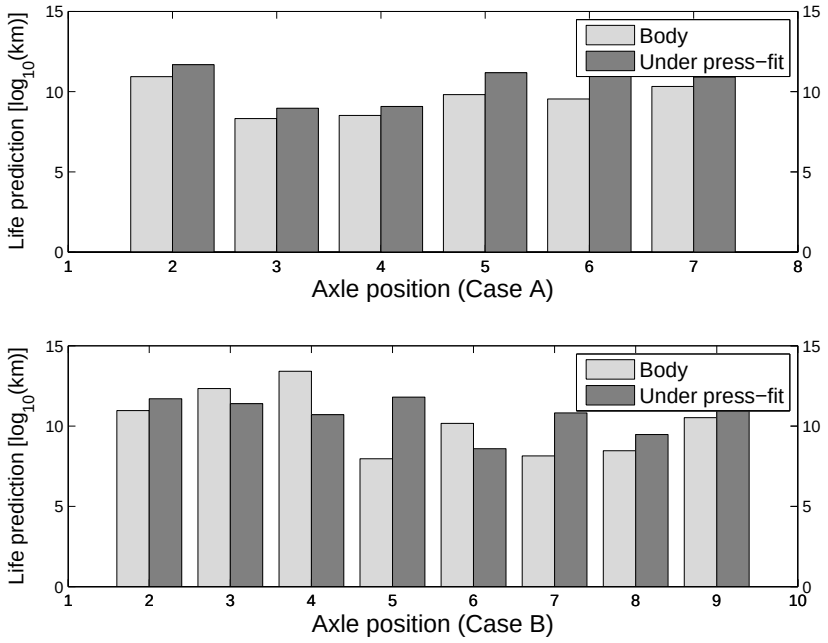

Figure 3.11: *Life predictions according to the Miner's rule*

As can be seen from Figure 3.11, a contradiction arose when comparing results coming from both the Current Regulations methodology and the Miner's rule; while for the European Standards the two axles are not complaint, the Miner's rule predicts lifetimes around 10^{10} cycles, which are in the 'Infinite Life' range, in accordance with the evidence that no failure occurred in service. Anyway, a standard Fatigue Life approach, based on the Miner's rule, is not adequate for managing the 'Safe Service extension' of these vehicles, since appropriate inspection intervals have to be defined; it was needed, for the purpose, to move to the damage tolerant approach.

3.6 Lifetime predictions based onto the damage tolerant approach

In order to perform a calculation of the residual lifetime of the axles, a crack propagation algorithm, not keeping into account for load interaction effects, and based on Shiratori's weight functions [99] for SIF determination, was developed.

Stress intensity factor solutions, for a crack inserted in a railway axle, are not given in the available handbooks of weight functions; only a few formulations, based onto FE methodology, already shown in chapter 1, are available. In order to perform quick analysis of the SIFs at the crack tip of a crack inserted in a railway axle, the Shiratori [99] weight functions were adopted. The Shiratori SIF solution, valid for a semi-elliptical

crack in a thick plate subjected to a known stress state, as in Figure 3.12, proved to give reasonable results also when applied to full-scale axles containing a typical semi-circular fatigue crack [30].

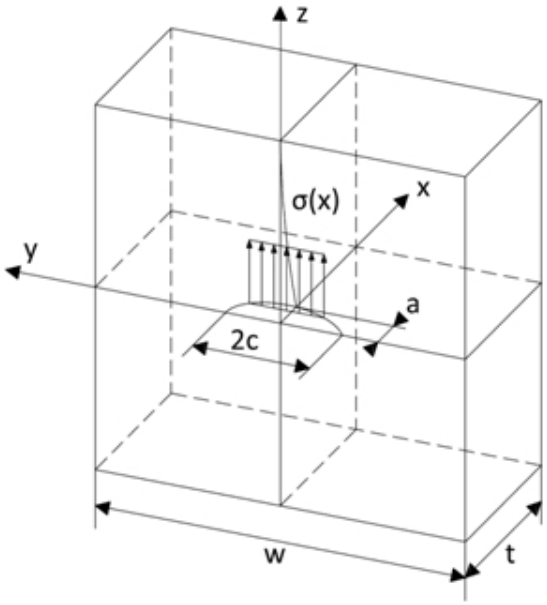

Figure 3.12: *Semi-elliptical crack in a thick plate subjected to a known stress state.*

The SIF values were evaluated at both the deepest point (point A) and the free surface (point C) of an hypothetical crack, in order to observe the variation of crack shape. The value of the dimensionless SIF is given in tabular form [99] at both points A and C for the interpolating polynomials of the applied stress up to the third order. In particular, four dimensionless crack ratios a/t (0.2, 0.4, 0.6 and 0.8), with a being the crack depth and t the thickness of the plate, and four aspect ratios a/c (0.2, 0.4, 0.6 and 1.0), with c being the semi-surface length, were considered by Shiratori. During the present life-time simulations, the dimensionless SIF M defined in eq.(3.5) was then evaluated by interpolation, considering the stress profiles for rotating bending and residual stresses, in order to determine the $K_0 - K_3$ parameters reported in eq.(3.6):

$$M = \frac{K_I}{(1/\Phi)\sigma_0\sqrt{\pi a}} \tag{3.5}$$

$$K_I = AK_3 + BK_2 + CK_1 + DK_0 \tag{3.6}$$

SIF values were independently determined for the two different stress conditions, given by rotating bending and press-fit, and then superimposed. For determining the SIFs in the prospective crack plane, the stresses due to rotating bending were determined by the dedicated finite element (FE) model shown in Figure 3.3. The position of the prospective crack plane was chosen as the position of the maximum principal stress, at the surface of the axle, given the superposition of both stress states. The rotating bending longitudinal stress profile along the prospective crack plane was derived and suitably interpolated for the application of Shiratori's solution; the same procedure was applied to the residual stresses, in the prospective crack plane, due to the presence

of the interference fit; the application of the Shiratori weight's functions is shown in the example of Figure 3.13.

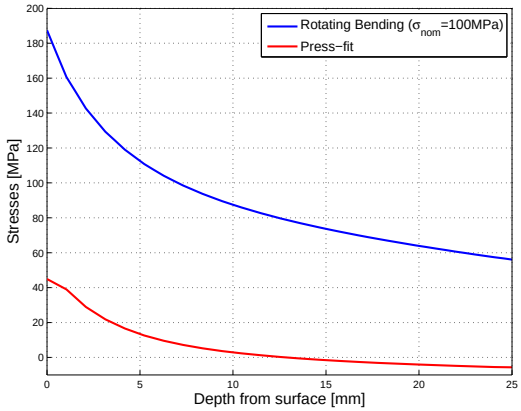

(a) Stresses from FE simulations

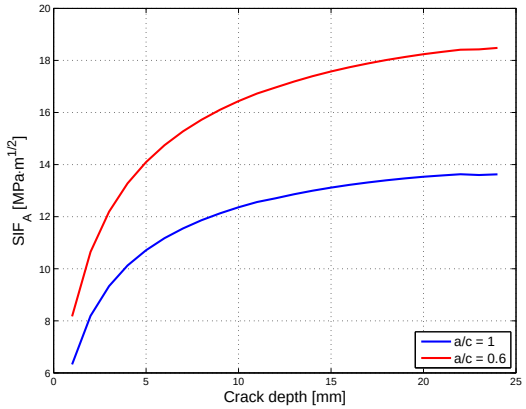

(b) Adimensional SIFs evaluated at the bottom point (A) of the crack

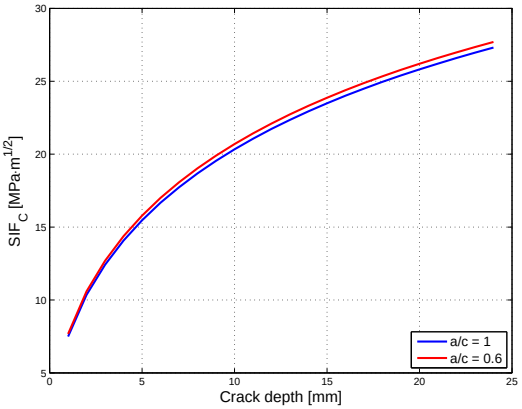

(c) Adimensional SIFs evaluated at the surface point (C) of the crack

Figure 3.13: *Example of application of the Shiratori weight's functions for the definition of the SIFs.*

Several crack growth simulations were carried out, for each section, also considering the different loading spectra evaluated from the different braking procedures; the shape of the initial crack was fixed as semi-elliptical, having depth 1 mm and the ratio $a/c = 0.6$, which is a typical defect having Probability Of Detection (POD) 50% from an in-line inspection adopting the UT measurements, as in [15]. In order to reduce the computational effort, the evaluated loading spectra were discretized in stress classes, having 5MPa amplitude, then the sequence of block loads was randomized. A summary of the adopted crack growth algorithm is given in the following:

1. given a block load level, calculation of the stress ratio acting at points A and C of the crack, due to the superposition of the rotating bending stresses and the residual stress field;
2. evaluation of the SIFs acting at the two points A and C;
3. independent evaluation of the crack growth rate, given the stress intensity factors ΔK and the stress ratios R, for both points A and C using the Forman-Mettu

equations [64] calibrated by the parameters found in the literature [100], relative to the 30NiCrMoV12 material;

4. definition of the actual crack size and shape, which acted as an input for the following block load.

The block load sequence was repeatedly applied up to failure or to an equivalent percurrence of 10 millions km.

Figure 3.14 shows an example of the carried out simulations of crack propagation onto the most critical sections of the two test case axles; the evolution of both points A and C are shown, as well as the two predictions, considering different braking procedures.

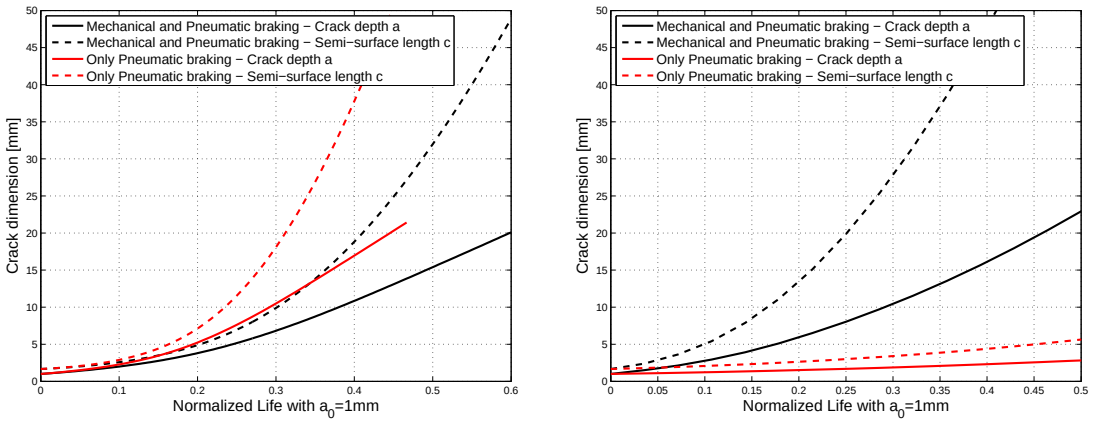

(a) Simulation of crack propagation for section 2 of the 'Case A' axle

(b) Simulation of crack propagation for section 5 of the 'Case B' axle

Figure 3.14: *Life predictions carried out for the more dangerous sections of the two axles; simulations carried out adopting the loading spectra as in Figure 3.9*

As can be seen from Figure 3.14, the braking procedure has a big impact onto life predictions; the knowledge of the effective braking strategy is of crucial importance for the correct determination of the residual lifetime and interval inspection of the railway axle.

Once performed the crack growth simulations, section by section, the inspection interval was defined, according to Figure 3.15, dividing by two the lifetime predictions, from the initial crack size, fixed in 1 mm with shape $a/c = 0.6$ [15], to the final fracture of the axle. Since the inspection interval represents the distance that can be safely run between two NDT controls, the factor two was chosen, as in [15], in order to ensure the possibility to observe the crack at least once, by a common in-line inspection by UT, during the lifetime of the axle.

All the evaluations of the inspection intervals, for all the sections of the two test case axles, are collected in Figure 3.16, and compared against the Safety Factors calculated as for the Current Regulations [2]; results, in term of inspection intervals, were normalized in respect to an appropriate conventional life. As can be seen, there is no direct correlation between the calculated Safety Factors, as required by the European Standards, and the estimated lifetime predictions based onto the simulated loading spectra.

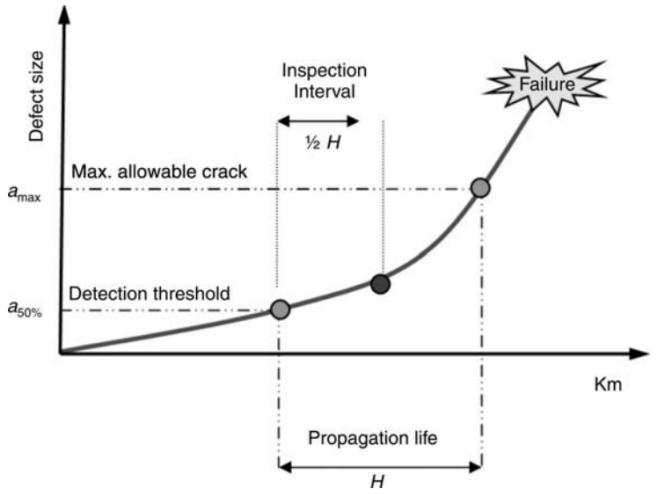

Figure 3.15: *Definition of the inspection interval, from the crack growth simulation [15]*

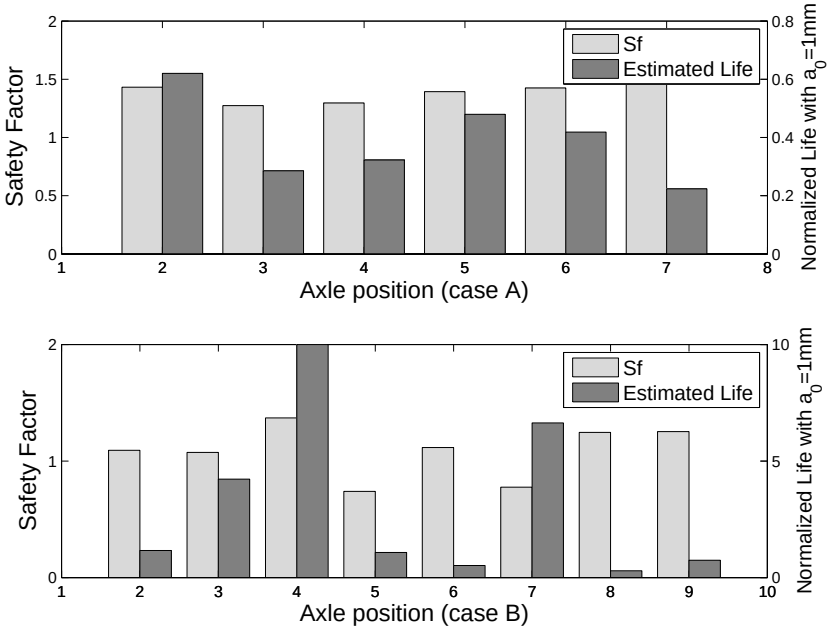

Figure 3.16: *Life predictions, from crack propagation simulations, against the Safety Factor, evaluated as in the Current Regulations*

The two plots of Figure 3.17 show the comparison between the predicted lives adopting the two braking scenarios explained. As can be seen, not only the predictions are different when changing braking strategy, but the locations of the most dangerous spots change too. This is a confirmation that the braking procedure can affect dramatically the lifetime predictions, and must be properly defined as an input for the calculation of the loading spectra.

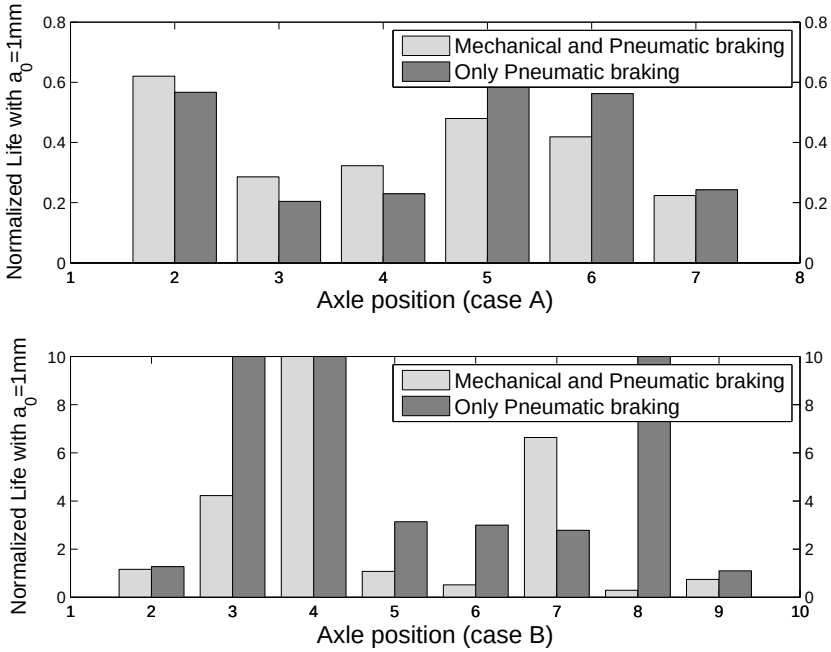

Figure 3.17: *Life predictions, from crack propagation simulations, considering different braking strategies*

3.7 Proposal of a Relevant Parameter representative of the 'Expected Service Life'

The burden of the calculations to be performed for the definition of the inspection intervals, as in Section 3.6, was heavy:

1. a FE model, with non-linearities due to the interference fit, was required for each transition of the axle; the stresses evaluated from the two loading conditions had then to be processed, as for the Shiratori weight's functions [99] in order to define the SIFs along the crack;

2. dynamic simulations of the wagon traveling had to be performed; loading spectra, section by section, had then to be evaluated from the time histories;

3. crack propagation simulations had to be carried out, at each section, and appropriate inspection intervals had to be deduced.

A Relevant Parameter, representative of the employment of the analyzed railway axles and able to simply correlate to the inspection interval to be adopted, have to be defined, in order to reduce the calculation effort.

The Current Regulations provide, as indicator, the 'Safety Factor', as already explained in Section 3.3; this parameter represents the ratio between the recommended Fatigue Limit [1, 2] and the maximum local stress range obtained by the calculations. But the inadequacy of this indicator to directly correlate with the appropriate Inspection Interval has already be proven; the overall picture for the different sections of the two test case axles can be seen from Figure 3.18a: the results, in this plot, show a very large

scatter, no direct correlation, and they look to contradict the common sense (longer inspection intervals should correspond to higher Safety Factors, and vice-versa).

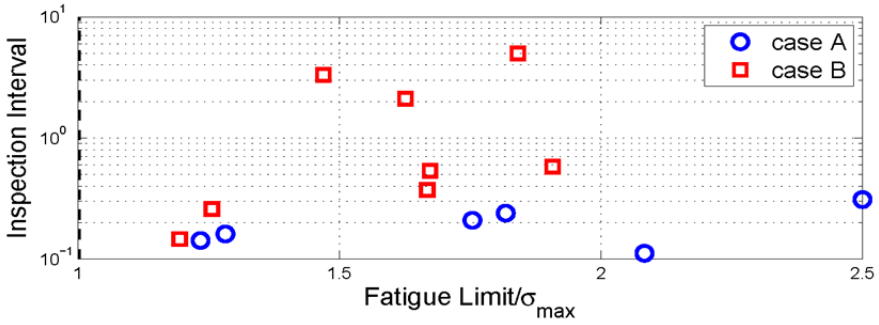

(a) Ratio between the Fatigue Limit and the maximum local stress range

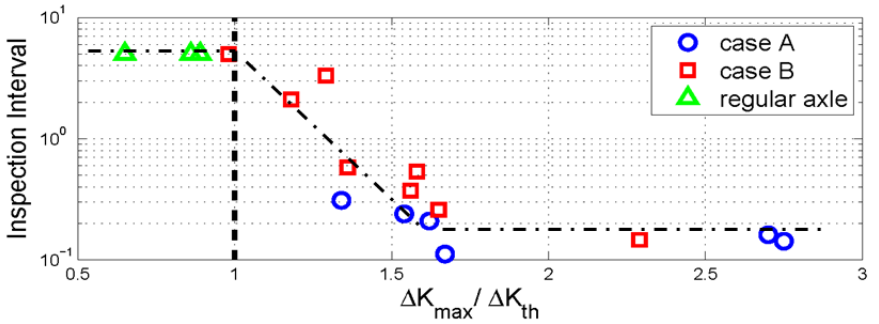

(b) Ratio between the maximum SIF and the threshold SIF

Figure 3.18: *Relationship between the relevant parameters and the estimated inspection interval*

A better indicator that can be taken for the prospective service life is the ratio between the maximum SIF and the threshold, here called 'Propagation Index', as in eq.(3.7).

$$PropagationIndex = \frac{\Delta K_{max}}{\Delta K_{th,R_{max}}} \tag{3.7}$$

where ΔK_{max} is the maximum applied SIF range for the simulated service spectrum considering an initial crack of 1 mm and $\Delta K_{th,R_{max}}$ is the threshold stress intensity factor. In particular, the residual stresses are taken into account within this latter parameter, since the stress ratio at the maximum stress range R_{max} is calculated considering the residual stresses due to wheel/disk fits.

The results are shown in Figure 3.18b: a trend of the defined inspection intervals against the defined parameter can be observed. Moreover, it can clearly be seen that when the 'Propagation Index' tends to the unity, the service lifetime (expressed in terms of the normalized inspection interval) tends to become very long, according, in this case, to the common sense.

The results of the calculation for the transitions of a regular axle (a modern axle, made of EA4T [2], compliant to the Current Regulations) are also reported onto the same graph; it can be appreciated how the propagation index is able to describe a univocal correlation with service life also for axles made of different steels and very

different shapes. It has to be here remarked that this 'Propagation Index' is only one of the possible relevant parameters which correlates with inspection intervals; this has to be regarded only as a simple first approximation of the phenomenon.

3.8 Conclusions

In this part of the research the critical issue of fatigue resistance of railway axles characterized by design not compliant with the present standard EN13103 and EN13104 was addressed. Limits and contradictions of the current regulations were highlighted, showing that the European Standards are maybe too much conservative; two test case axles, not complaint with the present normative, are in fact running without accidents since 30 years or more; this evidence was confirmed by damage calculations, as for the Miner's rule [4]. If a conservative approach is beneficial in the design approach, it cannot be applied to railway axles of 'old design', for whom an alternative methodology, for lifetime extension, is desirable. A fault-tolerant approach was defined for the purpose, based on the combined use of multi-body simulations, for the definition of realistic axle service loads, and Finite Element calculations and crack propagation models. A suitable program of non-destructive inspection intervals, allowing to keep in service old design, non Eu-compliant wheelsets until the end of their service life, was defined. The approach was applied on two tests cases representative of railway axles for suburban transportation. The relevant parameter of the European Standard for axle assessment, represented by the Safety Factor, was here discussed, finding that there is no direct correlation between this indicator and the estimated life predictions based on realistic estimation of axle load spectra and crack propagation assessment. A better indicator was here suggested as the ratio between the maximum applied stress range, considering an initial crack typically detectable during non-destructive inspection, and the threshold stress intensity factor. This simple parameter, here intended only as a first indicator, appeared to provide a better and more comprehensive indication on the inspection intervals to be considered.

CHAPTER 4

The effect of compressive residual stresses due to roll-forming onto fatigue crack propagation in railway axles

4.1 Introduction

Considering methods to improve the crack growth life of mechanical components subjected to fatigue, several surface mechanical procedures have been more and more adopted [38–40], over the last few decades, to increase their service durability and reliability. Since deep-rolling is the technological process traditionally adopted by axle producers and the damage tolerant approach, as already stated, is the design methodology, the focus was here pointed onto this particular procedure for the life extension of railway axles. In order to deepen the subject, the MARAXIL ('Manufacturing Railway Axles With Improved Lifetime') Project, supported by Regione Lombardia (Italy) [101], gave the opportunity to investigate the effect of deep-rolling onto the in-service life of railway axles made of EA4T steel, one of the standardized grades [1, 2] for the production of axles.

Firstly, special full-scale specimens were designed for variable amplitude crack propagation tests on a test bench with a 250 kNm capacity, and prepared applying the industrial deep-rolling process; the measurement of the resulting compressive residual stress field was then performed by x-ray diffraction onto the three machined specimens. The compressive residual stress field, in addition to the typical rotating bending stress state, modifies the in-service stress ratio of axles from the typical value (R=-1) to the very negative region (R=-10 or even below). For this reason, the crack propagation behavior of the material, in the unexplored region of the very negative stress ratios, lower than -2, was firstly experimentally characterized.

The three full-scale specimens were then tested, applying VA loading, considering different initial notch depths. Finally, full-scale experimental results were compared to simulated predictions carried out by a crack propagation algorithm, where the residual stresses were superimposed onto the bending stress and crack growth rate was modeled using Nasgro's propagation equations [80]. Results were extended to the case of an existing axle, in order to estimate, by simulations, the increase in service lifetime when applying the deep rolling technological process.

4.2 Characterization of the material to crack propagation

The material considered in this study is the EA4T (quenched and tempered 25CrMo4) steel grade, one of the standardized steels used for the production of railway axles [37] running in Europe. Due to the superposition of the very high compressive residual stresses, expected as the consequence of the deep-rolling technological process, and the stresses due to the in-service rotating bending, the stress ratio acting at the surface of the axle will be different, in particular much lower, than the typical R=-1 value due to rotating bending alone. From this point of view, a dedicated experimental campaign was then carried out, in order to investigate the crack propagation behavior of the A4T grade in the not-yet-explored region of very negative stress ratios. In particular, two different shapes of specimen were tested:

- 12x24 mm SE(B) specimen with an 8 mm initial notch length obtained by electro-discharging manufacturing (EDM), 12 samples;
- 20x50 mm SE(T) specimen with a 7 mm initial notch length obtained by EDM, 4 samples.

As known from the literature (see chapter 1), the traditional experimental technique (ΔK-decreasing, [58]) for generating threshold SIFs overestimates their values. For this reason, all the adopted specimens were prepared using the compression pre-cracking approach.

Specimens were pre-cracked in compression, in order to induce a non propagating sharp crack out of the machined notch; pre-cracking was carried out applying four points bending, as in the schematic of Figure 4.1a, adopting a servo-hydraulic mono-axial facility, equipped with a 100 kN load cell and a dedicated device, as in Figures 4.1b and c. The load was chosen in order to generate a 130 Nm bending moment at a stress ratio R=10; about 10^6 cycles, at a frequency of 30 Hz, were needed in order to obtain a naturally arrested crack of about 0.3 mm length; an example of the obtained pre-cracks is shown in Figure 4.1d.

Crack propagation tests onto SE(B) specimens were carried out using a Rumul Craktronic resonant plane bending facility, in Figure 4.2, working at a frequency equal to about 130 Hz; crack length was measured, at both sides of the crack, using crack-gages and a dedicated central unit, by the meaning of the potential drop technique. A total of 12 SE(B) specimens were tested at different stress ratios ranging from R=0.7 to R=-2.5. At every considered stress ratio, both the crack growth rate and the threshold SIF were investigated by means of the 'Compression Pre-cracking Constant Amplitude' (CPCA) [74] and the 'Compression Pre-cracking Load Reduction' (CPLR) [69] tests, respectively. In order to obtain relevant results for even more negative stress ratios,

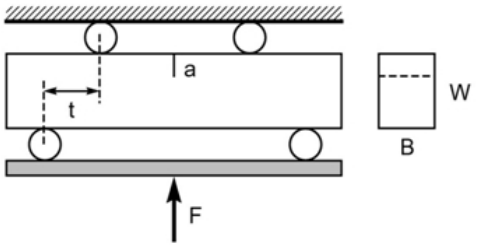

(a) Schematic of the compressive four points bending

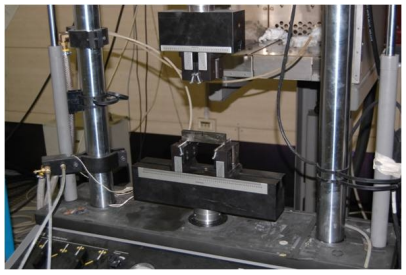

(b) Mono-axial servo-hydraulic facility

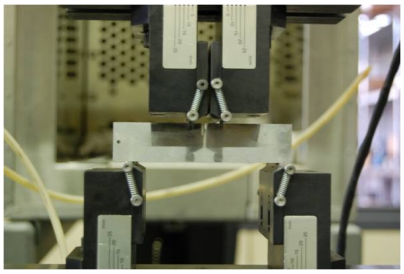

(c) Detail of the device for applying four points bending

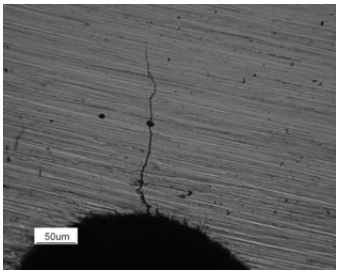

(d) Example of resulting pre-crack

Figure 4.1: *Experimental setup for pre-cracking in compression the SE(B) specimens*

a total of four SE(T) specimens were tested by a servo-hydraulic mono-axial facility instrumented with a 250 kN load cell, at different stress ratios ranging from R=-2.5 to R=-4.

Figure 4.3a shows the obtained experimental fatigue crack growth curves together with their interpolations carried out adopting the Nasgro equation [80] and the maximum likelihood method [93]. The same diagram also shows a comparison to the interpolation of experimental data [102] obtained by the traditional ΔK-decreasing approach for the same material. It is worth noticing the tendency of data to overlap at very negative stress ratios: all the tests carried out at R≤ -2 collapsed on the experimental data obtained at R=-2, suggesting a stabilization of the crack propagation behavior of the considered material at very negative stress ratios. This is also in agreement with the declared validity of the Nasgro equation for thresholds [80] over the stress ratio range $-2 \leq R \leq 0.7$.

Figure 4.3b shows the trend of the ΔK_{th} against the stress ratio, as obtained from the present experimental campaign, and compares it to data from the literature [102] obtained by the application of the ΔK-decreasing technique to the same material. Experimental data were interpolated by the Nasgro equation for thresholds [80], adopting, again, the maximum likelihood methodology. It is evident that the compression pre-cracking technique results in lower thresholds when compared to the traditional approach and that such a difference significantly increases decreasing the stress ratio. Thresholds (Figure 4.3b) and crack growth curves for R<-3 were considered constant, based on the observations onto Figure 4.3a.

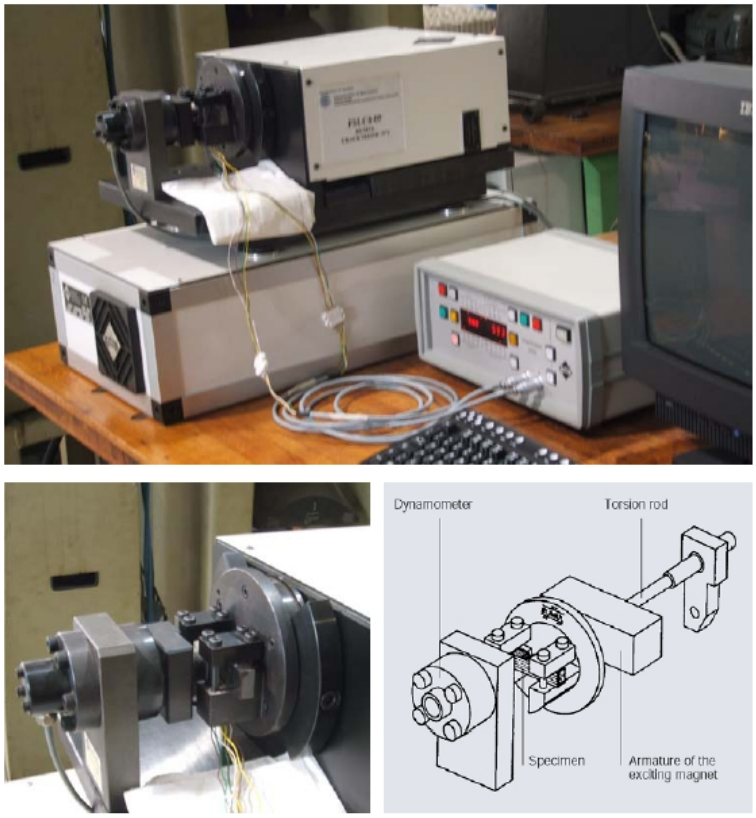

Figure 4.2: *Rumul resonant facility, applying plane bending, for the crack growth characterization*

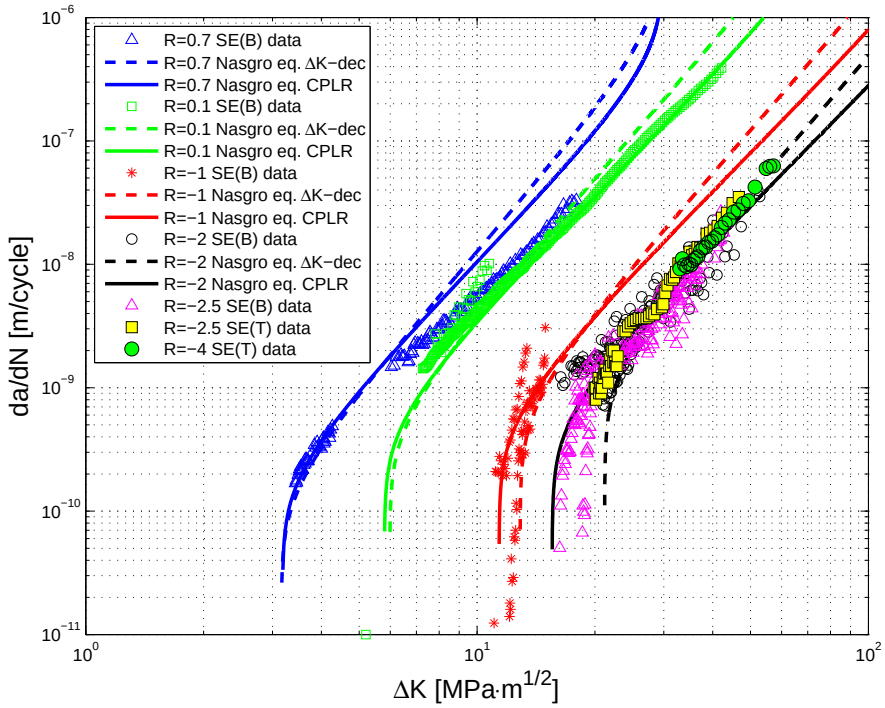

(a) Crack growth curves

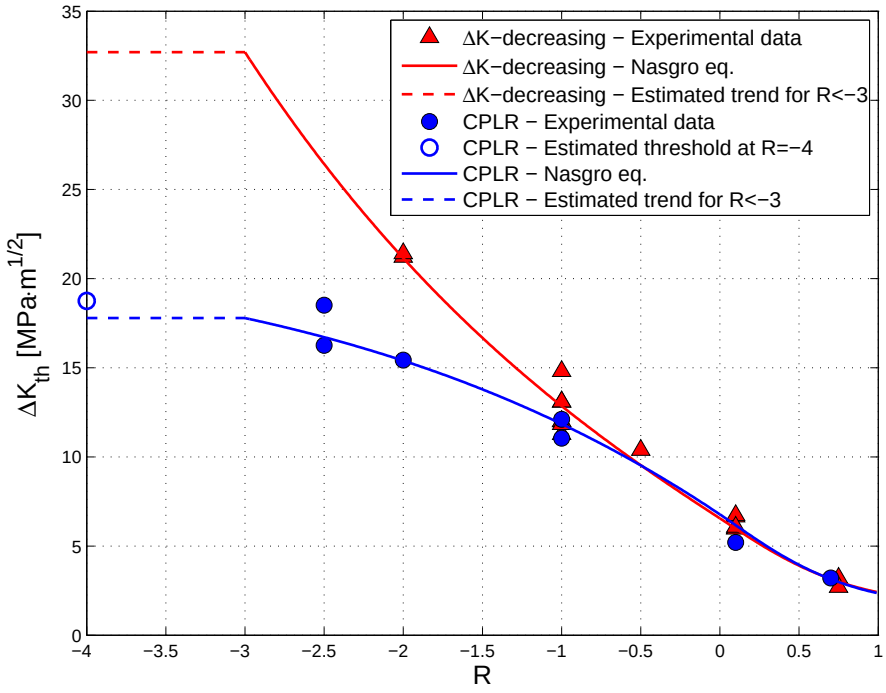

(b) Trend of threshold SIF with stress ratio

Figure 4.3: *Crack growth behavior of EA4T steel grade*

4.3 Full-scale test details

4.3.1 Specimens and test details

The adopted full-scale specimen, shown in Figure 4.4a, was specifically designed, according to the relevant standard [37], for the three point rotating bending bench (Figure 4.4b), having capacity 250 kNm, available at Politecnico di Milano - Dept. Mechanical Engineering. A portion of such a specimen, characterized by a lowered diameter equal to 130 mm, was subjected to the particular deep-rolling procedure used to produce deep-rolled axles for high-speed applications in Europe. In particular, the lower diameter of the deep-rolled portion of the specimen was adopted to overcome the high compressive residual stresses and to allow for crack propagation.

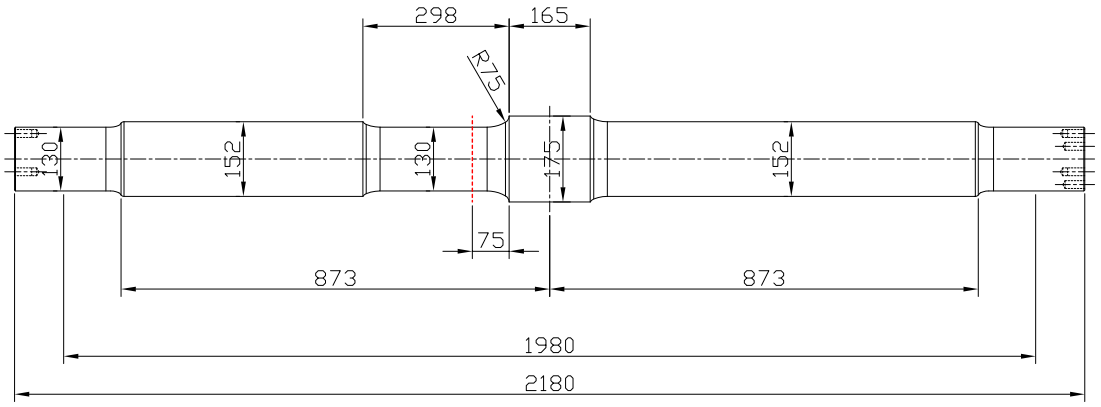

(a) Drawing of the specimen

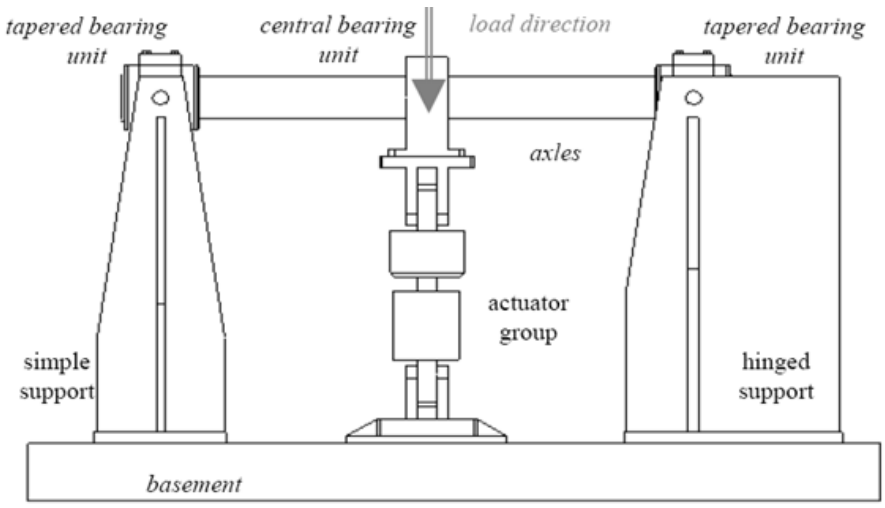

(b) Scheme of the three point rotating bending facility

Figure 4.4: *Experimental set-up for testing full-scale deep-rolled specimens*

After deep rolling, two semi-circular artificial defects were introduced, by EDM and at 180° to each other, into the deep-rolled portion of each specimen. In particular, three specimens were prepared, differing for the initial artificial notch radius: 2 mm, 3 mm and 4 mm. These particular dimensions were chosen based on the residual stress

profiles measured according to Section 4.3.2. Specimens were then subjected to both Constant Amplitude loadings (CA) and Variable Amplitude sequences (VA), derived from a typical in-service load spectrum available in the literature [14] and representative of about 57000 km of high-speed service. The continuous load spectrum and its discretization as load blocks are shown, normalized, in Figure 4.5a. The stress magnification was chosen in order to obtain an equivalence, in terms of the maximum ΔK value, equal to 16.70 MPa$\sqrt{\text{m}}$, between the specimen and the real in-service axle, both containing a 2 mm defect; this magnification, corresponding to a maximum amplitude stress level of 165 MPa at the notched section, will be called '100% amplitude' in the following. Finally, an appropriate cut level was chosen, in the lower load amplitudes, at a stress value corresponding to a ΔK of about 50% of the expected ΔK_{th}, when considering the smaller notch size; this cut level allowed to reduce the length of the spectrum to about 41000 cycles, thus preserving the correspondence with the original mileage.

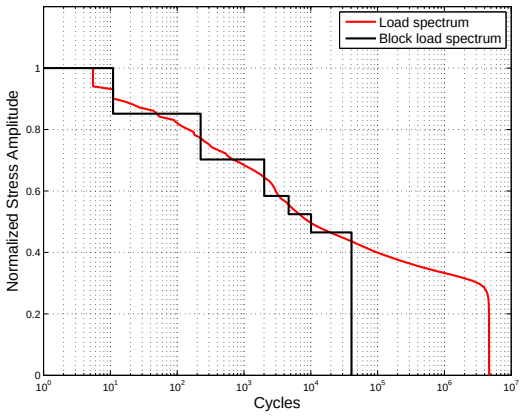

(a) Normalized block load spectrum, against the continuous original spectrum

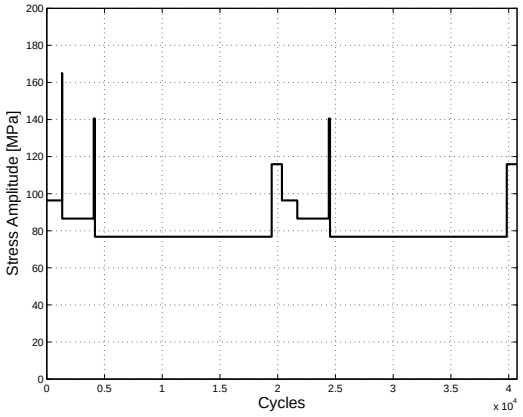

(b) Applied block load sequence (100% amplitude)

Figure 4.5: *Applied load spectrum, in terms of stress amplitudes, adopted for testing the full-scale specimens*

Actually, the shape of developing cracks immersed into a residual stress field is not very well known, so, during full-scale tests, the monitoring of crack growth was carried out using both visual (by an optical microscope and plastic replicas [103]) and ultrasonic (single crystal and phased array approaches) testing. In particular, visual testing (VT) was applied to monitor any possible propagation at the surface and at the internal bottom of the artificial notches, while ultrasonic phased array testing (UPAT, S-Scan, 32 active elements, 5 MHz) to monitor in-depth crack tip propagation by means of the 'crack tip diffraction' method [104]. Traditional single-crystal ultrasonic testing (UT, 4 MHz, 45°) was, instead, applied to monitor the general increase of the dimension of the defects by acquiring the amount of reflected sound energy in terms of gain needed to get the amplitude of the signal response up to the 90% of the screen of the flaw detector unit. In the following, the characterization of the residual stress profiles, before and after the full-scale crack growth tests, is firstly given, followed by the description of the full-scale tests themselves.

4.3.2 Measurement of the residual stress profile in the full-scale specimens

The residual stress profile was experimentally derived by X-ray diffraction (XRD, [105, 106]]) in order to quantify its longitudinal and circumferential components. In particular, an AST X3000 X-Ray diffractometer was used. Before each crack propagation test, three different sections of the deep-rolled region of each specimen, one of which containing the artificial notches (Figure 4.6a), were measured at three different surface points (0°, 120° and 240°), so not to introduce stress raisers and initiate unwanted cracks. The same sections and points were measured again at the end of the tests to understand whether the fatigue phenomenon could influence the amount of residual stresses. The surface residual stresses along the length of the axle resulted to be fairly uniform, section by section, and equal, in the section containing the artificial notches, to about -600 MPa along the longitudinal direction (Figure 4.6a for the example of the specimen containing 2 mm deep notches) and about -300 MPa along the circumferential one. Such a magnitude of residual stresses suggests an effective prospective action against crack propagation in full-scale axles, where, usually, the maximum in-service stress amplitude is lower than 200 MPa. Moreover, the applied fatigue cycles were not able to modify the residual stress field (Figure 4.6a), since the mean profile after the test remained comparable to the same before the test itself.

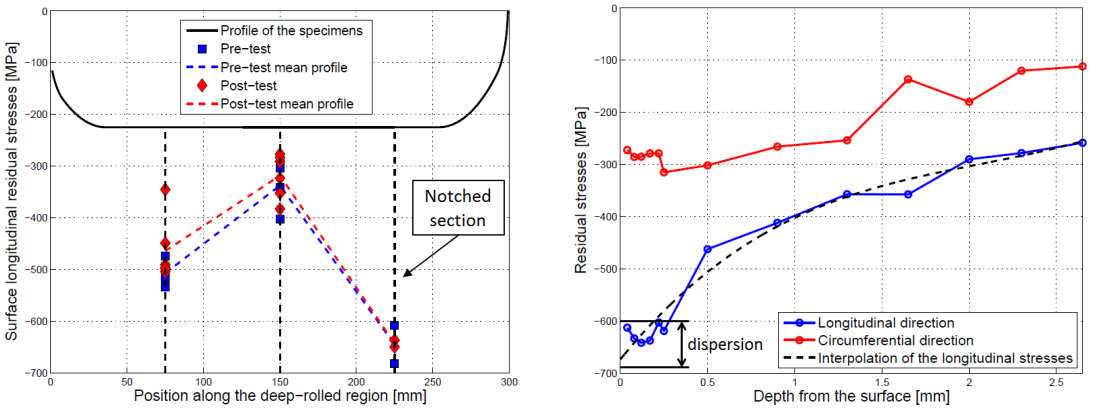

(a) At the surface, before and after the crack propagation test

(b) In-depth measurement, along the notched section, at the end of the test

Figure 4.6: *Residual stress profiles into the full-scale specimen containing 2mm deep notches*

At the end of the fatigue tests, some of the measuring spots were also investigated, again by XRD, to determine the in-depth residual stress profile. In particular, slices of material, of about one tenth of millimeter, were locally and progressively removed by electro-polishing, using a solution of acetic acid (94%) and perchloric acid (6%), in order not to affect the pre-existing stress field. The residual stresses pattern was determined down to a 2.5 mm depth. Figure 4.6b shows, as an example, the residual stress patterns of the section containing the 2 mm deep artificial notches: it is worth noticing that all the specimens showed an analogous behavior. It clearly appears that the residual stresses tend to decrease rapidly close to the surface, reaching a zero value between 3 and 4 mm depths. This explains the choice made about the size on the initial notches.

4.4 Results of the full-scale tests

Specimen	Test	Equivalent Distance [km]	Cycles	σ_{max} [MPa]	ΔK_{max} [MPa$\sqrt{m}$]	Crack Propagation
$a_0 = 2$mm	CA	-	$10 \cdot 10^6$	125	12.65	no propagation
	VA 100%	$4 \cdot 10^6$	$2.73 \cdot 10^6$	165	16.70	no propagation
	VA 125%	$3.5 \cdot 10^6$	$2.62 \cdot 10^6$	206	20.88	no propagation
$a_0 = 3$mm	VA 100%	$2 \cdot 10^6$	$1.43 \cdot 10^6$	165	20.72	no propagation
	VA 125%	$2 \cdot 10^6$	$1.43 \cdot 10^6$	206	25.90	no propagation
	VA 150%	$2.2 \cdot 10^6$	$1.57 \cdot 10^6$	247	31.08	no propagation
	VA 175%	$4.9 \cdot 10^6$	$3.50 \cdot 10^6$	288	36.26	initiation of cracks from notches
	VA 200%	$5 \cdot 10^6$	$3.57 \cdot 10^6$	330	41.44	stable crack propagation, at both artificial notches, until final failure of the specimen
$a_0 = 4$mm	VA 100%	$3.5 \cdot 10^6$	$2.60 \cdot 10^6$	165	23.80	stable crack propagation, at both artificial notches

Table 4.1: *Experimental plan applied to the tested specimens*

4.4.1 Specimen with 2mm deep initial notches

The obtained XRD measurements show that 2 mm deep defects were completely immersed into the compressive residual stress field. The first part of the test then consisted in subjecting the specimen to a constant amplitude load generating 125 MPa at the notched section. This stress level corresponds to a ΔK value of 12.65 MPa$\sqrt{m}$ at the bottom of the notches, slightly higher than the threshold SIF range at R=-1 as shown in Figure 4.3b. Ten million cycles were applied and no crack growth could be observed at both the surface and the deepest point of the notches. The specimen was then subjected to the VA loading sequence, already shown in Section 4.3.1, in the 100% amplitude. Such a block load sequence was applied for 2.73 million cycles, corresponding to approximately $4 \cdot 10^6$ km, and, since no crack propagation was again detected, its stress levels were increased by 25%, corresponding to a maximum SIF equal to 20.88 MPa$\sqrt{m}$, for another equivalent distance equal to approximately $3.5 \cdot 10^6$ km. All the details of the test are collected in Table 4.1.

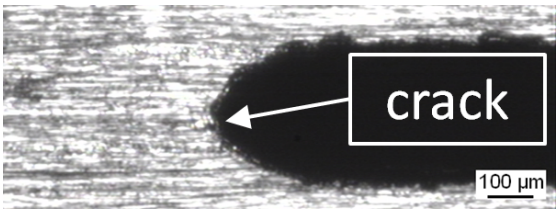

Figure 4.7: *Visual inspection of the surface tip of one of the artificial notches at the end of the test*

In the end of this part of the test, the 2 mm notches showed the presence of very short cracks, observed by optical microscope, with an average length of 0.1 mm. In particular, Figure 4.7 show, as examples, the state of the internal bottom and of one of the surface tips of one of the notches, respectively. It is worth noticing that the dimension of the observed surface cracks could be quantified in an average value equal to about 0.1 mm.

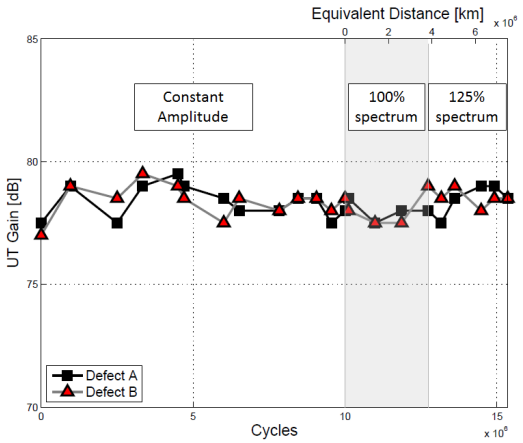

(a) Monitoring by UT over the whole test

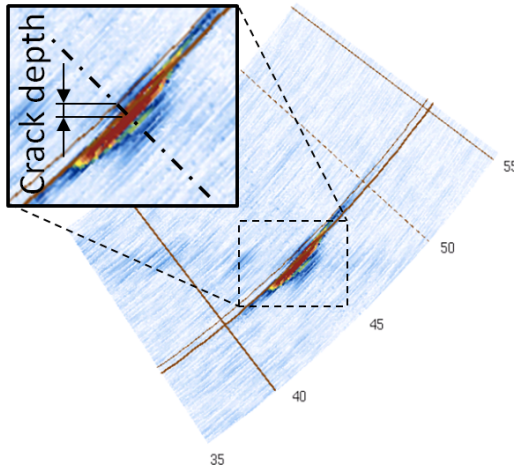

(b) Example of crack depth measurement from a PAUT acquisition

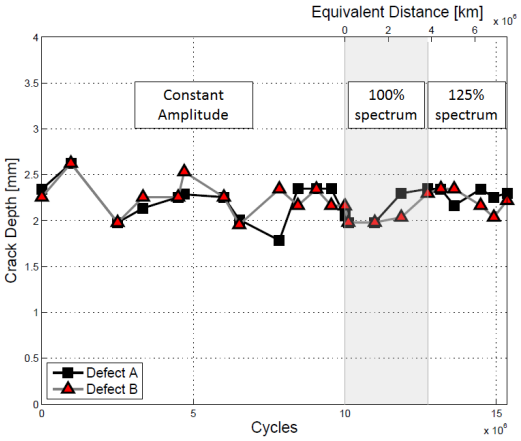

(c) Estimation of crack depth by PAUT over the whole test

Figure 4.8: *Measurements of crack growth from 2 mm deep notches*

On the other hand, both UT (Figure 4.8a) and PAUT (Figure 4.8b and 4.7c) suggested no propagation at all. This fact can be explained noticing (Figures 4.7a and 4.7c) that 0.1 mm is a variation of the radius of the defect smaller than the intrinsic standard deviation of the applied UT and UPAT procedures. Finally, the axle was suitably broken in order to observe, by the scan electron microscope (SEM), the surface of the initial notches. Indeed, the whole edge of the notches (Figure 4.9 shows an example) confirmed the onset of a very small cracks, which can be interpreted as non-propagating and likely related to the plasticity of the material around the tips of the

artificial notches.

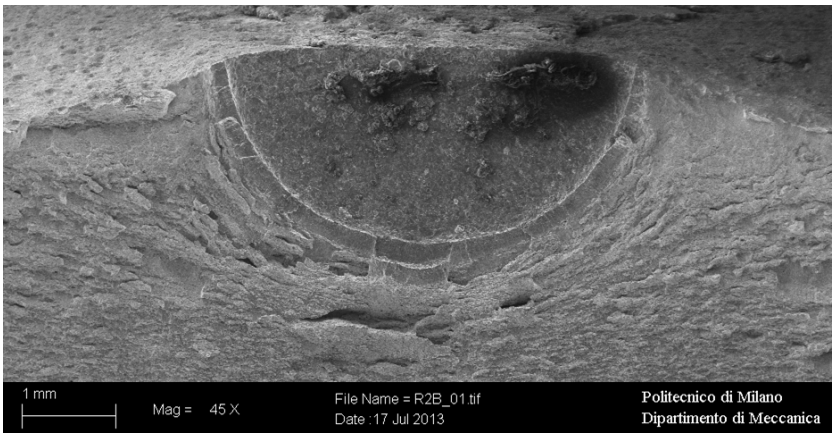

Figure 4.9: *SEM fractography of one of the 2 mm notches at the end of the fatigue test*

4.4.2 Specimen with 3mm deep initial notches

The axle containing the initial 3 mm deep notches was tested because this depth roughly corresponds to the vanishing of the residual stresses due to deep rolling, see Section 4.3.2 and Figure 4.6b. The focus was here particularly pointed to variable amplitude loading, considering the same load spectrum already taken into account. The test started with the application of the 100% amplitudes. Since no crack growth was observed after 2 equivalent million kilometers, the amplitude of the spectrum was gradually increased till crack propagation occurred. All the details about the experiment are reported in Table 4.1. For every load amplitude, a minimum distance of about 2 equivalent million kilometers was applied, in order to allow for any possible crack growth. As can be observed from Table 4.1, the maximum SIF acting at the bottom of the crack was always higher than the threshold at R=-1.

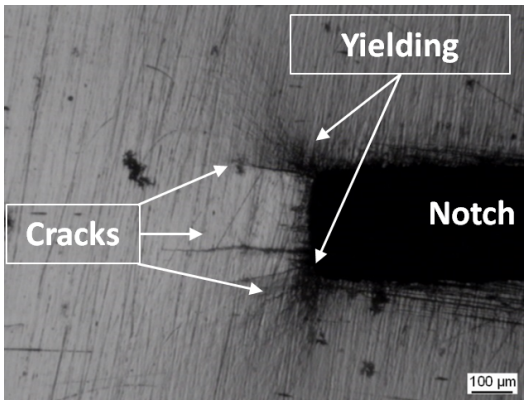

(a) Condition of one of the tips of the notches at the end of the 175% amplitude block load sequence

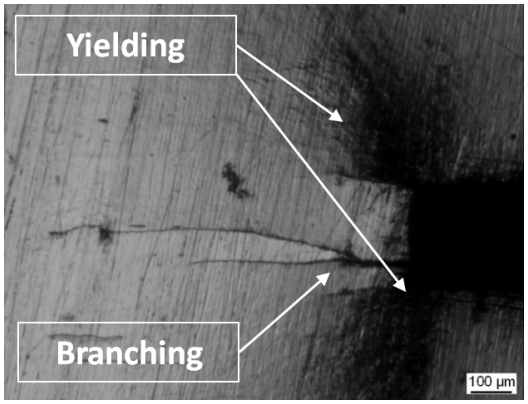

(b) Condition of the crack tip shown in (a) after about 4 million km at 200% amplitude block load sequence

Figure 4.10: *Monitoring of crack growth, by optical microscope, during the full-scale test on 3 mm deep artificial notches*

The developing cracks were periodically inspected, using again the described VT, UT and UPAT techniques, at suitable test interruptions. Considering, as an example, a tip of one of the notches, Figures 4.10a and 4.10b show its surface condition at the end of the 175% amplitude load sequence and after 4 million cycles of the 200% amplitude load sequence, respectively. It is interesting to notice that, around the notch, the material yielded considerably. This suggests that the rotating bending stresses were very high around the notch, but also that the residual stress field was very effective in avoiding initiation and propagation of fatigue cracks, at least up to a magnification of the load levels equal to 175%. It is also worth observing the very complex crack damage pattern: three different initiation sites can be seen in Figure 4.10a (two at the corners of the notch and one along its lateral edge), but just one developed in a propagating crack (Figure 4.10b) which also showed a branching phenomenon.

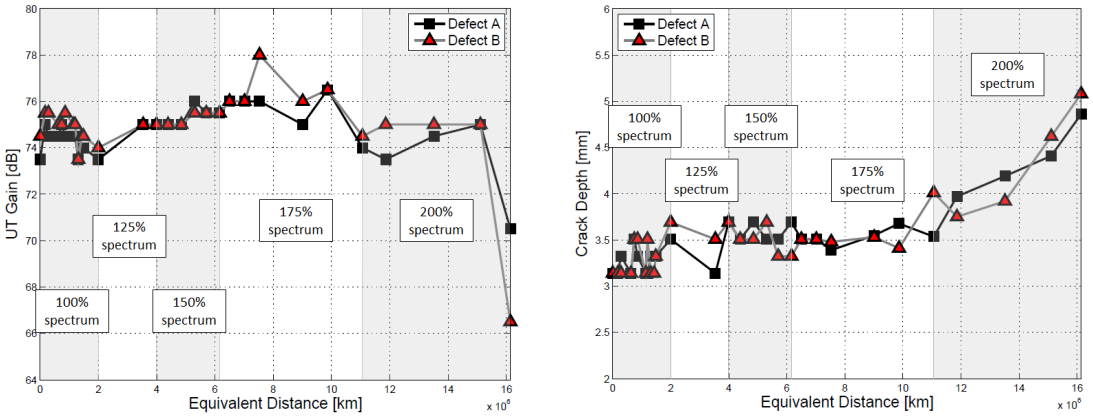

(a) Monitoring by UT over the whole test

(b) Estimation of crack depth by PAUT over the whole test

Figure 4.11: *Monitoring of crack growth, by ultrasonic inspections, during the full-scale test on 3 mm deep artificial notches*

As can be seen from Figure 4.11a, UT does not seem very effective to investigate crack propagation, since no significant differences could be observed over the whole test, a part for the final fracture of the specimen. A crack advance could, instead, be clearly measured (Figure 4.11b) by PAUT, starting from the second half of the 175% amplitude block load sequence. This was in accordance with the just described optical measurements.

At the end of the test, one notch fastly developed a large crack, breaking the specimen, while the other one showed only a little crack advance; the specimen was then properly cut and broken in liquid nitrogen, in order to observe the shape of the developing crack. A fractography of the notch which developed in a big crack is shown in Figure 4.12. The beach marks, indicating particular events during block loading test, are evident from the picture; particularly, it is evident that these marks have not the typical semi-elliptical shape, but tend to close, on the free surface of the axle, close to the initial notch. This means that the crack developed firstly under the surface, changing the crack shape from the typical semi-elliptical one, due to the presence of the negative residual stresses. Even if this evidence was expected, it is important to remark that the predictive model, based onto the Shiratori weight's functions, is only able to deal with

semi-elliptical crack shapes.

Figure 4.12: *Fractography of the 3 mm notches, which developed in a big crack, at the end of the fatigue test*

A higher magnification of the crack developing from the 3 mm initial notch was obtained by SEM inspections (Figure 4.13); from this fractography, beach marks are again evident.

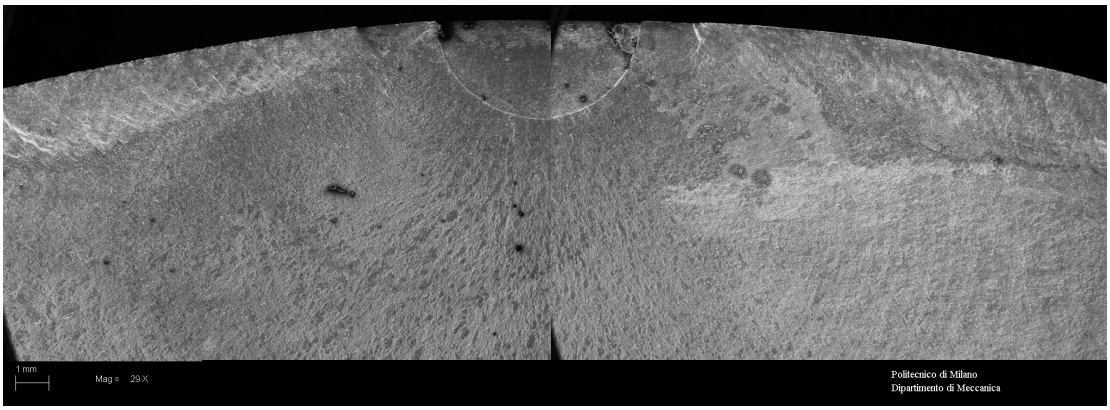

Figure 4.13: *SEM fractography of the 3 mm notch, which developed in a big crack, at the end of the fatigue test*

A SEM fractography of the other initial notch, which showed a smaller propagation, is shown in Figure 4.14a; Figure 4.14b shows the same notch under optical microscope. These two images confirm the crack shape development: the crack is bigger in the radial direction (at the bottom point) than at the free surface; moreover, the appearance of the notch surroundings reveals the same aspect as the 2 mm notch, suggesting the developing of an initially non-propagating crack.

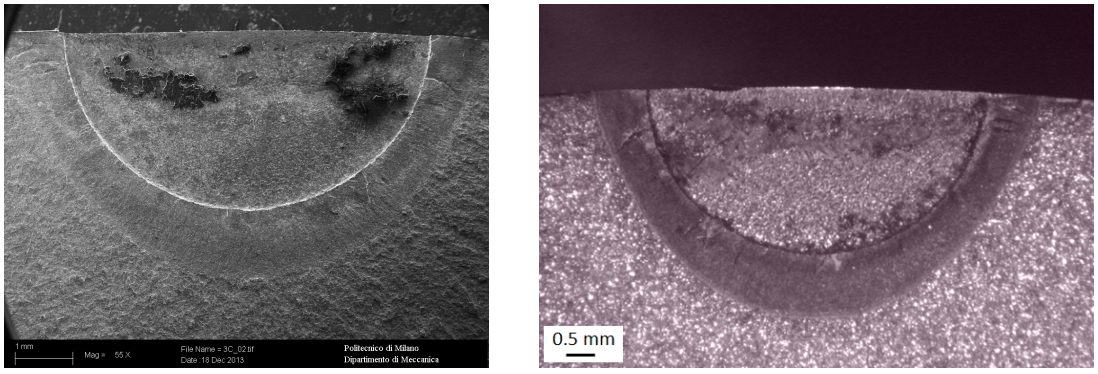

(a) SEM fractography

(b) Image by optical microscope

Figure 4.14: *Appearance of the 3 mm notch, which showed a small crack advance, at the end of the test*

4.4.3 Specimen with 4mm deep initial notches

The full-scale specimen containing initial 4 mm deep notches was tested just using the 100% amplitude block load sequence, as in Table 4.1. This stress amplitude corresponded, due to the 4 mm crack depth, to a maximum SIF of about 23.8 MPa$\sqrt{\text{m}}$. The aim of this experiment was to check the effectiveness of deep rolling against crack propagation considering the worst scenario of a quite deep crack, i.e. exceeding the depth of residual stresses. The test lasted for 64 repetitions of the block load sequence, corresponding to an equivalent distance of about $3.5 \cdot 10^6$ km, and was interrupted before the failure of the specimen.

The notches were again monitored by both VT, UT and PAUT techniques: Figures 4.15a and 4.15b show the surface condition, via optical observation of plastic replicas, at the 17^{th} and the 64^{th} repetitions of the block load sequence, respectively. As can be seen, developing surface cracks were found, but they advanced for a limited distance and showed an interesting behavior: they became non-propagating after about 35 repetitions of the block load sequence (Figure 4.15c). This can be again explained considering the local relaxation of compressive residual stresses due to the introduction of the notches. Moreover, as for the case of 3 mm deep notches, two cracks initiated at every notch tip, suggesting again a peculiar and complex damage pattern due to the presence of deep-rolling residual stresses.

Considering UT, Figure 4.16a shows the amount of reflected sound energy over the whole test. The trend is slightly decreasing suggesting the presence of propagation, but it is also clear the energy variation is quite small and this method is, again, not very effective. Measurements by UPAT resulted to be more interesting and sizable: Figure 4.16b shows the experimental estimation of crack depth. As can be seen, the crack propagated up to about 5 mm during the whole test. This suggests that the shape of cracks, during propagation in the residual stress field, does not likely correspond to the expected one from classical fatigue.

Finally, also this specimen was broken, in order to observe by SEM the surface of the initial notches. Around the whole edge of the notch (Figure 4.17a), a small circle, similar to the one already shown for the 2 mm notch axle, is evident. Anyway, out of the first small region, a second one appears, as in the detail of Figure 4.17b,

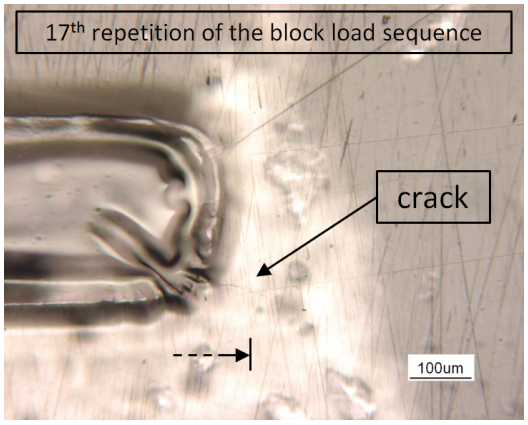

(a) Appearance of one of the tips of Defect B at the end of the 17^{th} repetition of the block load sequence

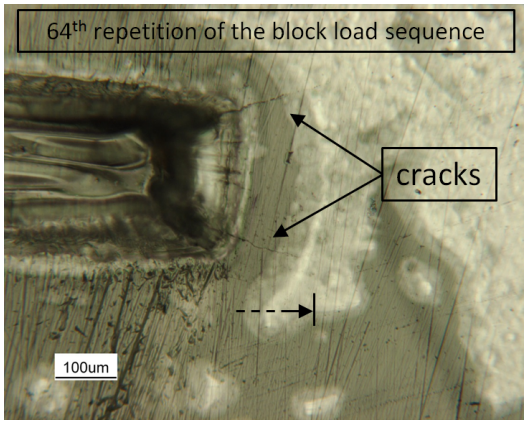

(b) Appearance of the crack tip shown in (a) at the end of the 64^{th} repetition of the block load sequence

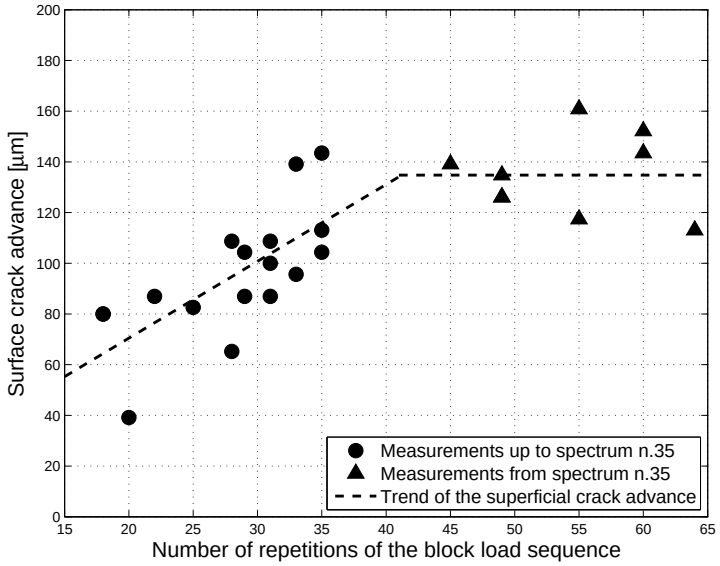

(c) Trend of the surface crack advance, during the test

Figure 4.15: *Monitoring of crack growth during the full-scale test on 4 mm deep artificial notches*

characterized by several different cracks, onto different planes, tending to coalesce. The total dimension of the crack is in agreement with UPAT measurements.

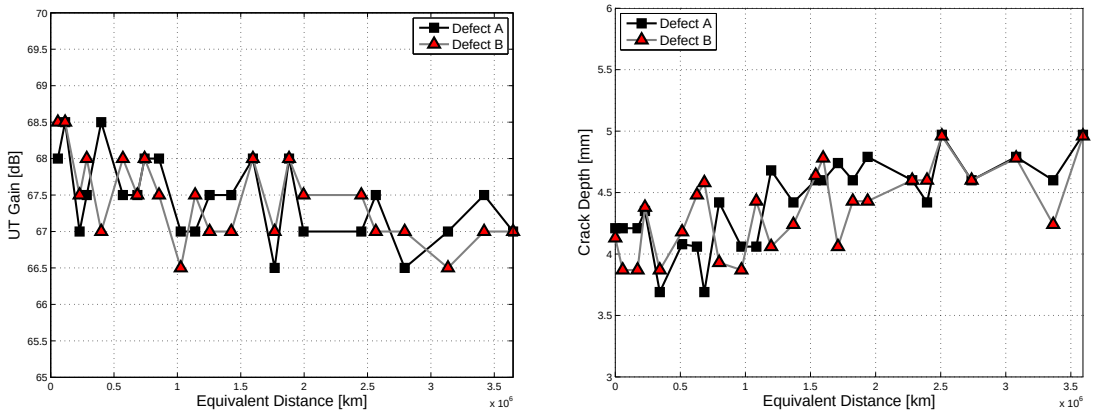

(a) Monitoring by UT over the whole test

(b) Estimation of crack depth by PAUT over the whole test

Figure 4.16: *Measurements of crack growth from 4 mm deep notches*

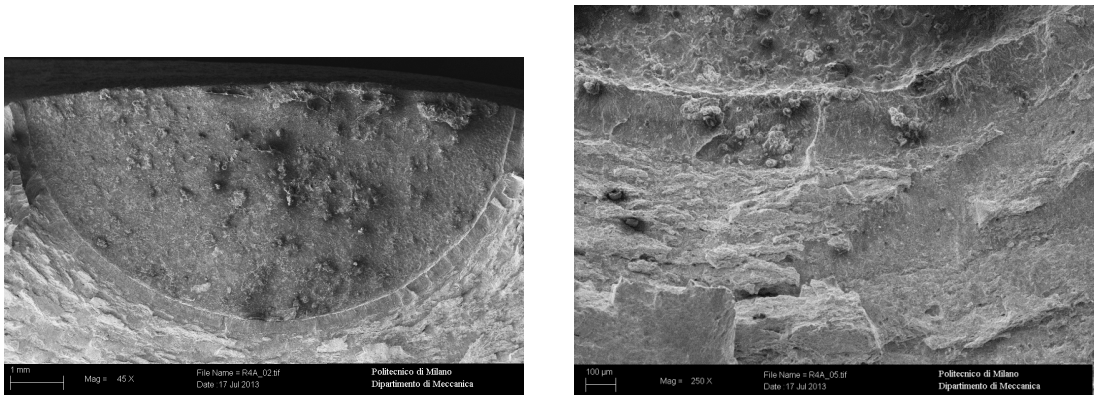

(a) SEM of one 4 mm notch

(b) Detail of the propagation from SEM fractography in (a)

Figure 4.17: *SEM fractography of one of the 4 mm notches at the end of the fatigue test*

4.5 Crack growth lifetime predictions of full-scale specimens

For determining the SIFs in the prospective crack plane, the experimental longitudinal residual stress profile along the depth, described in Section 4.3.2, was considered and properly interpolated (Figure 4.6b). The stresses due to rotating bending were instead determined by the dedicated finite element (FE) model shown in Figure 4.18. In particular, a 3D solid model was built, taking advantage of all the possible symmetries. Hinge-roller constraints were defined at the bearings, while the load was applied in the middle section of the central press-fit seat. A structured mesh was built, consisting in 20-node hexahedral elements with reduced integration, having global dimension 10 mm but reduced to about 1 mm along the deep-rolled portion of the axle. Results are here shown as the nodal average of the values extrapolated from Gauss quadrature points.

The rotating bending longitudinal stress profile along the prospective crack plane was then derived and suitably interpolated for the application of Shiratori's solution. Several crack growth simulations were carried out, considering all the different initial

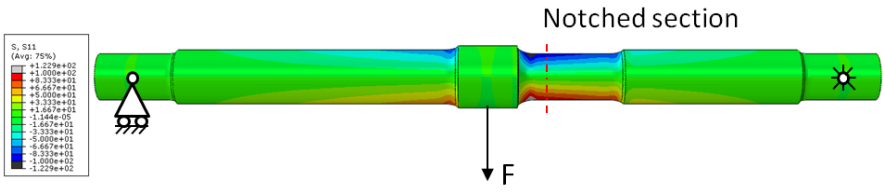

Figure 4.18: *FE model for the evaluation of the stresses, in the perspective crack plane, due to rotating bending*

notch sizes of the tested specimens and using the same block load sequence of the experiments.

A summary of the adopted crack growth algorithm is given in the following:

- given a block load level, calculation of the stress ratio acting at points A and C of the crack, due to the superposition of the rotating bending stresses and the residual stress field;
- independent evaluation of the crack growth rate, given the stress intensity factor ΔK and the stress ratio R, for both points A and C using the Nasgro equations [80] calibrated by the parameters experimentally derived from small-scale specimens. Different simulations were carried out considering both ΔK-decreasing and CPLR data;
- definition of the actual crack shape, which acted as an input for the following block load.

The block load sequence was repeatedly applied up to failure or to the natural end of the corresponding test. Figures 4.19, 4.20 and 4.21 show the estimated crack growth predictions compared to experimental outcomes for 2, 3 and 4 mm deep initial notch, respectively. In particular, Figure 4.19 shows that a 2 mm deep notch, completely immersed in the compressive residual stress field due to deep rolling, is not able to propagate, at least under the considered load levels. This conclusion is in agreement with the experimental outcome. It is also worth noticing that a specimen without deep rolling would have failed during the test at CA. It can be concluded that deep rolling actually has an important influence on crack growth life of axles.

Figure 4.20 shows the obtained crack propagation predictions for the 3 mm deep initial notch. In this case, the positive influence of deep rolling is evident, too. Moreover, ΔK-decreasing data provide longer crack growth predictions than CPLR ones. As can also be seen, the best match to experimental results is achieved at the beginning of the test, while some divergence is observed towards the final part. It remains that simulations are always conservative with respect to experiments. The discrepancy between simulated and experimental results can be explained by the uncertainty about the real depth of the residual stress profile, which could not be measured. In particular, simulations adopted the exact profile shown in Figure 4.6b, which is valid until a 2.5 mm depth, but which also suggests a deeper influence of residual stresses on the growing crack. This means that the slowing effect of compressive residual stresses lasted longer in the tests, increasing the retardation effect on propagation with respect to simulations.

In the end, the predictions regarding the specimen containing the 4 mm initial notch are shown in Figure 4.21. The effect of deep rolling and the choice of threshold data

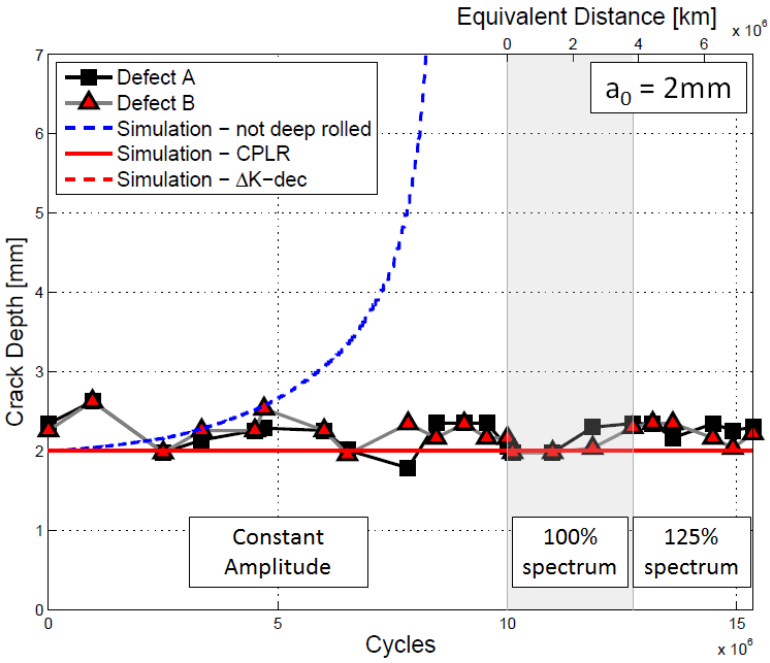

Figure 4.19: *Crack growth predictions for the 2 mm deep notch*

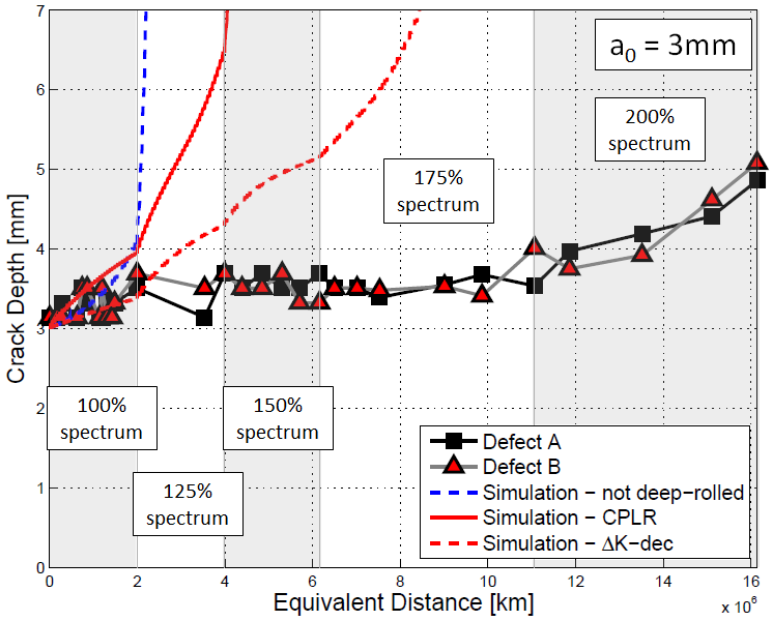

Figure 4.20: *Crack growth predictions for the 3 mm deep notch*

on crack growth in axles support the already drawn conclusions. In this case, a good agreement between predictions and experiment was found. In particular, experimental data match well with the prediction carried out considering deep rolling effects and ΔK-decreasing data, i.e. the 'slowest' considered configuration. Moreover, this result supports the observation made in the case of the 3 mm deep notch about the uncertainty of the deepest residual stress profile: it likely does not overtake a 4 mm depth, making

experiments and simulations match.

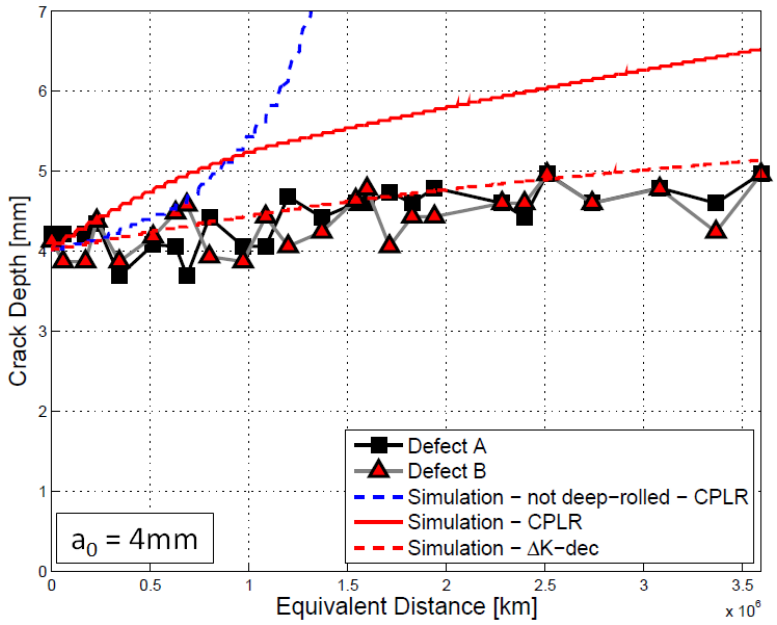

Figure 4.21: *Crack growth predictions for the 4 mm deep notch*

4.6 Lifetime predictions for an axle from real production

The developed algorithm for life predictions under a compressive residual stresses field was extended to the case of an axle, coming from real production, and subjected to the same deep-rolling procedure of the tested full-scale specimens. The schematic of the analyzed railway axle, typically adopted for high-speed service, is shown in Figure 4.22. Firstly, the residual stresses due to the technological deep-rolling procedure were measured, then, lifetime predictions were carried out, based on the developed algorithm.

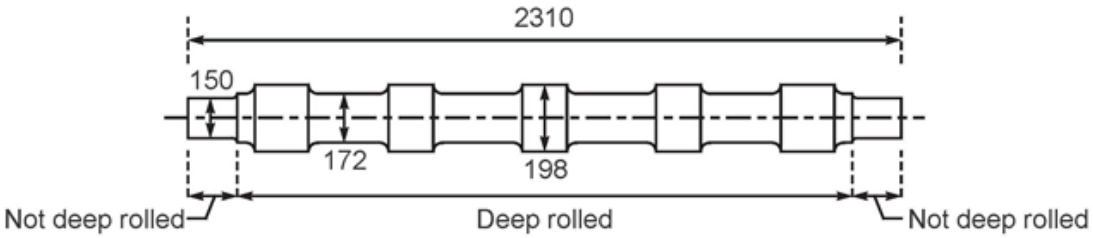

Figure 4.22: *Scheme of the investigated deep-rolled axle*

4.6.1 Residual stresses measurements

A full-scale axle, made of the same EA4T steel grade of the tested full-scale specimens, was deep-rolled along the body (including transitions) and all the seats of wheels and disk-brakes, but not along the bearing journals. Deep rolling was applied using the

same procedure already applied onto the three tested specimens. This axle was just used for the measurement of residual stresses, since no fatigue test was planned and carried out. In particular, eighteen different sections, represented in Figure 4.23, of the axles were investigated by XRD using the same equipment and procedure already described for the full-scale specimens (Section 4.3.2).

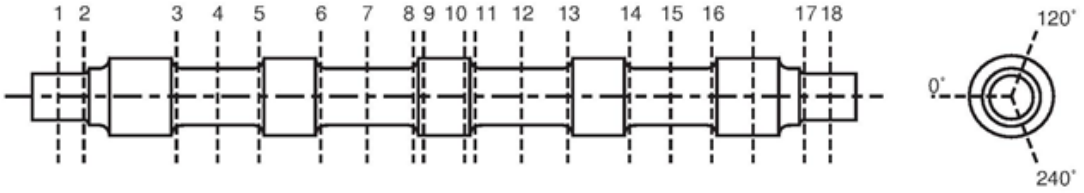

Figure 4.23: *Experimental XRD measurement of the residual stress pattern: measurement sections*

The surface residual stresses along the length of the axle (Figure 4.24a) resulted to be quite uniform and equal to about -850 MPa along the longitudinal direction and about -400 MPa along the circumferential one. The not deep-rolled bearing journals showed, instead, stress levels equal to about -150 MPa along the longitudinal direction and about +100 MPa along the circumferential one. It is also worth noting that the longitudinal and circumferential directions corresponded to the principal ones.

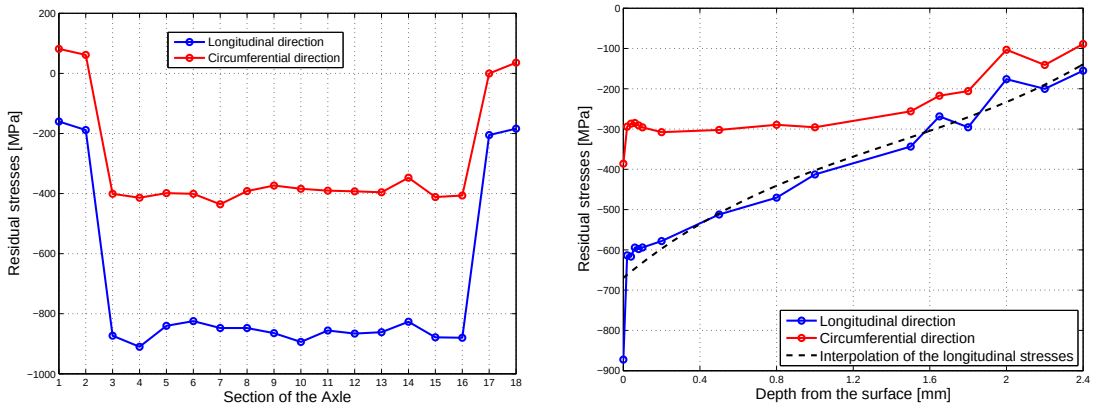

(a) Along the surface (mean value of the three measurements for each section)

(b) In-depth, section 14 at 0°

Figure 4.24: *Residual stress pattern in the investigated full-scale axle*

The residual stresses profile was also determined, down to about 2.5 mm, at some of the measuring spots, by subsequent electro-polishing and X-ray measurements. Figure 4.24b shows an example of the residual stress profile: in analogy with the measurements onto the deep-rolled specimens, the residual stresses tend to decrease rapidly close to the surface, reaching a zero value at about 3-4 mm depth.

4.6.2 Life predictions

Crack propagation simulations were carried out considering the real geometry of the axle and extending the application of the developed algorithm. The main difference,

when considering the full-scale axle rather than the specimens, is that three contributions to the stress field coexist in the former: rotating bending, compressive residual stresses due to the deep-rolling process and positive residual stresses due to the press-fits of wheels and brake disks. All the contributions were taken into account during simulations. In particular, dedicated FE models (Figure 4.25a) were built for evaluating the stresses arising from rotating bending and press-fit, while the compressive stress field was already known from the dedicated experimental campaign described in Section 4.6.1. Only half of the axle and the wheels were modeled and structurally meshed adopting 20-node hexahedral elements with reduced integration, having global dimension 10 mm but reduced to about 1 mm along the transitions close to press-fit seats. Axle and wheels were modeled separately, and joined through a surface to surface coupling, including the interference fit option, for taking into account the stresses from press-fit. The boundary conditions were introduced by a hinge-roller at the contact points between wheels and rails. Loads were applied at the bearing journals. Results are here shown as the nodal average of the values extrapolated from Gauss quadrature points.

A fictitious crack was located at the internal T-transition of the wheels, where the maximum principal stress was found (Figure 4.25b). The in-depth longitudinal stress profile was then evaluated (Figure 4.25c) and several crack growth simulations were carried out using the same load spectrum available in the literature [14] and already adopted for testing the full-scale specimens. The block load sequence was repeatedly applied up to failure or to an equivalent service distance of 10 million kilometers. Figure 4.26 shows the obtained results for two cases: 2 mm deep semi-circular initial crack, i.e. the characteristic size of in-service ballast impacts [15], and 4 mm semi-circular initial crack, i.e. overtaking compressive residual stresses. As can be seen, deep rolling shows, again, a big retardation effect onto life propagation: an initial 2 mm deep crack does not propagate at all (Figure 4.26a) considering both ΔK-decreasing and CPLR data, while the same initial crack size could propagate to failure, considering CPLR data, within about 1 million kilometers without deep rolling. Simulations with deep rolling estimated a life of more than 1 million km even considering a 4 mm deep crack (Figure 4.26b), extending considerably the possibility to lengthen the inspection interval.

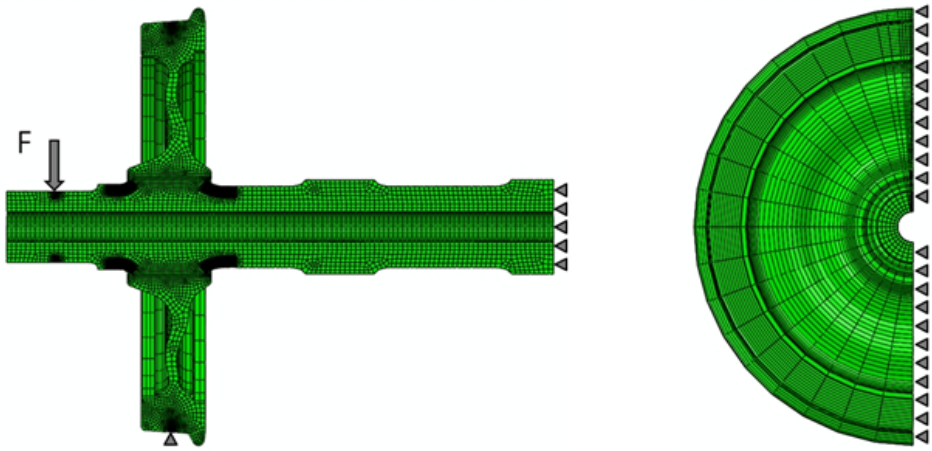

(a) Boundary conditions

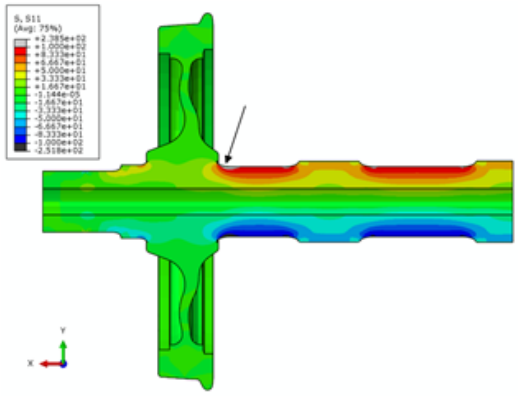

(b) Longitudinal stresses due to rotating bending

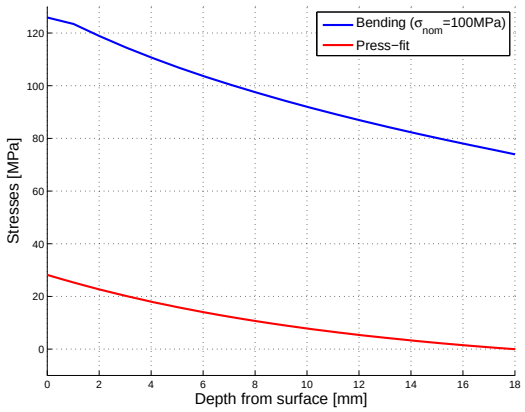

(c) Calculated in-depth stress profiles

Figure 4.25: *FE model of the full-scale axle, for the evaluation of the stress profile due to rotating bending and press-fit loading conditions*

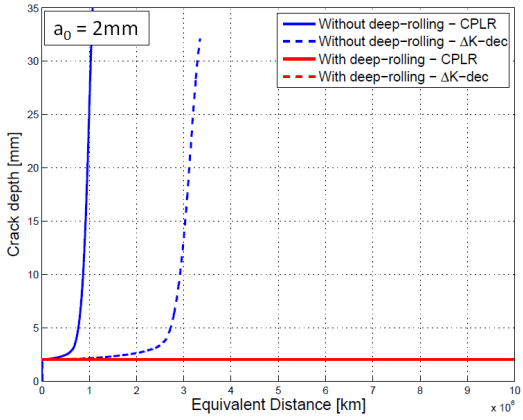

(a) Initial crack size equal to 2 mm

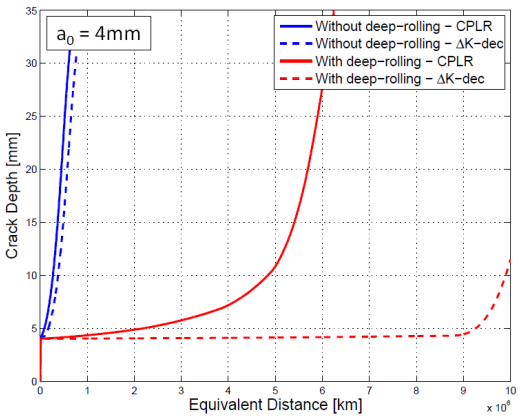

(b) Initial crack size equal to 4 mm

Figure 4.26: *Simulations of crack propagation in the full-scale railway axle considered*

4.7 Concluding remarks

The effect of the deep rolling on propagation lifetime of railway axles was investigated. The relevant results can be so summarized:

- crack growth rates of EA4T grade were experimentally measured at very negative stress ratios, finding a tendency of data to overlap and coincide with those at R=-2;
- three crack propagation tests were carried out on full-scale deep-rolled specimens. Depending on the initial notch size with respect to the depth of compressive residual stresses, no crack initiation could be observed for small flaws (R=2 mm), while unusual crack shape development happened for the largest ones (R=3 mm and R=4 mm);
- a complex surface damage pattern, characterized by crack branching and wide yielded regions, was observed around the tips of the initial notches;
- considering the case of an initial notch size comparable to the depth of the compressive residual stresses (R=3 mm), crack propagation happened for very high $\Delta \mathrm{K}_{max}/\Delta \mathrm{K}_{th}$ ratios;
- the compressive residual stress profile due to deep rolling was not modified by the application of a significant number of fatigue cycles;
- results obtained by a simple no-interaction crack propagation model, taking into account the measured stress field, were successfully compared to full-scale experimental ones;
- the application of the simple no-interaction model to the real geometry of a deep-rolled axle from industrial production, seems to allow for a significant lengthening of the inspection interval.

CHAPTER 5

Load Interaction Effects in Medium and High Strength Steels for Railway Axles

5.1 Introduction

The effect of variable amplitude loading onto crack propagation was considered in this part of the research. It is well known from the literature that an interaction effect on crack propagation arises when a specimen or a component is subjected to variable amplitude (VA) loading, like railway axles are. In dependence of the applied load sequence, a certain amount of retardation or acceleration onto fatigue crack growth rate can be observed, if compared to the constant amplitude (CA) case. In the case of structural ductile materials, this interaction phenomenon is mainly addressed by the local plasticity at the crack tip and can be explained, from a global point of view, by adopting the plasticity-induced crack closure concept [78, 107]. Since it was not feasible to perform crack propagation tests, under variable amplitude loading, only onto full-scale specimens, companion specimens SE(T), showing the same constraint effect at the crack tip as a railway axle, were adopted on the purpose. In addition, it is not possible to apply time history loading onto full-scale axles using the test bench available at PoliMi; the carried out tests onto companion specimens were intended to represent, as close as possible, the crack propagation behavior of full-scale axles at VA. Crack growth tests under variable amplitude loading were carried out onto companion SE(T) specimens made of medium (two batches of A4T material) and high strength steels (34CrNiMo6 and 30NiCrMoV12). The variable amplitude loading applied was in the shape of time history or equivalent load spectrum, with different lengths of the blocks, in order to check the retardation effect due to the load sequence adopted. Two different block's length were adopted, and two different load spectrum were used, including or not the effect of a mean stress value, simulating the effect of press-fit onto

the axle; crack propagation tests were so carried at stress ratios R=-1 and $-1 \leq R \leq 0$. Moreover, during each test, the crack closure at the crack tip was also experimentally measured. Crack growth simulations were then carried out, trying to approximate at best the experimental evidence, adopting the threshold definition from different experimental techniques, CPLR and ΔK-decreasing. Firstly, crack growth simulations were carried out by the meaning of a no-interaction model, then a simple approximation was adopted, trying to match the experimental outcomes by translating the threshold ΔK_{th}. This approximation was only intended as a first one, for basic calculations, since it cannot obviously take into account the retardation effect, which was, instead, considered adopting the more complex Strip-Yield (SY) model.

5.2 Experimental setup and methodology

The adopted specimen's geometry was a single edge-notched specimen for tensile application (SE(T)), shown in Figure 5.1, having width equal to 50 mm and thickness equal to 20 mm; the initial notch size, obtained by EDM, was 6 mm. This geometry was chosen because it is characterized by a constraint factor, at the crack tip, similar to the one shown by railway axles [90]; this permits to use these specimens as 'companion specimens' [91] of railway axles during tests in the lab.

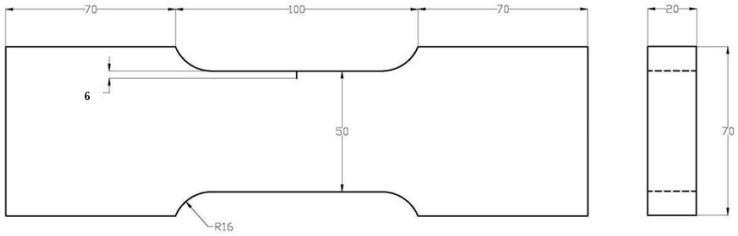

Figure 5.1: *Drawing of the adopted SE(T) specimen*

The existing notch, 6 mm in depth, was extended by sliding a razor blade into the material. Using this technique it was possible to get extremely sharp notches. The sharper the notch, the smaller the load to initiate a pre-crack at the notch root and the smaller the required length of the pre-crack to eliminate notch effects. SE(T) specimens were compression-compression fatigue pre-cracked on a Schenck Hydropuls universal testing facility equipped with a 250 kN load cell, in Figure 5.3a, available at the laboratories of PoliMi. The required load levels, obtained by trials and errors, were set to a ΔF=170 kN at R=10. Final pre-cracks lengths were documented with optical microscopy; an example is shown in Figure 5.2.

CA and VA tests were performed on the same Schenck Hydropuls universal testing facility with a capacity of 250 kN; crack length was measured in real-time with a RUMUL Fractomat control unit using a potential drop technique. For this reason, two 20 mm crack gages were glued on both sides of each specimen after pre-cracking. Crack closure calculation was performed by the meaning of a clip-on gage placed across the crack mouth, adopting the 'compliance offset' methodology described in ASTM E647 [58].

Moreover, before starting tests, 8 strain gages were glued on each specimen, as visible in Figure 5.3b, in order to verify the good alignment of the load axis; misalignment,

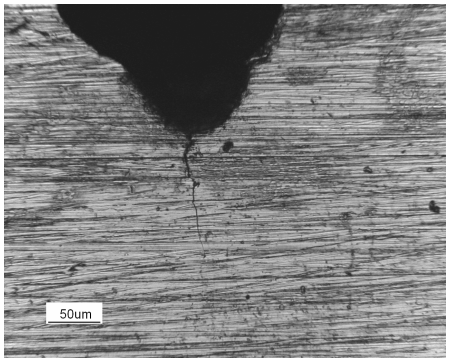

Figure 5.2: *Example of generated crack after 'razor sliding' and compression pre-cracking: final pre-crack length 0.096 mm*

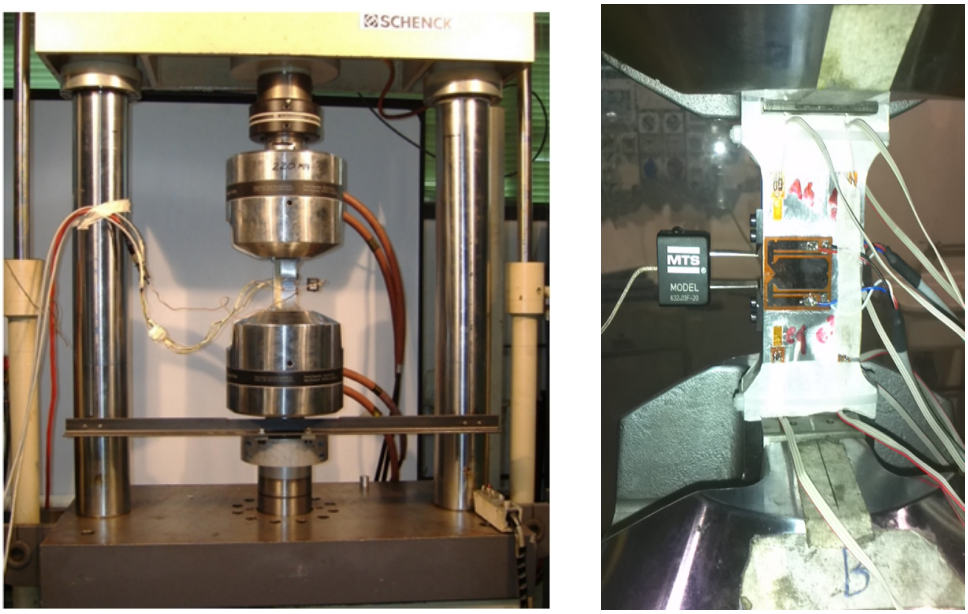

(a) Testing facility adopted

(b) Detail of the specimen with strain-gages, crack-gages and clip-on gage mounted

Figure 5.3: *Schenck Hydropuls universal testing facility equipped with a 250kN load cell*

in fact, can cause non-symmetric cracking due to bending.

Experimental crack growth data of each specimen were processed with the secant method [58], and the applied stress-intensity factor range was calculated using eq.(5.1), which was obtained from finite element analysis during previous activities [90].

$$\begin{aligned}\Delta K =&(\Delta\sigma \cdot (0.00031460192171549 \cdot a^2 + 0.00362705686515193 \cdot a + \\ &1.09184617292946) \cdot \sqrt{\pi \cdot a/1000}) \quad [\text{MPa}\sqrt{\text{m}}]\end{aligned} \tag{5.1}$$

where $\Delta\sigma$ is the applied axial stress range [MPa] and a [mm] is the measured crack length. The Finite element analysis was needed for this specimen's geometry, because the adopted SE(T) specimen, with fixed ends, is not included in the ASTM E647 stan-

dard.

5.3 Medium strength steel 1: A4T batch A

The first studied material was the commercial steel grade A4T, the medium strength steel for railway axles production included in the current regulations [1, 2]; in particular the material was given in the shape of small-scale SE(B) and SE(T) companion specimens. Eight SE(B) specimens, whose dimensions were in accordance with the standards drawings by ASTM E647 [58], were used to perform fatigue crack growth (FCG) tests at loading ratio R of 0.7, 0.1, -1 and -2, and define the corresponding thresholds and Paris diagrams. CPLR was chosen as the experimental methodology for the evaluation of the thresholds ΔK_{th}; most of the specimens were tested in the threshold region, with CPLR tests, then, if enough material was left, CPCA was also carried out, in order to define the Paris regime of the FCG curve. Specimens were pre-cracked, as already shown in chapter 4, using a MTS servo-hydraulic facility, equipped with a dedicated device for the four-point bending; stress ratio was again set to R=10, while the bending moment, for this batch of material, had to be increased, from 130 Nm, to about 160 Nm, in order to be able to obtain a pre-crack. The A4T material given for this part of the research was slightly different from the previously tested one (Chapter 4); this evidence was confirmed by hardness measurements, by which this material batch resulted harder (about 15%) than the 'Maraxil' A4T. FCG tests, after pre-cracking, were carried out onto Rumul resonant facilities, working at a frequency of about 130 Hz. Results of the carried out FCG tests are shown in Figure 5.4; results are normalized for sake of privacy; ΔK_{th} at R=-1 was chosen as reference value.

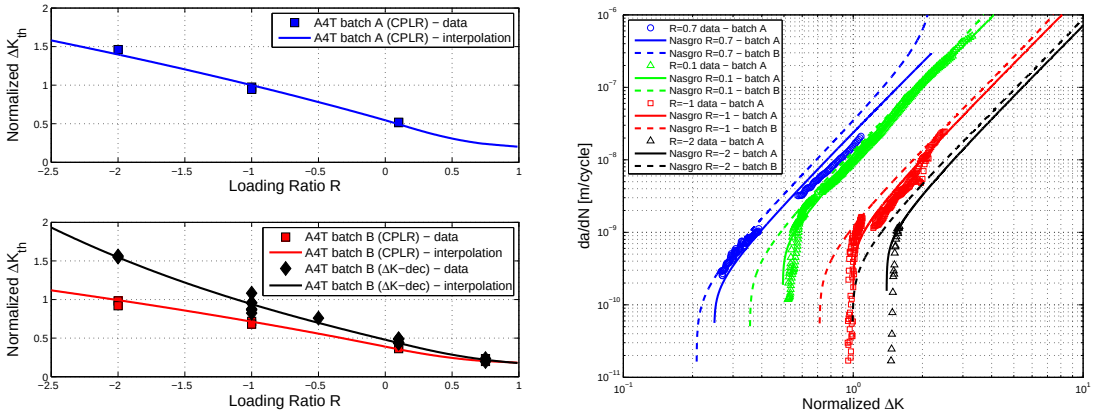

(a) Trend of normalized threshold SIF with stress ratio

(b) Normalized crack growth curves

Figure 5.4: *Normalized crack growth behavior of the considered A4T materials*

The evidence that this batch of material is slightly different from the previously tested A4T (close to A4T batch B) clearly appears from Figure 5.4a, where normalized thresholds, from both batches, are compared; as can be seen, the threshold trend line of the present grade (batch A) is higher over the whole stress ratio R range. It is worth remarking that the experimental methodology, for the threshold evaluation, was based onto compression pre-cracking for both material's batches. Apart from threshold, the

linear part of the Paris diagram (Figure 5.4) is almost identical for the two batches. The given load spectrum, for VA testing, is represented in Figure 5.5a, and it was derived from in-line measurements of a high-speed railway axle, made of A4T, traveling in Europe. The plot represents the normalized SIF amplitudes of the block load spectrum at the transition close to the wheel seat; the K_{med} value represents the SIF due to the presence of the interference fit of the wheel onto the axle. This SIF value was added to each block of the load spectrum, then the block load sequence was rearranged, obtaining the block load history shown, again normalized, in Figure 5.5b. It is worth noticing that, due to the superposition of the constant value K_{med} onto the load spectrum, the resulting stress ratio moves from the typical value R=-1 (only rotating bending), to less negative values; the acting stress ratios are between zero and minus one. Since aim of this part of the research was to understand the effect of the block length onto crack propagation and retardation, two different block's length were adopted: the 'longer' one, composed of about 5 million cycles, represented in Figure 5.5, and a 'shorter' one, obtained dividing the blocks by seven; the experimental plan is shown in Table 5.1: specimen A4T SE(T)1 was tested applying the longer blocks, while specimen A4T SE(T)2 was tested against the shorter ones.

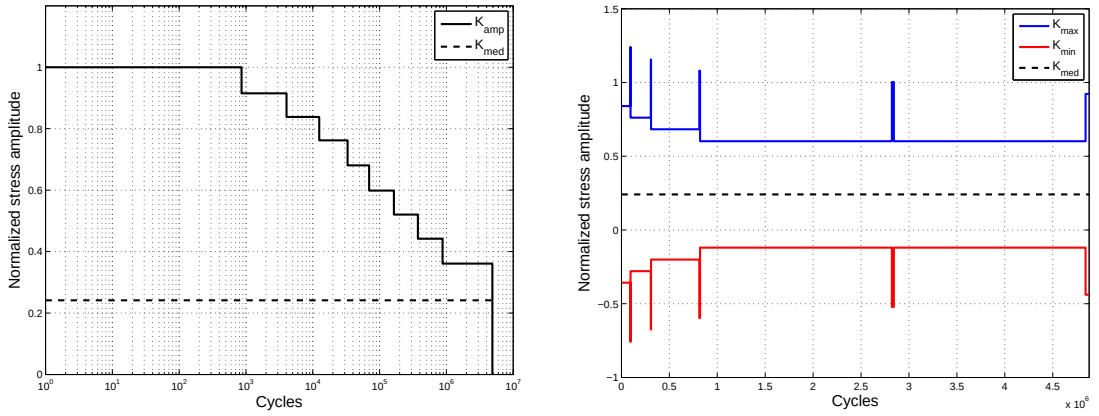

(a) Load spectrum

(b) Applied block load sequence, derived from the load spectrum in (a)

Figure 5.5: *Normalized VA loadings, in the shape of load spectrum and block loading sequence derived from real service; stress ratio* $-1 < R < 0$

Specimen	Type of test
A4T SE(T)1	Variable amplitude loading – Longer blocks
A4T SE(T)2	Variable amplitude loading – Blocks length divided by 7

Table 5.1: *Batch A – A4T SE(T) specimens – performed tests*

The amplification of the block load sequence, equal for both specimens, was chosen in order to generate, at the crack tip of the SE(T) specimens, the same stress intensity as a 2 mm depth crack present in the wheelset. Results of crack propagation onto the two tested specimens are shown in Figure 5.6; as can be seen, both experiments lasted around 25 million cycles, and crack propagation of the two tests match very well

between themselves; there is no additional retardation effect due to the length of the blocks for the considered material.

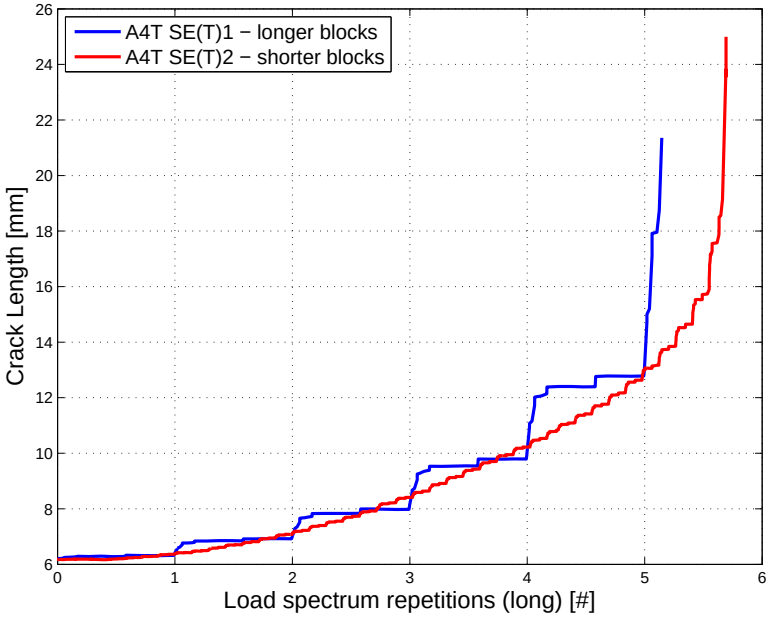

Figure 5.6: *Comparison between long and short blocks*

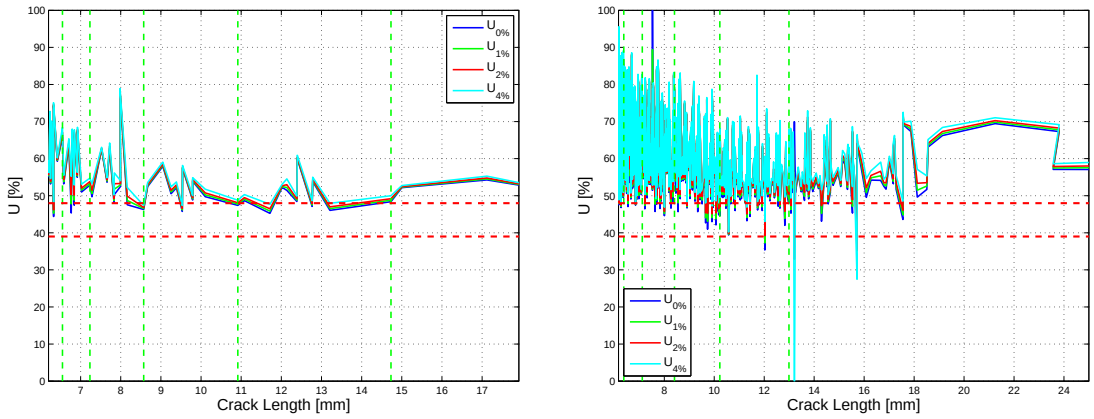

(a) Specimen A4T SE(T)1 (b) Specimen A4T SE(T)2

Figure 5.7: *Measured crack closure U for the two A4T tested specimens*

The crack closure level, as recorded during the two tests, is shown in Figure 5.7; as can be seen, the closure level is higher than expected; the two red dotted lines, representing the extremes value, as for the Schijve formulation, at the involved stress ratios, are lower than the experimental outcomes for both tests, which, anyway, showed comparable trends also for the closure U value. This behavior appears to be due to the fact that at lower stress amplitudes (when crack advance is negligible) the S_{op} values remain 'frozen' at values of the higher stress amplitudes, where a sudden crack advance happen, causing a 'large opening' of the crack tip. This closure level should indicate

a faster crack growth, while, in reality, the crack does not propagate at all during the lower load blocks, because of the crack tip plasticity induced by the high levels.

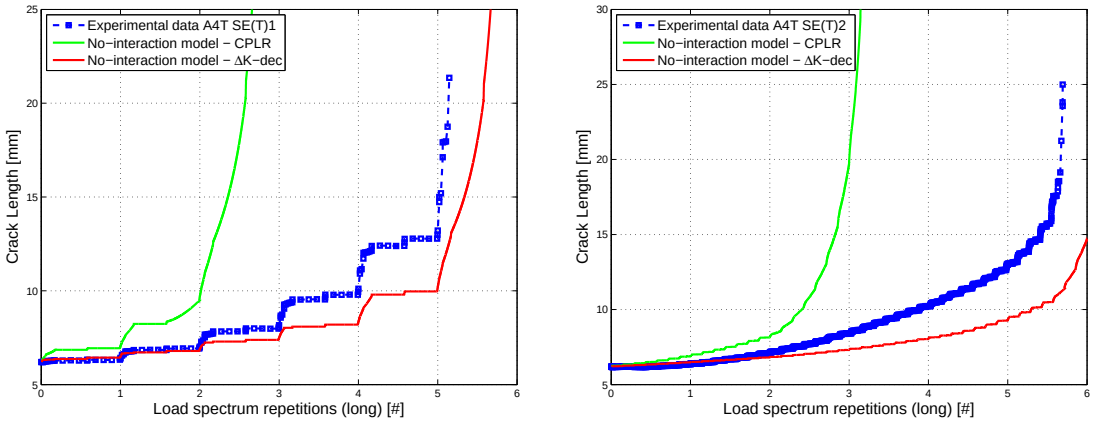

(a) Specimen A4T SE(T)1 (b) Specimen A4T SE(T)2

Figure 5.8: *Crack growth simulations adopting a simple no-interaction model*

Crack growth predictions, adopting a simple no-interaction model, were carried out; the crack propagation algorithm was based on the Nasgro equations, tuned with the parameters derived from the small-scale experimental campaign onto SE(B) specimens, and on the SIF definition, for SE(T) specimens, of eq.(5.1). Both the threshold's trends, from present experimental campaign, based onto CPLR testing methodology (Figure 5.4a), and from previous experimental testing, based onto ΔK-decreasing [102], were adopted for the simulations, and compared. Results are shown in Figure 5.8; as can be seen, both experiments stay in between the carried out predictions adopting thresholds from the two adopted techniques. CPLR and ΔK-decreasing can so be regarded as lower and upper bound, respectively, of the experimental outcomes, at least for this material.

5.4 High strength steel 1: 34CrNiMo6

The second tested material was the steel grade 34CrNiMo6, a high strength steel for railway application adopted in the german ICE trains, not included in the current regulations. This material exhibits a yielding stress around 730 MPa and an ultimate stress close to 1000 MPa. Material, in the shape of SE(B) specimens, was firstly tested to crack propagation at CA, in order to derive FCG curves and thresholds. Both experimental approaches, CPLR and ΔK-decreasing, were adopted for the threshold determination. Results of the FCG tests carried out are shown, again normalized for sake of privacy, in Figure 5.9; the reference point chosen for normalization was the threshold, from CPLR, at the stress ratio R=-1.

As can be seen from Figure 5.9a, this material does not show any remarkable difference in thresholds due to the experimental methodology adopted, as was for the A4T medium strength steel. A peculiarity of this material clearly appears looking at the plot of Figure 5.9b, where FCG rates, at stress ratios R=0.7 (effective curve) and R=-1 are compared. As can be seen, the two data sets, at different stress ratios, have a different

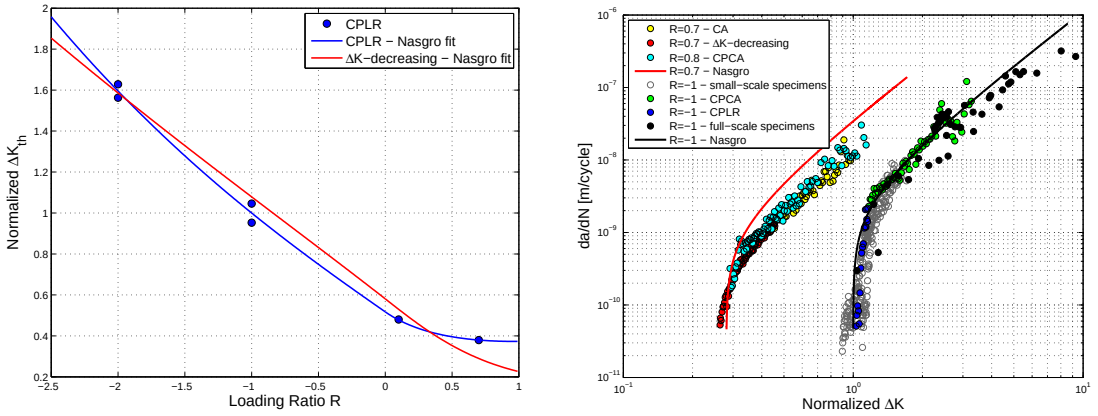

(a) Trend of normalized threshold SIF with stress ratio

(b) Normalized crack growth curves

Figure 5.9: *Normalized crack growth behavior of the considered 30NiCrMoV12 material*

shape, which cannot be captured by Nasgro's interpolations, represented by continuous lines in the plot. In order to clarify the differences, a crack closure evaluation was carried out onto these curves, starting from the 'effective' one, as in Figure 5.10. It was found that the FCG curve at R=-1 cannot be obtained from a rigid translation of the 'effective' curve, because the U value is not constant at about 0.34 as expected by Schijve equation, but increases up to 0.5 in the upper region, at da/dN values higher than about $3 \cdot 10^{-9}$. Anyway, the lower region is well represented by a 'standard' closure phenomenon, with a closure value $0.27 \leq U \leq 0.34$, as expected.

Table 5.2 summarizes the crack propagation tests, under VA loading, carried out onto the considered 34CrNiMo6 high strength steel (here shortened as 'HSS1'). The focus is here again pointed onto the effect of block's length upon crack growth rate and retardation. The applied load spectrum was the same one of Figure 5.5, already adopted for the two tests onto the A4T material; the two experiments onto 34CrNiMo6 material represent the same conditions as for the A4T material: specimen HSS1-SE(T)1 was tested against 'long blocks', as in Figure 5.5b, while HSS1-SE(T)2 was tested against 'short blocks', i.e. block's length divided by seven. The magnification of the load spectrum was again chosen in order to represent, onto the specimens, the same SIF as a 2 mm circular crack inserted in an existing axle.

Specimen	Type of test
HSS1-SE(T)1	Variable amplitude loading – Longer blocks
HSS1-SE(T)2	Variable amplitude loading – Blocks length divided by 7

Table 5.2: *34CrNiMo6 SE(T) specimens – performed tests*

Results of the two carried out crack propagation tests are shown in Figure 5.11. As can be seen, this material, contrarily to the tested A4T material, exhibits an effect of retardation due to block's length: the experiment with shortened blocks lasted longer than the other one. It is worth remarking, here, that the ΔK values of the two tests were quite high, leading specimen HSS1-SE(T)1 to failure in less than three repetitions of the load spectrum. Measurements of crack closure during the two experiments,

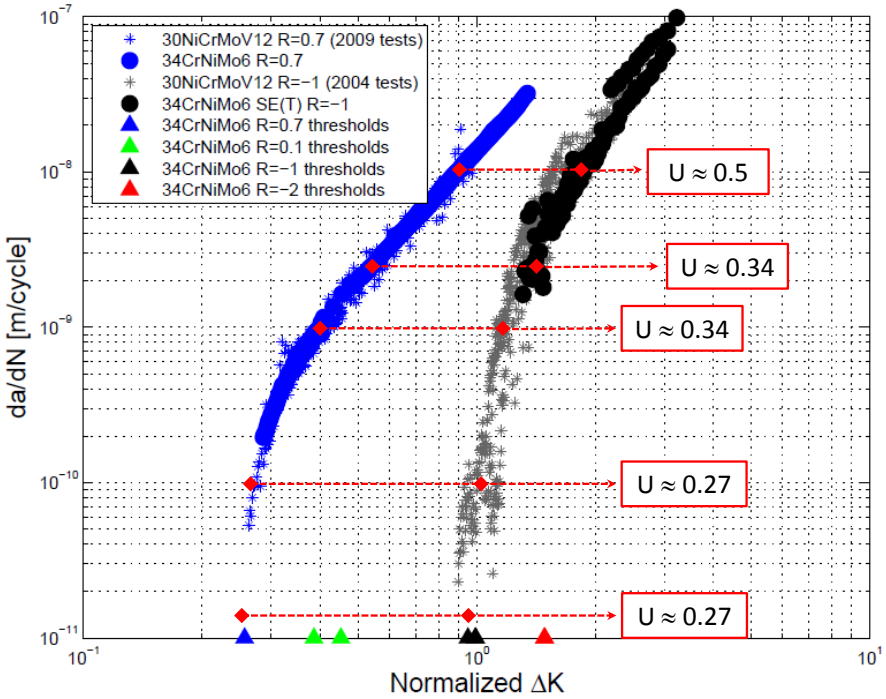

Figure 5.10: *Closure evaluations at different da/dN values, between the 'effective' FCG and the R=-1 stress ratio one*

in Figure 5.12, look similar; there is no difference in measured crack closure level which can explain the experimental evidence of one crack retarding more than the other one. Again, the crack closure measurements are higher, during the whole tests, than expected adopting the Schijve formulation, represented by red dotted lines in the two plots of Figure 5.12. The evidence that crack closure remains 'frozen' at the level reached during the higher stress blocks is reinforced looking at Figure 5.12b, relative to the test with shorter blocks; it is here clearly visible that the closure level increase at the beginning of each short spectrum, where the stresses are higher. Moreover, the sequence repetition is evident.

Crack growth simulations carried out, with the simple no-interaction model, are shown in Figure 5.13. Since, for this material, there is almost no difference in the threshold trend line, only CPLR thresholds were taken into account for the simulations. As can be seen, crack growth simulations show a large amount of conservativism in comparison to the experimental outcomes.

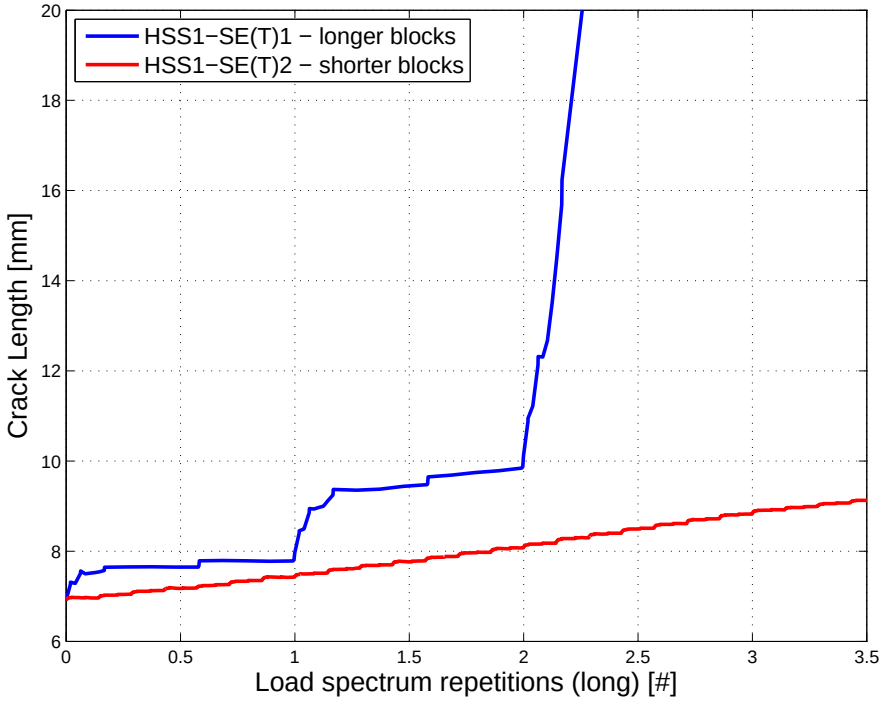

Figure 5.11: *Comparison between time history and block loading*

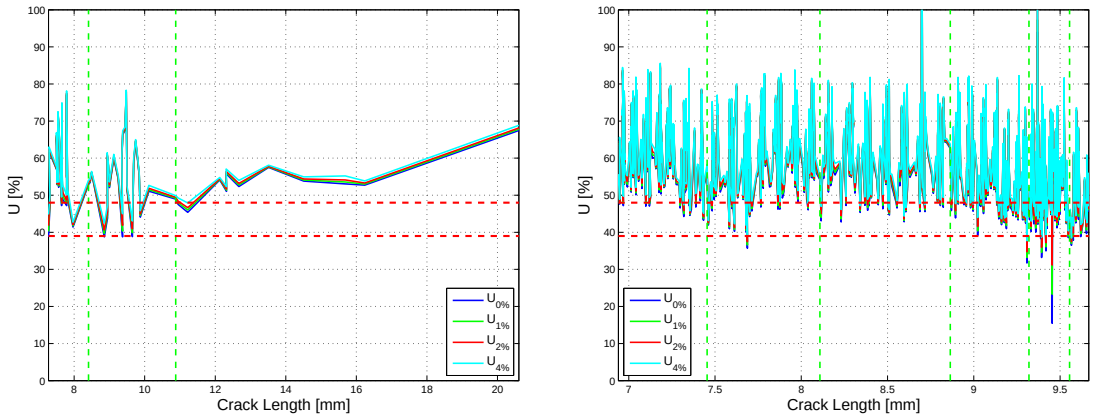

(a) Specimen HSS1-SE(T)1

(b) Specimen HSS1-SE(T)2

Figure 5.12: *Measured crack closure U for the two 34CrNiMo6 tested specimens*

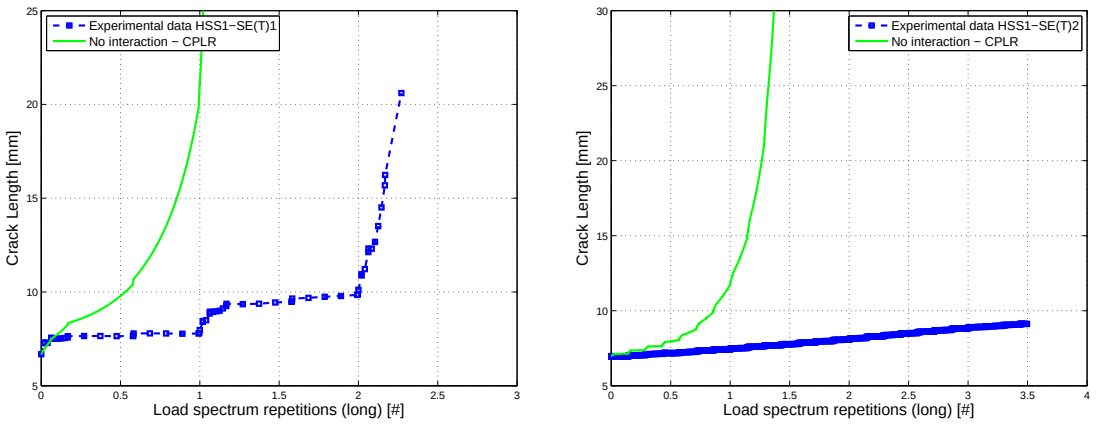

(a) Specimen HSS1-SE(T)1

(b) Specimen HSS1-SE(T)2

Figure 5.13: *Crack growth simulations adopting the simple no-interaction model*

5.5 High strength steel 2: 30NiCrMoV12

The same approach already adopted for A4T material, in section 5.3 and high strength steel 34CrNiMo6, in section 5.4, was extended to other materials tested during previous experimental campaign: firstly, experiments onto high strength steel 30NiCrMoV12, then onto a different batch of A4T material were re-analyzed based on the defined methodology. Regarding 30NiCrMoV12 high strength steel, the behavior to crack propagation was found to be indistinguishable from the similar 34CrNiMo6 already tested, as can be observed from the detail of Figure 5.10, which included experiments from both high strength steel grades. Flow stress and ultimate stress were found to be similar too, having values close to 730 MPa and 1000 MPa respectively. Given these presuppositions, the behavior to VA loading was expected to be similar to the already tested 34CrNiMo6 steel grade. Figure 5.14 shows the VA loading shapes considered: a first specimen was tested against time history loading, as in Figure 5.14a, while a second one was tested against load spectrum, in Figure 5.14b, derived from the same time history loading; the carried out tests are shown in Table 5.3. The approach was similar to the already tested materials; the main difference here, was that the stress ratio was constant and equal to minus one: no effect of the mean stress, from press-fit loading condition, was here considered. Again, VA loading is shown as normalized for privacy reasons.

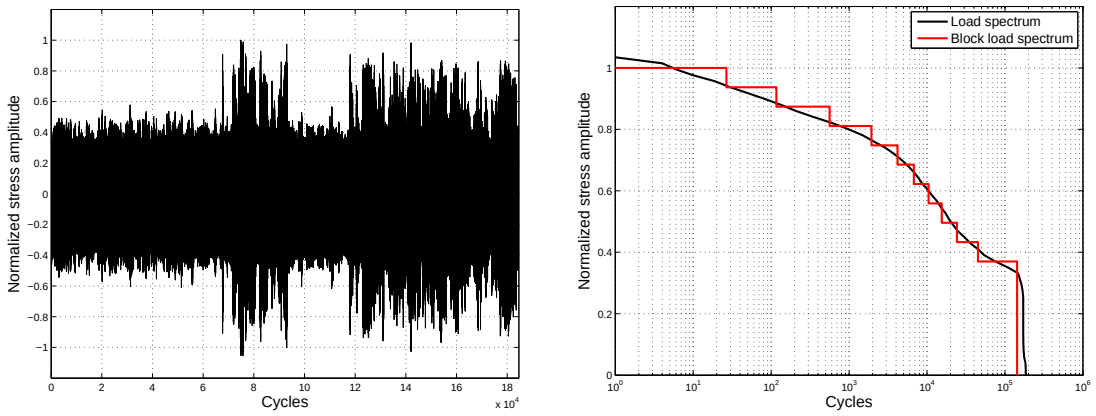

(a) Time history loading

(b) Loading spectrum derived from the time history in (a)

Figure 5.14: *Normalized VA loadings, in the shape of time histories or equivalent block loading sequence derived from real service; stress ratio* $R = -1$

Specimen	Type of test
HSS2-SE(T)1	Variable amplitude loading – Time History
HSS2-SE(T)2	Variable amplitude loading – Equivalent Load Spectrum

Table 5.3: *30NiCrMoV12 SE(T) specimens – performed tests*

Comparison of the resulting crack growth advances, for the two specimens tested against time history and equivalent load spectrum is shown in Figure 5.15. As can be seen, the two experimental outcomes match very well, at a global level, even if, block

by block, the crack advance is different. Contrary to the already shown 34CrNiMo6 steel grade, the two specimens made of 30NiCrMoV12 were tested at lower ΔK values; crack advance, at the end of the tests, was around 3 mm for the two experiments.

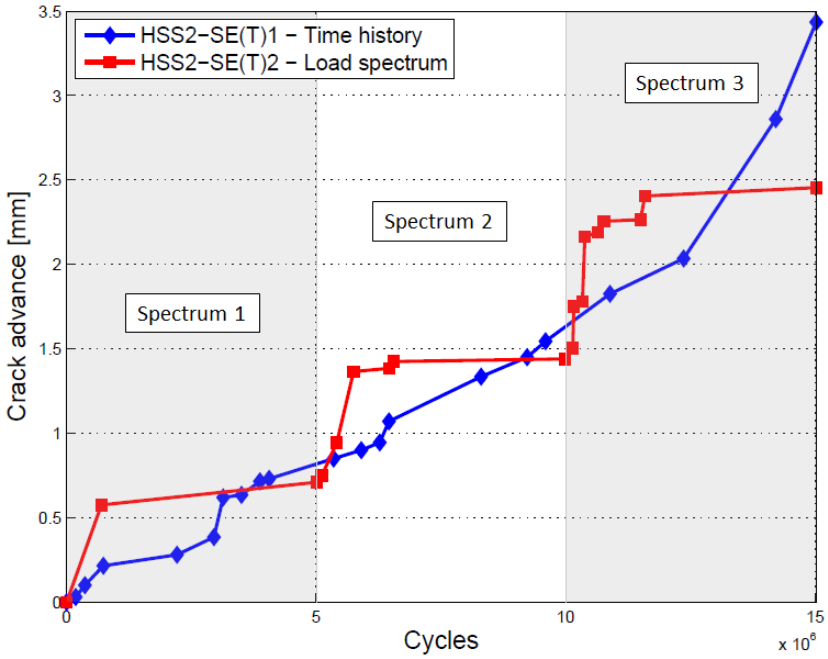

Figure 5.15: *Comparison of crack growth between two specimens, made of 30NiCrMoV12, tested applying Time History or Load Spectrum of Figure 5.14*

Regarding the measured crack closure, in Figure 5.16 the trend is similar to the other tested materials, with measured U values higher than the value expected, by Schijve equation, at constant amplitude loading. Again, this behavior can be explained considering that crack closure, at lower ΔK values, cannot stabilize, since the crack cannot advance, and remains 'frozen' at high values.

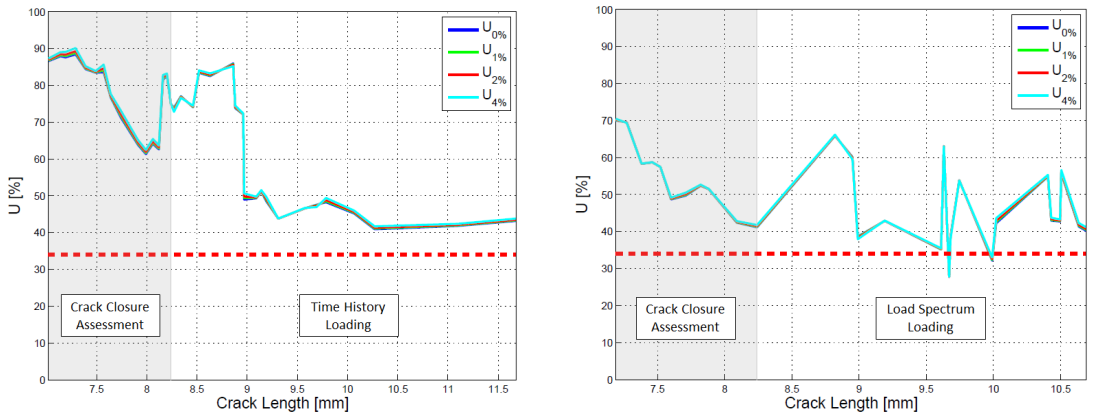

(a) Specimen HSS2-SE(T)1

(b) Specimen HSS2-SE(T)2

Figure 5.16: *Measured crack closure U for the two 30NiCrMoV12 tested specimens*

Crack growth simulations, considering again only the CPLR trend of the thresholds, since the material behavior is the same of the 34CrNiMo6, showing almost no difference in the threshold trends between the two methodologies, is shown in Figure 5.17. As can be seen, a large amount of conservatism appears from the carried out simulations.

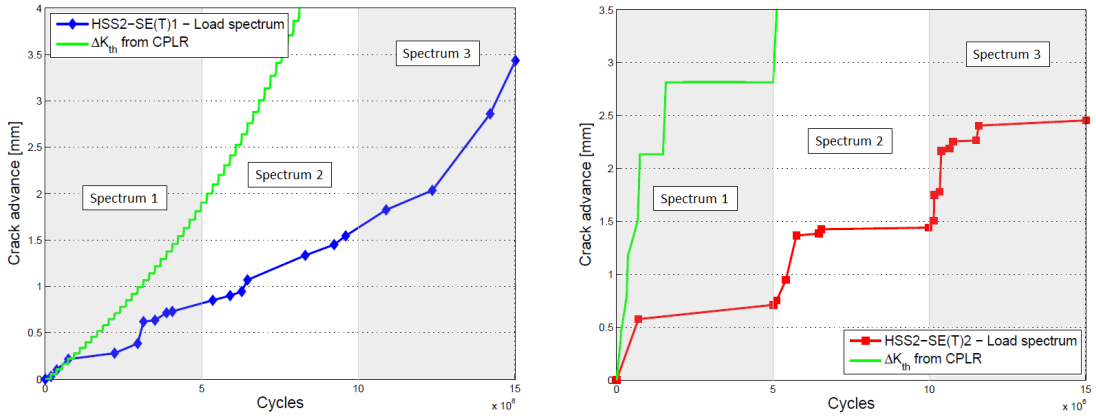

(a) Specimen HSS2-SE(T)1

(b) Specimen HSS2-SE(T)2

Figure 5.17: *Crack growth simulations adopting the simple no-interaction model*

5.6 Medium strength steel 2: A4T batch B

Finally, a second batch of A4T medium strength steel, marked as 'batch B', was re-analyzed from previous testing. The considered experiments, shown in Table 5.4, include two companion SE(T) specimens, tested against time history and equivalent load spectrum, and a full-scale specimen (Figure 5.18), tested against load spectrum onto the test bench, applying rotating bending, available at PoliMi laboratories. The FCG diagram, regarding both thresholds and linear region of the Paris diagram, was found to be very close to the experimental evidence found for the 'Maraxil' A4T material, already shown in chapter 4; as parameters of the Nasgro equation, the 'Maraxil' set was adopted.

Specimen	Type of test
A4T2-SE(T)4	Variable amplitude loading – Time History
A4T2-SE(T)5	Variable amplitude loading – Equivalent Load Spectrum
Full-scale axle	Variable amplitude loading – Equivalent Load Spectrum

Table 5.4: *A4T batch B specimens – performed tests*

The adopted VA loading was the same already taken into account for the high strength steel 30NiCrMoV12, shown in Figure 5.14. Amplification of the loading spectra was set in order to reach a SIF level, at the crack tip, equivalent to the one registered by a 2 mm deep crack inserted in a real full-scale axle. Figure 5.19 directly compares the crack advance registered during the two tests onto SE(T) specimens. As can be seen, they seem comparable, at least over the initial propagation of the crack.

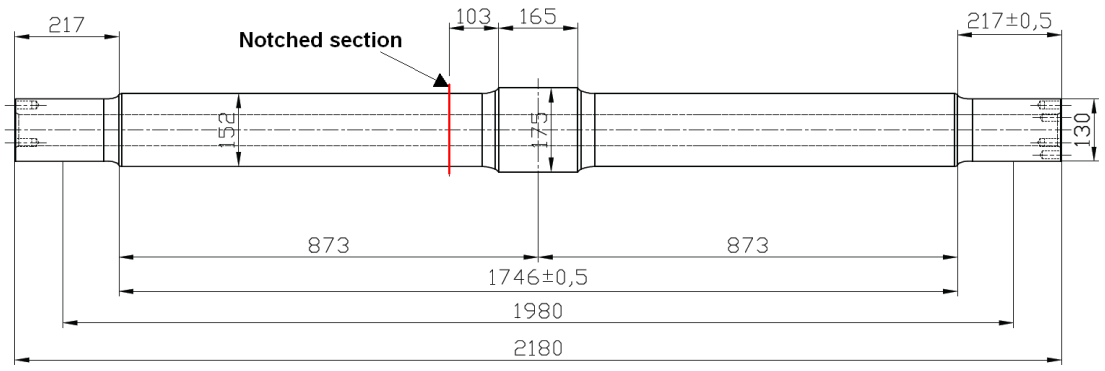

Figure 5.18: *Full-scale specimen, made of A4T batch B, tested against load spectrum*

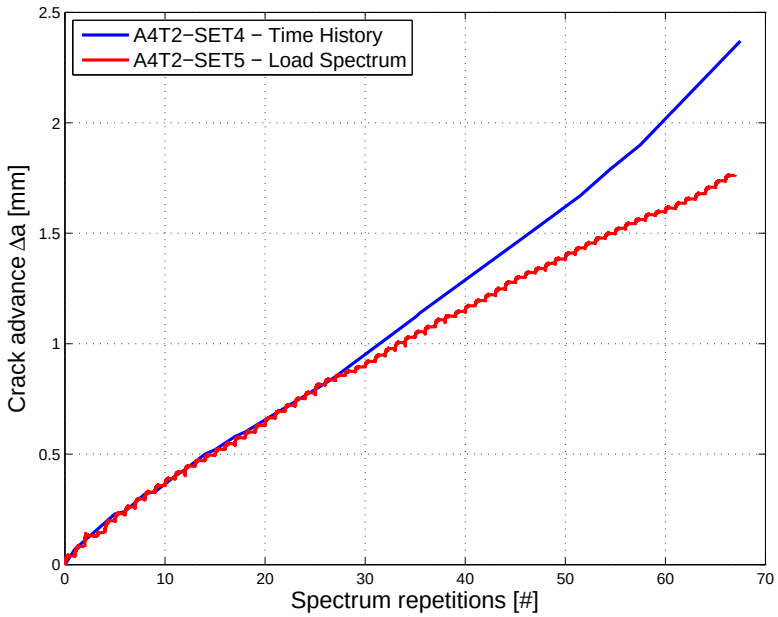

Figure 5.19: *Comparison between time history and block loading*

The trend of the measured crack closure U levels, for the two tested SE(T) specimens is shown in Figure 5.20. The experimental $U = \Delta K_{eff}/\Delta K$ value, during the effective VA loading test, resulted to be about 0.35 for both tests, in accordance with the indications given by the Schijve equation at R=-1.

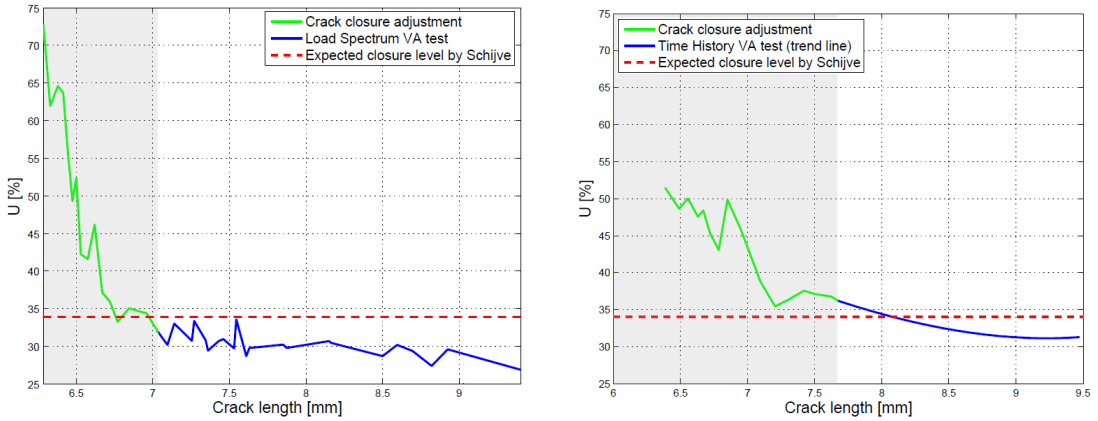

(a) Specimen A4T-SE(T)4 - Time History

(b) Specimen A4T-SE(T)5 - Load spectrum

Figure 5.20: *Measured crack closure U for the two tested specimens made of A4T 'batch B'*

Crack growth simulations, adopting both CPLR and ΔK-decreasing thresholds, are shown in Figure 5.21; it was decided to start the simulations only at spectrum number eight, since the two experimental curves show a descendant behavior, meaning that the crack closure was not sufficiently stabilized. By the carried out simulations, it appears that the experimental outcomes are included between the two simulations adopting CPLR or ΔK-decreasing, as it was for A4T batch A steel grade.

Regarding the crack propagation test onto the full-scale specimen, in Figure 5.18, two artificial notches were machined by electrodischarging method (EDM) in the indicated section, at 180° from each other, in order not to interfere during propagation; the two notches were machined as semi-elliptical, having depth $a_0 = 1.5$mm and shape $a/c = 0.67$. The full-scale specimen was subjected firstly to 10 repetitions of the load spectrum, in order to nucleate a sharp crack out of the artificial notches, than to other 90 repetitions, and finally to other 77 repetitions of the load spectrum increased by 25%, since almost no crack growth occurred during the previous phase. Results of the carried out test onto the full-scale axle are shown in Figure 5.22.

No crack closure was measured during the test on the full-scale specimens. From Figure 5.22 it appears evident, anyway, that about 15 repetitions of the load spectrum were needed to stabilize crack closure; the behavior of crack propagation, during the first 15 spectrum, is slowing, and moves upward during the remaining part of the test. Because of this behavior, crack growth simulations, shown in Figure 5.23, were carried out starting from spectrum 16. As for the companion SE(T) specimens, the experimental evidence stays between the two predictions with thresholds from CPLR and ΔK-decreasing, confirming the trend for this material and the validity of SE(T) specimens as 'companion' of full-scale axles.

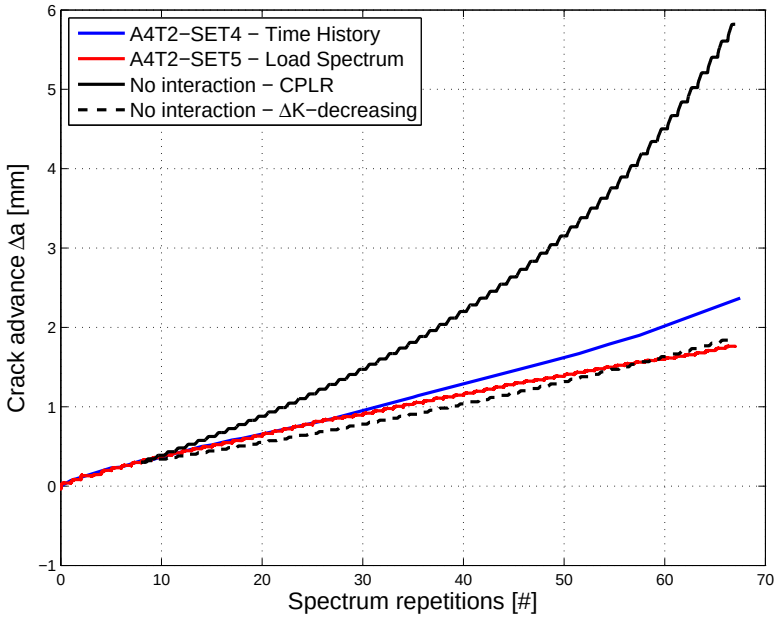

Figure 5.21: *Crack growth predictions adopting thresholds from both CPLR and ΔK-decreasing experimental methodologies*

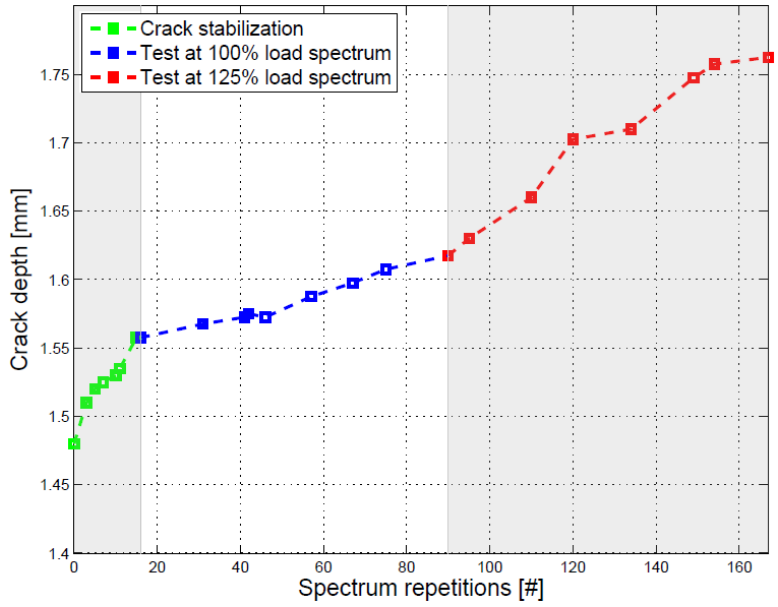

Figure 5.22: *Results of the crack propagation test onto the full-scale specimen made of A4T 'lotto B'*

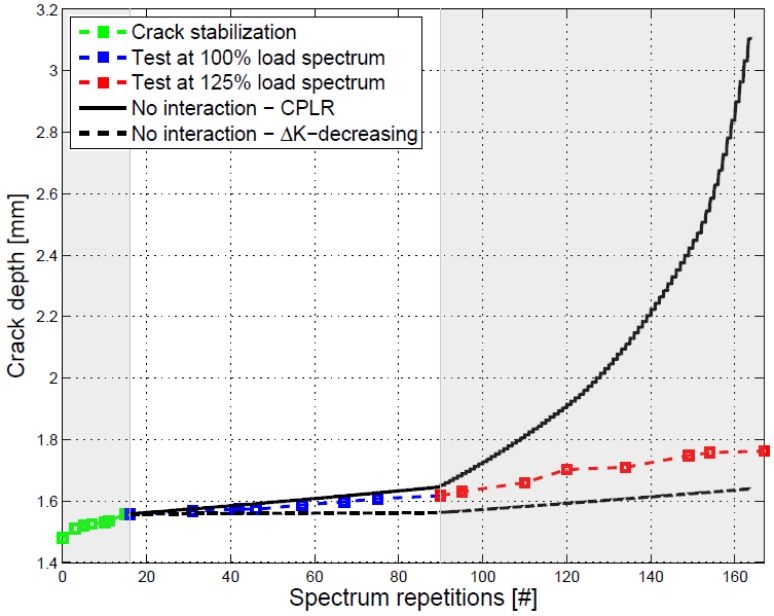

Figure 5.23: *Crack growth predictions, adopting thresholds from the two experimental methodologies, compared to the measurements*

5.7 Crack growth simulations adopting the Strip-Yield model

More sophisticated crack growth simulations were carried out by the meaning of the Strip-Yield model, as implemented in the commercial software Nasgro [80], which is able to take into account for interaction effects, during propagation, due to crack tip plasticity and developing of the crack closure. The threshold trend from CPLR experimental methodology was adopted, and the software required the experimental points of the effective crack growth curve as input; the Strip-Yield method is, in fact, based upon crack closure evaluation and calculations of the crack growth rates are carried out onto the curve at stress ratio R=0.7, conventionally adopted as the 'closure free' curve.

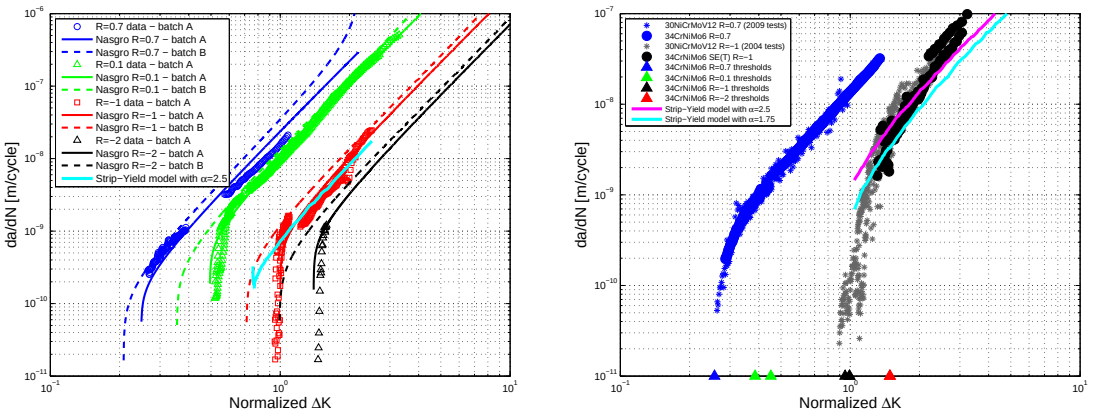

(a) A4T steel batches

(b) High strength steel batches

Figure 5.24: *Analysis at constant amplitude loading, at R=-1, adopting the Strip-Yield model*

The parameter α can affect crack propagation in a large way: according to the Nasgro manual [80] it should be fixed at 2.5 for common steel grades, while literature [90] suggests a value of α close to 3 for the modified SE(T) specimens made of A1N. A first analysis was carried out, trying to reproduce the crack growth curves at the stress ratio R=-1 by the meaning of the Strip-Yield model. The value $\alpha = 2.5$, suggested by the Nasgro manual, was adopted for these analysis, in order to understand its adequacy. Results of such analyses are reported, for both medium and high strength steels, in Figure 5.24. As can be seen, the value $\alpha = 2.5$ is adequate for the A4T medium strength steel batches, while no univoque α value is able to describe the whole crack growth curve at R=-1, regarding the high strength steel grades. This is due to the already discussed (Figure 5.10) behavior of the high strength steels tested, at CA loading, at low or high stress levels; these materials, in fact, show a non-constant closure level, so the crack growth curve at R=-1 cannot be described by rigid translation of the effective curve. An α value close to 2.5 seems to be adequate to describe the linear part of the Paris diagram (higher ΔK), while an α value close to 1.75, as in Figure 5.24b, seems to represent in a better way the near-threshold region (lower ΔK).

Considering A4T batch A, the lifetime predictions, for both the tested specimens, in Figure 5.25, are close to the experiments, thus remaining on the safe side. The simulation by the Strip-Yield model are closer to the experimental evidence than the simpler no-interaction model, and the retardation effect is well represented.

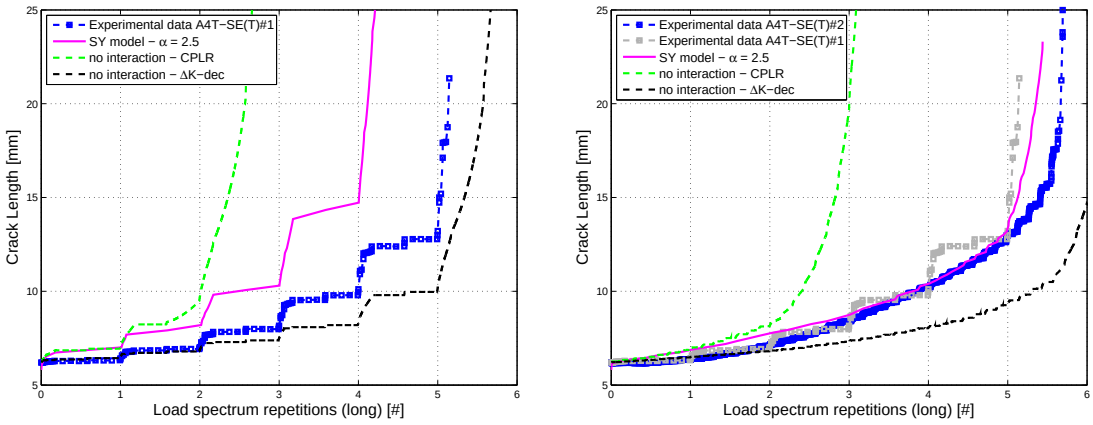

(a) Specimen A4T SE(T)#1

(b) Specimen A4T SE(T)#2

Figure 5.25: *Comparisons of crack growth simulations, onto the A4T batch A steel grade, adopting the Strip-Yield model against the simple no-interaction one*

Regarding 34CrNiMo6 high strength steel grade, crack growth predictions, by Strip-Yield model, were also carried out, shown in Figure 5.26. As can be seen, in this case the model is close to the experiment, with an $\alpha = 2.5$ parameter, regarding specimen HSS1-SE(T)#1, tested with longer blocks, but cannot represent the evidence when considering specimen HSS1-SE(T)#2, tested against shorter blocks and showing a large amount of retardation.

Figure 5.27 is relative to the Strip-Yield calculations carried out onto the second high strength steel tested, the 30NiCrMoV12 grade. In this case, since the applied ΔK were low, close to the near-threshold region, the α parameter was set to 1.75,

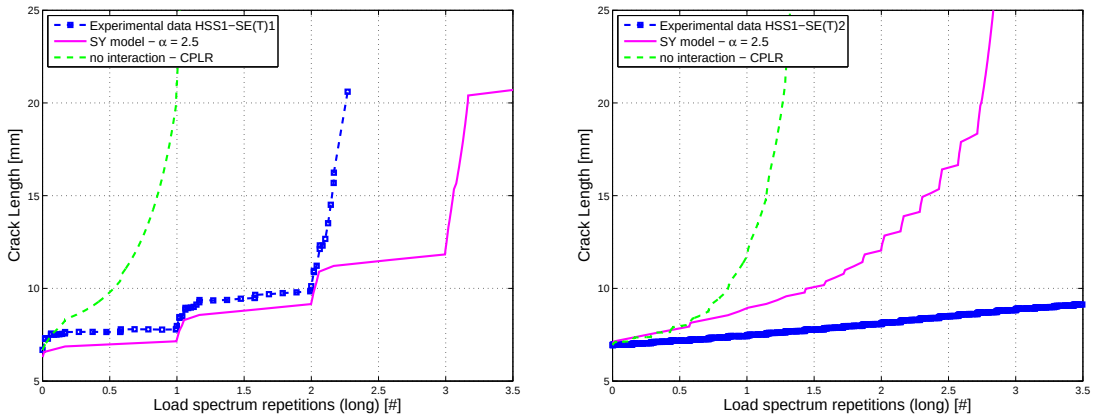

(a) Specimen HSS1-SE(T)#1 (b) Specimen HSS1-SE(T)#2

Figure 5.26: *Comparisons of crack growth simulations, onto 34CrNiMo6 steel grade, adopting the Strip-Yield model against the simple no-interaction one*

which results in a better description of the lower region of the crack growth curve at R=-1, as shown in Figure 5.24. As can be seen, specimen HSS2-SE(T)1, tested against time history loading, is well represented by the Strip-Yield model calibrated with $\alpha = 1.75$. Regarding specimen HSS2-SE(T)2, tested against block loads, the simulation is too much conservative. Even if the two specimens show comparable crack propagation trends at a global level, as visible in Figure 5.27, the sequence of loads is different, requiring a different SY modellization; regarding the second specimen, a very low α value is required to force the crack to stop during the long blocks at low stress amplitude. It's worth noticing, anyway, that these values of the α parameter are quite uncommon, and outside the typical range [90].

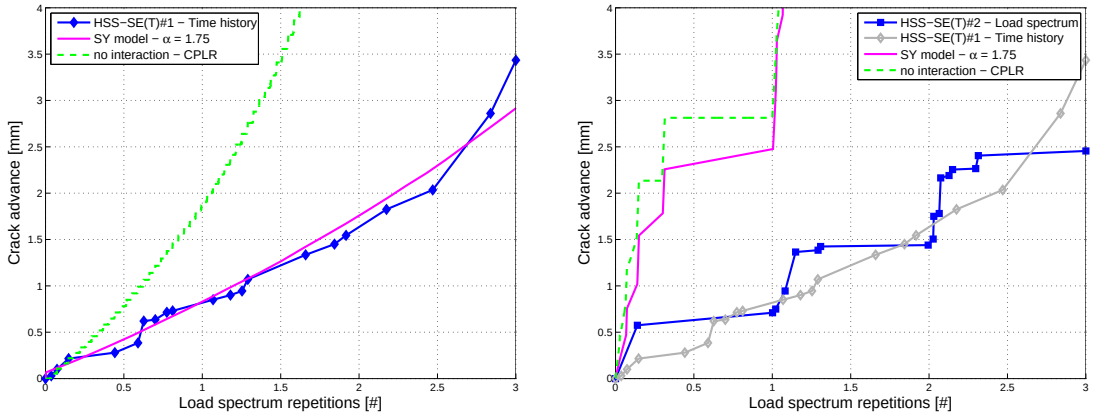

(a) Specimen HSS2-SE(T)#1 (b) Specimen HSS2-SE(T)#2

Figure 5.27: *Comparisons of crack growth simulations, onto 30NiCrMoV12 steel grade, adopting the Strip-Yield model against the simple no-interaction one*

Concluding with the high strength steels, it's worth remarking that, as already shown in Figure 5.10, the crack growth curves at stress ratios different than 0.7 cannot be

obtained from rigid translation of the effective curve, due to the intrinsic behavior of the two high strength steel grades tested; the Strip-Yield model, only based onto the effective curve, is maybe too much affected from this behavior. The chosen approach, dividing the crack growth curve in the near-threshold and Paris regimes, is a good approximation, but too simplistic for real application cases.

Coming back to the second A4T tested batch, the Strip-Yield model was adopted also for the predictions of the two SE(T) specimens, shown in Figure 5.28, returning, again, in accurate predictions when adopting the parameter $\alpha = 2.5$, well describing the crack growth curve, at R=-1, under constant amplitude loading.

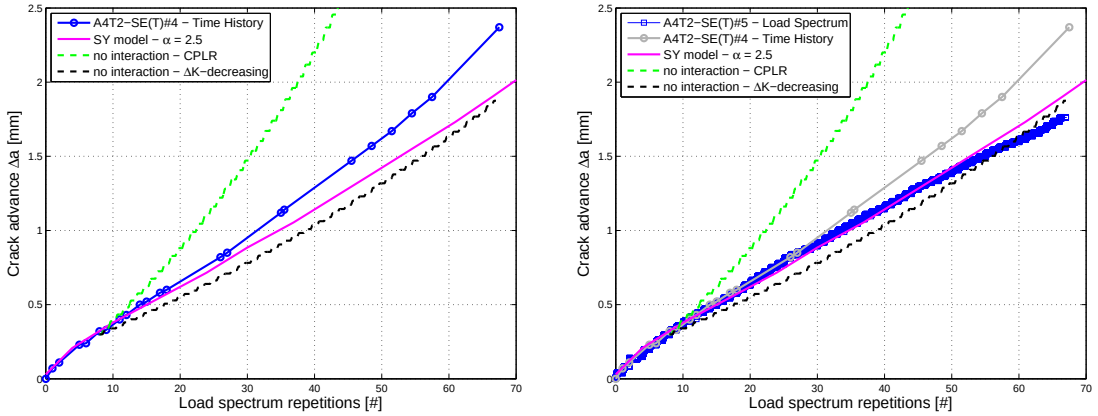

(a) Specimen A4T2-SE(T)#4 (b) Specimen A4T2-SE(T)#5

Figure 5.28: *Comparisons of crack growth simulations, onto A4T batch B steel grade, adopting the Strip-Yield model against the simple no-interaction one*

Considering the whole A4T tested, from the two batches, a similar amount of retardation seems to arise from all the tests carried out under VA loading; the α value suggested by the Nasgro manual coincided with the one evaluated by considerations on the crack growth curves at R=-1 under constant amplitude loading. The crack growth simulations under variable amplitude loading were in good accordance with the experimental outcomes, thus remaining on the safe side.

Considering the two high strength steel grades tested, instead, the experiments present a higher dispersion and cannot be represented by a univoque value of the α parameter, as was for the A4T steel grade. A value $\alpha = 2.5$ can be assumed in the case of high ΔK and long blocks (specimen HSS1-SE(T)1), when only a small amount of retardation arises, while values of $\alpha = 1.75$ should be adopted for tests at low ΔK values, close to the near-threshold region. These indications, anyway, were not accurate for all the tested specimens.

5.8 Crack growth simulations adopting a simple threshold translation

A simpler attempt to match lifetime predictions to the experiments, which has no physical meaning, out of the statistical dispersion of the thresholds, consisted in trying to move the threshold trend line till the predictions were close to the experiments; since ΔK-decreasing, when resulting in thresholds higher than those obtained by CPLR, led

to non-conservative predictions, it was chosen to move upward the CPLR threshold trend, as in Figure 5.29. An equivalent result could be obtained by reducing the thresholds from ΔK-decreasing methodology, but the upward translation of the thresholds from CPLR was preferred because it highlights the retardation effect of the material, according to the physical effect.

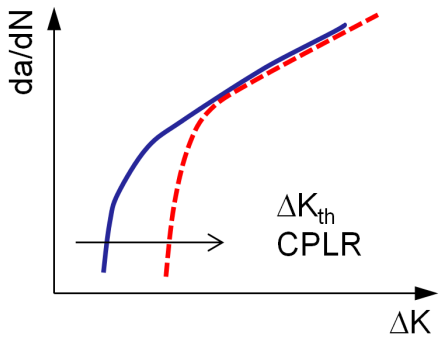

Figure 5.29: *CPLR threshold translation*

Regarding A4T batch A, the predictions with threshold translation are shown in Figure 5.30. As can be seen, while CPLR is too conservative and ΔK-decreasing is not, the best matching, for both experiments, was found moving the CPLR thresholds by 12%; by this correction the predictions better agree with the experimental evidence, thus remaining on the safe side.

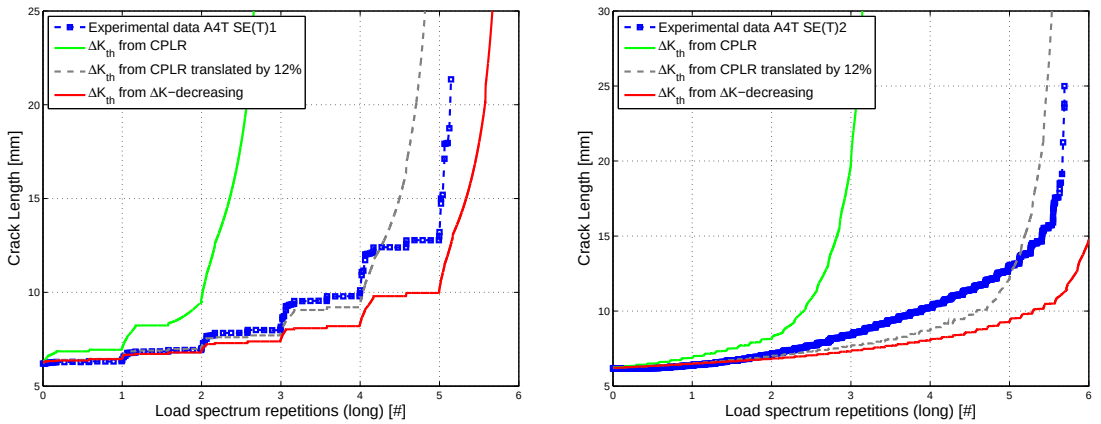

(a) Specimen A4T SE(T)1

(b) Specimen A4T SE(T)2

Figure 5.30: *Crack growth simulations onto SE(T) specimens made of A4T batch A, adopting a simple no-interaction model; matching the experiments by threshold translation*

Regarding 34CrNiMo6 steel grade, since it was shown that there was an effect of the block's length onto crack propagation, no univoque indication could be drawn about the increase of threshold to match the experiments. As shown in Figure 5.31, the test with longer blocks could be perfectly reproduced by an increase of 11% of the threshold, while the other one, tested applying shorter blocks, required an increase of 25% of the threshold in order to match prediction and experimental evidence.

Figure 5.32, relative to crack growth simulations onto 30NiCrMoV12 high strength

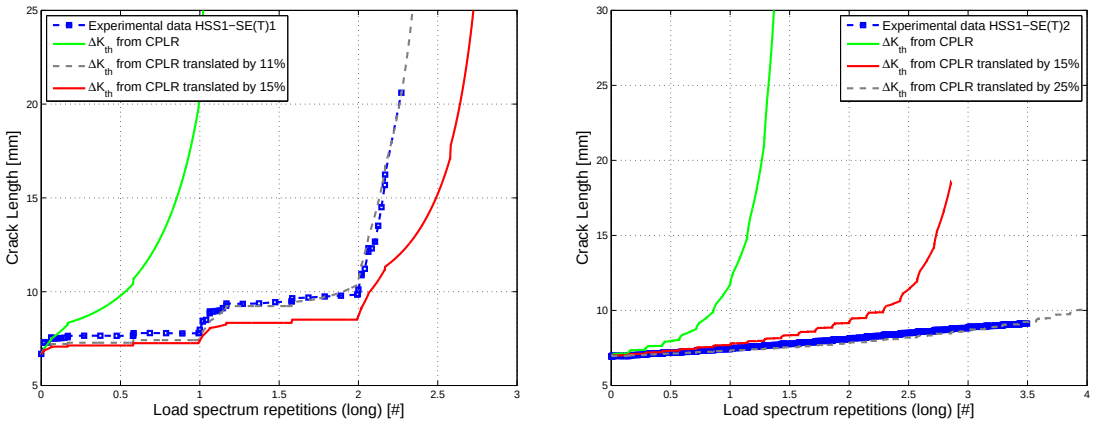

(a) Specimen HSS1-SE(T)1 (b) Specimen HSS1-SE(T)2

Figure 5.31: *Crack growth simulations onto SE(T) specimens made of 34CrNiMo6, adopting the simple no-interaction model; matching the experiments by threshold translation*

steel grade, shows the needing of threshold translation of about 30%. In particular, crack growth on specimen HSS2-SE(T)1, tested with Time History loading, was well predicted increasing the threshold by 28%, while specimen HSS2-SE(T)2, tested against long blocks, was well predicted increasing the threshold by a slightly higher value, corresponding to 38%; the 28% translation, for this second specimen, returned predictions on the conservative side. This behavior is in agreement with the indications drawn by the Strip-Yield method, for the same specimens, in Figure 5.27: the second specimen require a higher threshold translation or, equivalently, a lower α value, in order not to allow for propagation during the long blocks at low stress level.

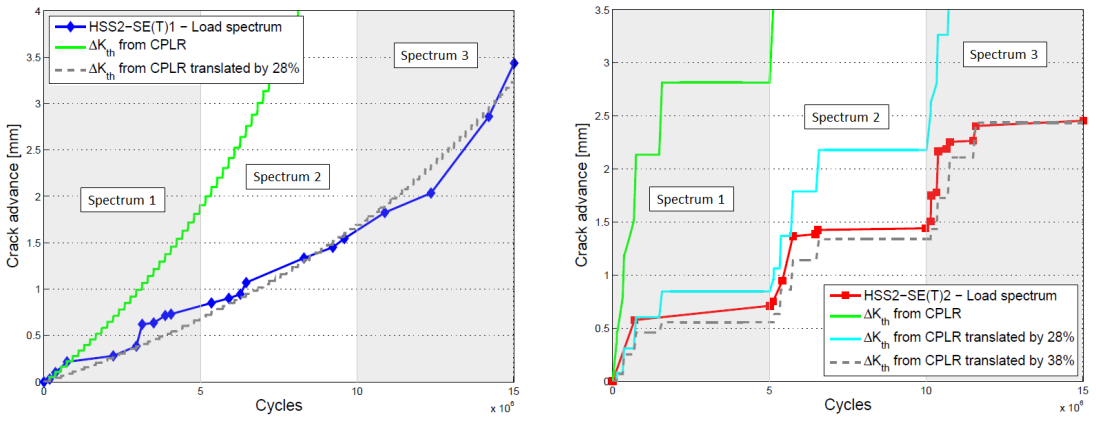

(a) Specimen HSS2-SE(T)1 (b) Specimen HSS2-SE(T)2

Figure 5.32: *Crack growth simulations onto SE(T) specimens made of 30NiCrMoV12, adopting the simple no-interaction model; matching the experiments by threshold translation*

Finally, considering the experiments onto A4T batch B medium strength steel grade, an increasing of the thresholds of about 12% (Fig. 5.33) seems to be adequate to match

both the tests onto SE(T) specimens and, above all, the test carried out onto the full-scale specimen tested at VA.

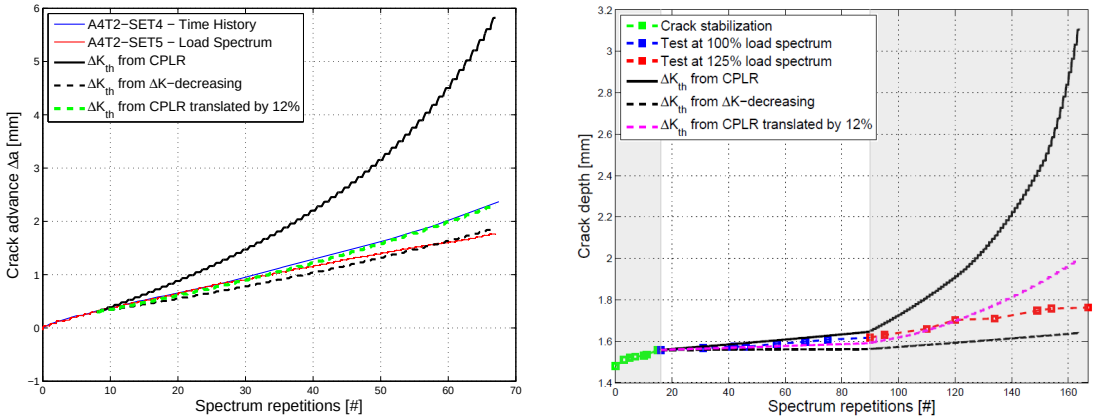

(a) SE(T) specimens A4T2-SET4 and 5

(b) Full-scale specimen

Figure 5.33: *Crack growth simulations onto SE(T) and full-scale specimens made of A4T batch B, adopting a simple no-interaction model; matching the experiments by threshold translation*

A summary of the amount of threshold translation, from CPLR, required in order to match the experiments with a no-interaction model is shown in Table 5.5.

Specimen	material	VA loading	translation of the CPLR threshold
A4T SE(T)1	A4T batch A	long blocks ($R \neq -1$)	12%
A4T SE(T)2	A4T batch A	short blocks ($R \neq -1$)	12%
HSS1-SE(T)1	34CrNiMo6	long blocks ($R \neq -1$)	11%
HSS1-SE(T)2	34CrNiMo6	short blocks ($R \neq -1$)	25%
HSS2-SE(T)1	30NiCrMoV12	time history ($R = -1$)	28%
HSS2-SE(T)2	30NiCrMoV12	block loading ($R = -1$)	38%
A4T2-SET4	A4T batch B	time history ($R = -1$)	12%
A4T2-SET5	A4T batch B	block loading ($R = -1$)	12%

Table 5.5: *Summary of the required CPLR threshold translation, in order to match the experiments*

Considering all the experiments and the simulations carried out, it seems that all the A4T medium strength steel tested, from both batches A and B, can be well predicted by a simple no-interaction model, increasing the thresholds from CPLR of about $10 \div 12\%$, thus remaining on the safe side. This is in agreement with the simulations carried out adopting the Strip-Yield model, where a similar α value was needed for the two A4T batches. A more complex scenario appears when considering all the high strength steels together, with increase of threshold varying from 11% (high ΔK values and long blocks) up to 38% (low ΔK values and long blocks). It seems that the higher amount of retardation, requiring high threshold translations to be captured, happens when stresses are low (specimens made of 30NiCrMoV12), while, applying high stresses, the retardation effect is small; this is in agreement with the indications found in literature [82]. It's worth remarking that CPLR and ΔK-decreasing, when leading

to different results, represent the lower and upper bound for crack propagation under VA loading; the required threshold increment to match the results does not exceed the ΔK-decreasing trend line.

Obviously, this approach is intended only as a simple attempt to match the experiments, not representing the retardation due to the load sequence and crack tip plasticity.

5.9 Plan of the inspection intervals

Based on the consideration that the adopted geometry of the SE(T) specimens results in experimental outcomes close to the full-scale specimens, making them 'companion' [90, 91] of full-scale axles, the derived crack growth curves and predictions were adopted for the definition of an appropriate inspection plan. The idea was trying to understand how much could be increased the distance between inspections due to the retardation effect, thus maintaining a given probability of failure. For this purpose, the distance between inspection was calculated, for all the specimen which showed a large propagation (A4T batch A and 34CrNiMo6), considering both the no-interaction CPLR prediction, as conservative result, and the no-interaction curve adopting the opportune threshold translation, treated as the realistic result, including retardation. Calculations were performed considering the POD curves by Benyon and Watson [18] for 'near-end' and 'far-end' UT scan and a total probability of failure equal to $7 \cdot 10^{-5}$ [16]. Results are given in Table 5.6, normalized against the distance between intervals in the worst case, when the detection is relied to the 'far-end' scan method onto the no-interaction prediction carried out adopting CPLR thresholds.

	ΔK_{th} from CPLR		ΔK_{th} translated from CPLR	
Specimen	**Far-end scan**	**Near-end scan**	**Far-end scan**	**Near-end scan**
A4T SE(T)1 (batch A)	1	1.95	1.63	3.51
A4T SE(T)2 (batch A)	1	2.03	1.62	3.49
HSS1-SE(T)1 (34CrNiMo6)	1	1.63	1.85	3.63
HSS1-SE(T)2 (34CrNiMo6)	1	1.87	3.35	6.77

Table 5.6: *Comparison of the normalized inspection intervals*

As expected, the 'near-end' scan is the better UT method, permitting a distance between inspection about $1.6 \div 2$ times the distance when adopting the 'far-end' scan method. But more than this, since this result was expected, it is important to notice, from Table 5.6, the increment of the distance between inspections made possible by an accurate description of the retardation effect. This increment can be quantified in, at least, 60%, when considering the worst case, up to more than 300% in case of high retardation, as was for specimen HSS1-SE(T)2. A correct evaluation of the retardation effect is of crucial importance for the definition of the inspection plan, allowing for a sensible reduction of controls, thus maintaining the probability of failure low, and, consequently, a reduction of operative costs.

5.10 Conclusions

In this part of the research, the effect of Variable Amplitude loading, in different shapes, onto crack propagation was considered, relatively to four different materials: two medium strength steel batches (A4T) and two high strength steel grades (34CrNiMo6 and 30NiCrMoV12) were considered. The four steel grades, typically adopted in the railway axle production, were firstly characterized against crack propagation under CA, adopting small-scale SE(B) specimens, then VA tests were carried out onto 'companion' SE(T) specimens, applying both Time History and equivalent Load Spectrum, eventually with different lengths of the blocks, and finally, simulations of crack propagation were carried out adopting simple no-interaction models or a more sophisticated (and complex) Strip-Yield model. The results of this part of the research can be so summarized:

1. Regarding the CA loading tests:
   - the two bathes of A4T material resulted in different thresholds, with batch A showing results higher (up to $10 \div 15\%$) than batch B;
   - thresholds obtained from CPLR and ΔK-decreasing methodologies resulted to be different only for the A4T batches (with CPLR on the lower side), while were substantially identical for the high strength steel grades;
   - 34CrNiMo6 and 30NiCrMoV12 high strength steel grades resulted in identical FCG diagrams;
   - fatigue crack growth curves at stress ratios different than 0.7 cannot be obtained from rigid translation of the effective crack growth curve; in fact the amount of crack closure required in order to match the FCG curves vary from 0.27, at very low da/dN, up to 0.5 in the upper region of the Paris diagram.
2. Regarding the experimental evidence from VA loading tests:
   - measurements of crack closure at VA resulted to be always higher than expected; this behavior appears to be related to the fact that no propagation (or almost) happened at lower stresses; the crack closure so remained 'frozen' at high levels, not having sufficient crack advance to assest;
   - no evident retardation effect arose in dependence of the shape of the VA loading, considering the medium strength steel A4T, from both batches: results from Time History and equivalent Load Spectrum well agree, as well as results from longer or shorter block's length;
   - an evident effect of retardation, on the contrary, appeared, in dependence of the length of the blocks, considering the high strength steel 34CrNiMo6, tested at stress ratios different than -1 and at high ΔK values;
   - the same retardation effect did not appear, on the similar 30NiCrMoV12 steel grade, tested at lower ΔK values;
3. Regarding the crack growth simulations:
   - simulations adopting the thresholds from CPLR resulted always in conservative results; adopting thresholds from ΔK-decreasing (when different from

CPLR), on the contrary, always resulted in simulations longer than the experimental evidence, apart from the specimen showing a large amount of retardation; the experimental evidence is always in between the two simulations;

- simulations carried out adopting the more complex Strip-Yield model resulted, regarding the medium strength A4T steel grade, in predictions close to experiments when calibrated with an α factor close to 2.5; regarding the high strength steels, instead, it was necessary to adopt two $alpha$ values: 2.5 for high ΔK values, in the linear Paris regime of the crack growth curve, or 1.75 for lower ΔK values, close to the threshold; due to the fact that crack growth curves at R$\div 0.7$ cannot be obtained from rigid translation of the 'effective' one, crack growth simulations by Strip-Yield are not always accurate;
- the experimental outcomes could always be well predicted by a simple translation of the CPLR thresholds; a value close to $10 \div 12\%$ seems to be adequate for A4T steel grade, while a higher value is suitable for high strength steels; this procedure is intended as a suggestion for coarse crack growth simulations, only valid as first attempt, but remaining on the safe side.

Concluding Remarks

The starting point of this Ph.D thesis was the discussion of the existing methodologies for performing fatigue assessment onto railway axles. Three methods of fatigue assessment exist: the simplest one is the design against fatigue limit, with an infinite life approach, according to the current regulations, the second one is the damage sum and the last and more complex is the damage tolerant approach, only recently proposed as application to railway axles.

An overview of the design approaches was firstly discussed, pointing out the importance of complementing the traditional calculations with damage tolerance, in order to take into account for degradation along lifetime and proper optimization of the lifecycle, by definition of appropriate inspection intervals.

Even if the damage tolerant approach is well known, it is relatively new in the railway field, and a few questions are still under discussion. Aim of this research was trying to improve a few points among them: firstly, an attempt to correlate the three methodologies of calculation was carried out, by assessment of the allowable damage sum, then the effect of residual stresses and variable amplitude loading onto lifetime calculations was carried out, in comparison to dedicated experiments.

The first step was represented by the fatigue assessment of small-scale specimens, made of a medium strength steel for railway axle production, carried out under variable amplitude loading, in accordance to damage sum methods, as in the most advanced fatigue guidelines. The allowable damage sum D, and the choice of the right fatigue curve onto which calculations should be carried out was discussed, comparing the experimental results, from VA loading tests, against predictions obtained by properly moduling the two variables under exam, in order firstly to match the experiments, then to make reliable and affordable predictions. It was found that a damage sum equal to one led to not conservative predictions: the dispersion of the experiments could better be represented by a damage sum set to 0.5. Calculations performed onto the 2.5% percentile of the fatigue curve, with an allowable damage sum equal to 0.3, in agreement to the FKM guidelines, led to sufficiently conservative predictions, being adequate as design criterion.

Limitations and contradictions of the current regulations were highlighted, and the need of, at least, complementing the traditional approach with the novel damage toler-

ant one was proved by an example of application of the approach to old axles, no longer complaint with the current regulations, in order to show how to manage their service life extension. A simple application of a damage sum criterion, based on the Haibach's rule, but adopting realistically derived load spectra, returned very long predictions, according to the evidence (none of these axles failed over more than 30 years of service), but in contrast to the European Standards, which are, maybe, too conservative. By use of appropriate crack-propagation models, in conjunction with the realistic derivation of the loading spectra, a procedure for the evaluation of a reliable inspection plan was proposed and discussed. Finally, a simple parameter was proposed, more indicative of the inspection intervals than the Safety Factor proposed by the current regulations.

Regarding the effect of the residual stress field onto crack propagation and lifetime assessment of railway axles, even if its importance was already highlighted in the literature, the focus was there pointed only onto the detrimental effect due to tensile residual stresses. In the last few decades, several surface mechanical procedures, generating compressive residual stresses, have been adopted to increase the service life of mechanical components subjected to fatigue. This approach has been more and more adopted also in the railway field, with deep-rolling as the adopted technological process; despite the beneficial effects of deep-rolling onto crack propagation are known, from other mechanical fields, no intensive studies onto its effects onto lifetime predictions of railway axles were found. In the present research, the effect of the residual stress onto crack propagation was addressed: full-scale specimens, made of the medium strength steel grade A4T, were machined and deep-rolled adopting the parameters adopted for axles from production. Then, crack propagation tests, under VA loading, were carried out in order to compare the experimental results with dedicated simulations, by the meaning of a no-interaction model taking into account the effect of the residual stresses onto the stress intensity factors at the crack tip. Depending on the initial notch size with respect to the depth of compressive residual stresses, no crack initiation could be observed for small flaws (R=2 mm), while unusual crack shape development, characterized by crack branching and wide yielded regions, happened for the largest ones (R=3 mm and R=4 mm). In any case, crack propagation occurred only at very high $\Delta K_{max}/\Delta K_{th}$ ratios, much higher than the typical values of commercial wheelsets. Regarding the crack growth simulations, results obtained by a simple no-interaction crack propagation model, taking into account the measured stress field, were successfully compared to the full-scale experiments, opening the possibility of accurately planning the inspection intervals in the case of deep-rolled axles.

Finally, the effect of variable amplitude loading onto crack propagation was considered. In dependence of the applied load sequence, a certain amount of retardation or acceleration onto fatigue crack growth rate is usually observed, mainly addressed to the local plasticity at the crack tip and explained, from a global point of view, by adopting the plasticity-induced crack closure concept. Crack growth tests under variable amplitude loading were carried out onto companion SE(T) specimens, showing the same constraint effect at the crack tip as a railway axle, made of medium (two batches of A4T material) and high strength steels (34CrNiMo6 and 30NiCrMoV12). The variable amplitude loading applied was in the shape of time history or equivalent load spectrum, with different lengths of the blocks, in order to check the retardation effect due to the load sequence adopted. Two different block lengths, and two different load spectrum

were used, including or not the effect of a mean stress value, simulating the effect of press-fit onto the axle; crack propagation tests were so carried at stress ratios R=-1 and $-1 \leq \mathrm{R} \leq 0$. No evident retardation effect arose, in dependence of the shape of the VA loading, when considering the medium strength steel A4T, from both batches: results from Time History and equivalent block loading agree, as well as results from longer or shorter block lengths. Regarding the two high strength steel grades, an evident effect of retardation appeared when considering the high strength steel 34CrNiMo6, tested at stress ratios different than -1 and at high ΔK values, while no evident retardation appeared on the similar (at CA) 30NiCrMoV12 steel grade, tested at lower ΔK values. During each test, moreover, the crack closure at the crack tip was experimentally measured, returning always in trends higher than expected, by the Schijve equation; this behavior appears to be related to the fact that no propagation (or almost) happened at lower stresses; the crack closure so remained 'frozen' at high levels, not having sufficient crack advance to stabilize. Crack growth simulations were then carried out, trying to approximate at best the experimental evidence, adopting the threshold definition from different experimental techniques, CPLR and ΔK-decreasing. Firstly, crack growth simulations were carried out by the meaning of a no-interaction model, then, an attempt to simulate the retardation effect was carried out adopting the Strip-Yield (SY) model. A convergence analysis on the α parameter permitted to state that the most appropriate values, regarding A4T, stay around $2.5 \div 2.7$, when the CPLR thresholds were considered. The high strength steels were, instead, better represented by lower α values, depending on the amount of retardation, variable between 2 and 1. This was in agreement with the higher retardation of these steel grades. A simpler approximation was finally adopted, trying to match the experimental outcomes by translating upward the threshold $\Delta \mathrm{K}_{th}$ from CPLR. This approximation, which gave good results, according to the more complex Strip-Yield model, is suggested as a 'rule of thumb', for basic calculations of the perspective lifetime.

Finally, the increasing distance between inspections, possible by an accurate representation of the retardation effect, was discussed, considering the equivalence between SE(T) specimens and railway axles. In particular, it was found that, for a given failure probability, inspection intervals could be increased by 60% respect to predictions made with 'no interaction' and CPLR data.

APPENDIX $\mathcal{A}$

Evaluation of the Fatigue Crack growth rate

The evaluation of the fatigue crack growth rate (FCG) at the crack tip, for lifetime predictions, was carried out by the meaning of the so-called Nasgro equations [80], once evaluated the SIFs acting along the crack itself. The equation involved, describing the correlation between ΔK values and crack advance during fatigue cycling, da/dN, is shown in eq.(A.1).

$$\frac{da}{dN} = C\left[\left(\frac{1-f}{1-R}\right)\Delta K\right]^n \frac{\left(1-\dfrac{\Delta K_{th}}{\Delta K}\right)^p}{\left(1-\dfrac{K_{max}}{K_c}\right)^q} \tag{A.1}$$

Calibration of the involved parameters was carried out, for each tested material, by least squares regression, matching experimental data and equation. The term f (Newman closure function), in eq.(A.1), takes into account the effect of the stress ratio R onto crack propagation of long cracks under constant loading conditions, according to eq.(A.2), with parameters $A_0 \div A_3$ evaluated as in eq.(A.3) [80]:

$$f = \frac{K_{op}}{K_{max}} = \begin{cases} max\left(R, A_0 + A_1 R + A_2 R^2 + A_3 R^3\right) & \text{if } R \geq 0 \\ A_0 + A_1 R & \text{if } -2 \leq R < 0 \end{cases} \tag{A.2}$$

$$
\begin{aligned}
A_0 &= \left(0.825 - 0.34\alpha + 0.05\alpha^2\right)\left[cos\left(\frac{\pi}{2}\frac{S_{max}}{\sigma_0}\right)\right]^{1/\alpha} \\
A_1 &= \left(0.415 - 0.071\alpha\right)\frac{S_{max}}{\sigma_0} \\
A_2 &= 1 - A_0 - A_1 - A_3 \\
A_3 &= 2A_0 + A_1 - 1
\end{aligned}
\tag{A.3}
$$

The parameter α represents the constraint factor at the crack tip and varies, depending on the specimen's geometry; it was fixed, for regression, at the value 2.5, typical for the SE(B) geometry, according to the Nasgro manual and ASTM-E647 standard for testing [58, 80]. Regarding the other parameter involved, S_{max}/σ_0, great care was put on its definition, since it has a big effect on the evaluation of the FCG rate, as can be seen in Figure A.1; typically, in the Nasgro database [80], this parameter is set to 0.3, returning high values of da/dN, but this value is quite high, and leads to too much conservative evaluation of the FCG rates, especially when considering small flaws. During this research, the parameter S_{max}/σ_0, was not kept constant at a defined value, but evaluated, at every measured crack advance of each tested specimen, as the ratio between the maximum local stress, calculated considering the reduction of the resistent section, and the flow stress of the involved material.

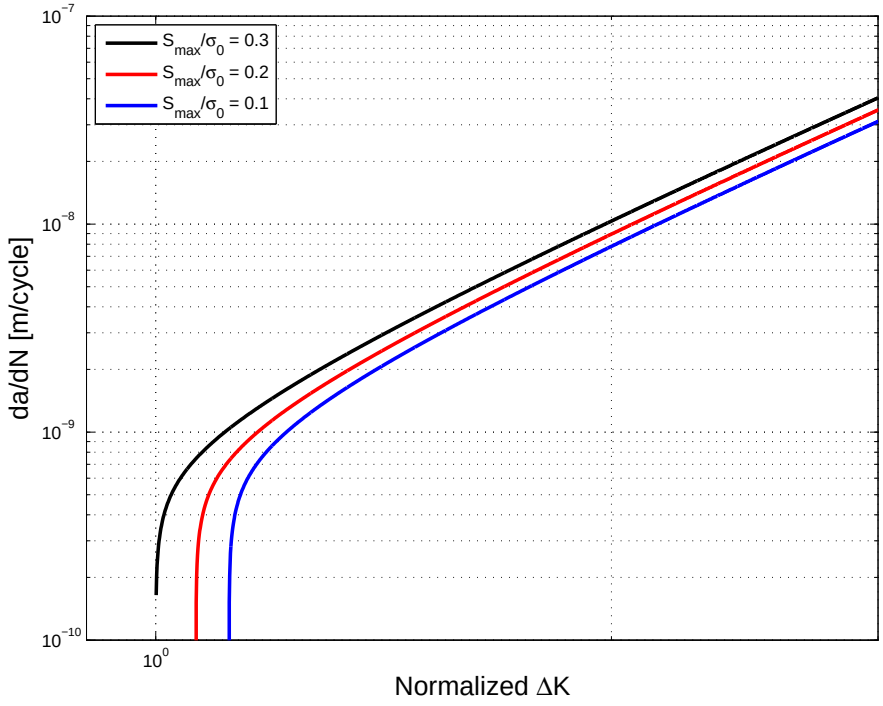

Figure A.1: *Effect of the parameter S_{max}/σ_0 onto crack growth rates.*

The variability of the parameter S_{max}/σ_0 was not kept into account only during the regression of the parameters to fit experimental data, but also during crack propagation simulations, by evaluation of the local stress state, at the crack tip, due to the loading condition; this parameter was considered as 'variable'.

In order to derive the parameters of the Nasgro equation, for evaluation of FCG, regression of the thresholds has firstly to be carried out, by the meaning of the Forman-Mettu equation for thresholds [64], in eq.(A.4), or the newer Nasgro equation for thresholds, in eq.(A.5).

$$\Delta K_{th} = \Delta K_{th0} \frac{\sqrt{\frac{a}{a+a_0}}}{\left[\frac{1-f}{(1-A_0)(1-R)}\right]^{(1-C_{th}R)}} \tag{A.4}$$

$$\Delta K_{th} = \begin{cases} \Delta K_1 \cdot \sqrt{\frac{a}{a+a_0}} \cdot \frac{\left(\frac{1-R}{1-f}\right)^{\left(1-RC_{th}^m\right)}}{(1-A_0)^{\left(C_{th}^p - RC_{th}^m\right)}} & \text{if } R < 0 \\ \Delta K_1 \cdot \sqrt{\frac{a}{a+a_0}} \cdot \frac{\left(\frac{1-R}{1-f}\right)^{\left(1-RC_{th}^p\right)}}{(1-A_0)^{(1-R)C_{th}^p}} & \text{if } R \geq 0 \end{cases} \tag{A.5}$$

The two equations are completely coincident for practical uses, returning the same values of thresholds, given the stress ratio; the choice of the equation to be adopted have to be done depending on the software adopted for crack propagation simulations; typically, newer crack propagation softwares prefer the second equation, based onto the threshold value at R=1 (ΔK_1) rather than at the stress ratio R=0 (ΔK_{th0}). The parameters of the threshold equation were evaluated by least square fit, as in eq.(A.6), relative to the newer equation.

$$S^2_{res,tot} = \sum_{i=1}^{4} \left(\Delta K^i_{th,exp} - \Delta K^i_{th,eq.(A.5)}\right)^2 \Longrightarrow \Delta K_1,\, C^p_{th},\, C^m_{th} \tag{A.6}$$

The remaining parameters, fitting eq.(A.1), were evaluated in the same way, by least square fit onto the experimental data.

$$S^2_{res,tot} = \sum_{i=1}^{4} \left(\log_{10}\left(\Delta K^i_{exp}\right) - \log_{10}\left(\Delta K^i_{eq.(A.1)}\right)\right)^2 \Longrightarrow \text{C, n, p, q} \tag{A.7}$$

APPENDIX B

Experimental and numerical investigations of fatigue crack closure in standard specimens

This appendix presents an experimental study of fatigue crack closure behavior in standard specimens of types C(T), SE(T) and M(T) made of the steel 25CrMo4, carried out during the research period of the author at IWM Fraunhofer institut in Freiburg im Breisgau, during the second phD year.

B.1 Introduction

Several experimental investigations of fatigue crack growth (FCG) in metallic materials provide the evidence of dependency of FCG rates on specimen geometry, even though test conditions comply with the small-scale yielding requirements, e.g. according to ASTM E 647 [58]. In particular, distinctly different FCG rates reported in [85–88] for two types of standard specimens, C(T) and M(T), resulted in opposite trend. FCG data obtained on particular standard geometry are not unconditionally transferable to other specimens or components. The difference in crack growth rates at equal applied stress intensity factor range, ΔK, and stress intensity ratio R, is usually addressed to the crack closure phenomenon [51], whereas the latter is often related to plasticity induced crack closure [108]. Besides the crack closure, the crack growth rate is governed by material damage within the plastic zone at the crack tip, and thus depends on the local stress triaxiality (constraint) [86–88]. The constraint effect, being a consequence of material yielding at the crack tip, can thus be linked to PICC. The work was focused on quantifying crack closure and examining its correlation to FCG rates in different specimens. The investigations were performed on three standard specimen types C(T), SE(T) and M(T) made of the 25CrMo4 steel grade. Besides the specimen geometry, the effect of the pre-cracking procedure on crack closure behavior and FCG rates was

explored.

B.2 Test procedure and experimental setup

Three specimen geometries, as schematically shown in Figure B.1, were adopted within the framework of this study:

- C(T) specimen: 50x25 mm^2 cross section, initial notch of 10 mm depth;
- SE(T) specimen: 29x10 mm^2 cross section, initial notch of 2 mm depth;
- M(T) specimen: 24x10 mm^2 cross section, initial notch of 5 mm depth.

Altogether nine specimens, three specimens of each type, were investigated.

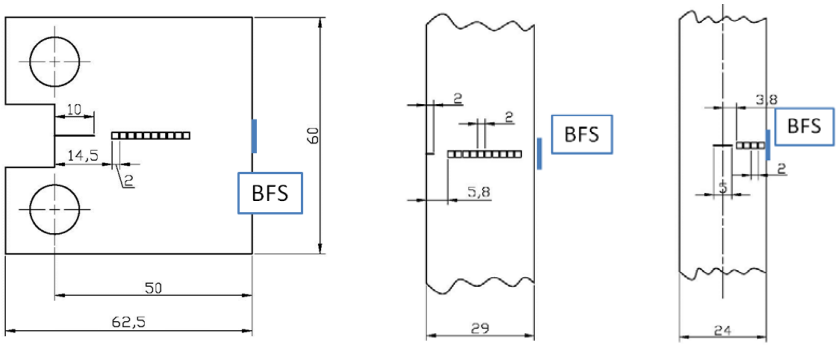

(a) C(T) specimen (b) SE(T) specimen (c) M(T) specimen

Figure B.1: *Specimen geometries with indication of the strain gage locations*

The initial notches were introduced by electric discharge machining (EDM) using a wire with a nominal diameter of 0.25 mm. Both standard pre-cracking (SPC), according to [58] and compression pre-cracking (CPC) were adopted. Two specimens of each type were subjected to SPC, while the third specimen was pre-cracked in compression. Subsequent FCG tests were performed at R = 0.1, under constant maximum load to avoid possible load interaction effects on the crack closure behavior. The final pre-crack length, as measured from the notch root, was achieved to be 1.5 to 2 mm. For specimens subjected to CPC, the crack typically stops after some 0.1 to 0.2 mm extension from the notch root. Further pre-cracking in those specimens was accomplished by applying cyclic loading with the parameters attained in the subsequent crack propagation tests. FCG tests were performed in a Rumul resonant testing machine equipped with a 150 kN load cell. The load frequency, depending on the specimen stiffness, was about 80 Hz for the C(T) specimen and 145 Hz for the SE(T) and M(T) geometries. Only the Paris range of the fatigue crack growth curve was investigated The crack length was optically measured at one side of each specimen, while the opposite specimen side was prepared for evaluating crack closure by means of the local compliance method. The local deformation has was recorded ahead of the crack tip during several cycles by the meaning of a chain of strain gages mounted ahead of the crack tip at each specimen (see Figure B.1). The strain gage chain adopted was of type HBM 1-KY21-2/120, consisting of ten individual strain gages having the grid dimension of 1.7 mm and spaced 2 mm

from each other. An additional single strain gage of the same grid dimension was glued at the center of the back face, in the prospective crack plane (Figure B.1). This back-face strain (BFS) gage was required for the evaluation of the crack closure by global compliance measurements, according to ASTM E 647 [58].

B.3 Results of the FCG tests

Figure B.2a shows FCG rates, da/dN, versus the stress intensity factor range, ΔK, for all specimens considered. The results cover ΔK values ranging from 11 to 60 MPa$\sqrt{\text{m}}$ and FCG rates within some $4 \cdot 10^{-6}$ to $8 \cdot 10^{-4}$ mm/cycle. For the specimen CT2, two data series are distinguished: these are denoted as CT2 and CT2*, corresponding to the first (80 Hz) and the second (5 Hz) test phases, respectively onto resonant and servo-hydraulic facility. Accordingly, no distinct frequency effect on FCG rates can be observed.

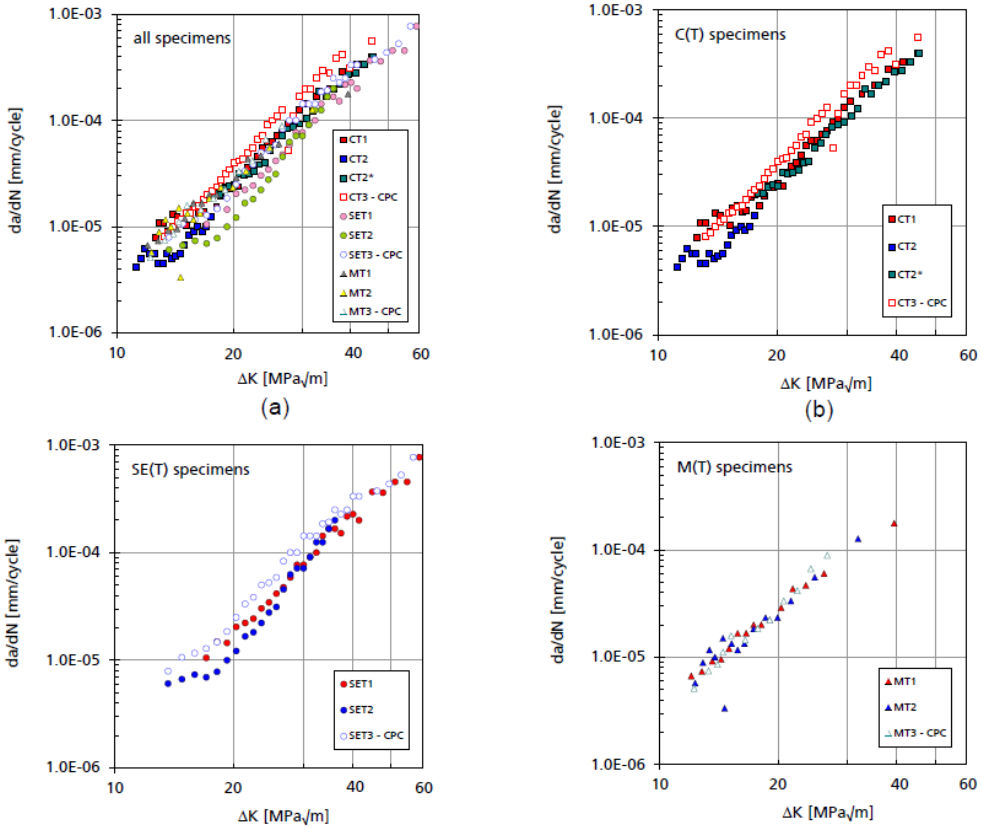

Figure B.2: *FCG data for all specimens (a) and separated for different specimen types and pre-cracking techniques: b) C(T); c) SE(T); d) M(T)*

In contrast, different specimen geometries turn out to result in different crack growth rates at equal ΔK. On average, the C(T) and SE(T) specimens reveal the highest and the lowest crack growth rates, respectively, while the results for M(T) specimens are allocated in an intermediate zone, being nearer to the C(T) data. The largest data scatter is observed around ΔK = 20 MPa$\sqrt{\text{m}}$, with an almost quadruplicate difference in da/dN values for the specimens SET2 and CT3. When considering test results for dif-

ferent specimen types (Figures B.2b, c and d), one can further conclude that higher FCG rates are likely to be achieved after compression pre-cracking, as compared to the conventional pre-cracking procedure. This observation holds for both C(T) and SE(T) specimens, while the M(T) specimens reveal no dependency of the FCG curve on the pre-cracking technique.

B.4 Results of crack closure measurements

The results of the crack closure evaluation are given in Table B.1 and Table B.2. The values U_{op} and U_{cl} refer to the local measuring techniques, whereas the signals from the first and the second strain gages ahead of the crack tip were taken into consideration. The values UBFS are derived from the back-face strain measurements (global methodology) as mean values for several succeeding recorded cycles. For reference purposes Schijve estimate is also provided in Table B.1.

Specimen		local method		global method
		U_{op}	U_{cl}	U_{BFS}
CT1		n.d.	0.475	0.677
CT2	80 Hz	0.715	0.474	0.782
	5 Hz	0.720	0.560	0.633
CT3 – CPC		0.915	0.790	0.296
SET1		0.665	0.560	0.645
SET2		0.788	0.660	0.655
SET3 – CPC		0.938	0.475	0.340
MT1		0.934	0.475	0.851
MT2		0.918	0.475	0.780
MT3 – CPC		0.899	0.760	0.894

Table B.1: *Crack closure factors evaluated at ΔK = 18 MPa$\sqrt{m}$*

Specimen	U_{BFS}	U_{op}	U_{cl}	Averaged open portion of the cycle, U_{mean} = ½(U_{op} + U_{cl})	
				single specimen	average of 3 specimens
CT1	0.646	0.776	0.499	0.638	0.658
CT2	0.504	0.726	0.562	0.644	
CT3 – CPC	0.496	0.86	0.526	0.693	
SET1	0.482	0.78	0.651	0.716	0.722
SET2	0.349	0.867	0.612	0.739	
SET3 – CPC	0.458	0.947	0.475	0.711	
MT1	0.231	0.895	0.582	0.738	0.722
MT2	0.228	0.945	0.475	0.710	
MT3 – CPC	0.258	0.945	0.489	0.717	

Table B.2: *Crack closure factors as averaged values during the whole test duration*

Table B.1 contains results obtained at a fixed stress intensity factor range of ΔK = 18 MPa$\sqrt{\text{m}}$, at which considerably different FCG rates are observed for different specimens and pre-cracking techniques. Moreover, at this ΔK level a comparison is possible between the two test phases for the specimen CT2. For all specimen geome-

tries considered, the U_{op} factor turns out to be distinctly higher than U_{cl}, which means that the crack opening load (within the increasing load branch) is lower than the load at crack tip closure (decreasing load branch). The estimates of U_{cl} for the C(T) and M(T) geometries are rather similar which corresponds with comparable FCG rates for the respective specimens. Furthermore, higher U_{op} and U_{cl} values for CT3 as compared to CT1 and CT2 may explain higher FCG rates for the CT3 specimen. However, in case of the M(T) and SE(T) specimens, only U_{op} correlates with the data trend for the two pre-cracking techniques in Figures B.2b, c and d, whereas U_{cl} seems to be not informative. Neither UBFS values provide meaningful correlation with the FCG rates for different specimens and pre-cracking techniques. Table B.2 summarizes crack closure estimates obtained by averaging the measurements over the whole test duration for each specimen. The respective conclusions agree in general with those at ΔK = 18 MPa$\sqrt{\text{m}}$. Accordingly, neither U_{op} nor U_{cl} alone provide a consistent description of the experimental findings for all specimen types. When using UBFS as a measure of crack closure, contradicting results are achieved at least for the C(T) specimens. The last two columns in Table B.2 show the crack closure factor, for both single specimens and specimen groups, obtained by averaging the U_{op} and U_{cl} values from local crack closure measurements. The corresponding value, U_{mean}, representing the fraction of a whole load cycle (including both loading and unloading branches) during which the crack remains completely open can be regarded as a measure for an effective crack driving force. While the U_{mean} could be judged as a proper parameter for two individual series of C(T) and M(T), it fails describing the SE(T) results. Moreover, using this parameter, similar FCG rates would be expected for M(T) and SE(T), on the one hand, and the lowest FCG rates for C(T), on the other hand, whereas both conclusions contradict the experimental findings.

B.5 Conclusions

Based on results of this study, the following conclusions can be drawn:

- The local methodology allows for distinguishing between crack closure and crack opening factors U_{cl} and U_{op}, respectively. The value of U_{cl} changes insignificantly during the whole specimen life, being roughly equal to 0.5 with moderate variations depending on particular specimen geometry and pre-cracking technique. In contrast, U_{op} changes considerably, constituting the highest and lowest values for M(T) and C(T), respectively, and thus being in contrast to the test results. Consequently, neither U_{op} nor U_{cl} are regarded as suitable measures for the 'effective' crack driving force.

- The average open fraction of the whole cycle U_{mean}, as derived by combining U_{cl} and U_{op}, yields the smallest value for C(T) and equal values for SE(T) and M(T) geometries. This is contradictory to experimental findings.

- Estimates of the crack closure factor from back-face strain measurements, UBFS, are subject to large scatter. Moreover, this parameter can explain neither comparable FCG rates for C(T) and M(T) nor higher FCG rates for the compression pre-cracked specimen CT3, as compared to CT1 and CT2.

Acknowledgements

Part of the present research was carried out in the frame of the MARAXIL Project, co-funded by Regione Lombardia (ID 16973, Rif. n° MAN-15) with support of IWM (Fraunhofer Institut für Werkstoffmechanik IWM). The author also acknowledges the support of the EURAXLES project for his research assistant position and the permission to publish results. The author is also grateful to LucchiniRS for the support and collaboration.

The author would like to thank Dr. M. Luke and Dr. I. Varfolomeev (IWM Fraunhofer institut) for the useful discussions and hospitality at IWM.

Bibliography

[1] UNI-EN13103. Railway applications - wheelsets and bogies - non powered axles - design method. UNI EN 13103:2012, UNI - Ente Nazionale Italiano di Unificazione, Milano, Italy, 2012.

[2] UNI-EN13104. Railway applications - wheelsets and bogies - powered axles - design method. UNI EN 13104:2012, UNI - Ente Nazionale Italiano di Unificazione, Milano, Italy, 2012.

[3] B. Hänel, E. Haibach, T. Seeger, G. Wirthgen, and H. Zenner. Fkm-guideline–analytical strength assessment of components in mechanical engineering. *Forschungskuratorium Maschinenbau eV (FKM), Research Association for Mechanical Engineering, Frankfurt*, 2003.

[4] M.A. Miner. Cumulative damage in fatigue. *Journal of applied mechanics*, 12(3):159–164, 1945.

[5] E. Haibach. *Modifizierte lineare Schadensakkumulations-hypothese zur Berücksichtigung des Dauerfestigkeitsabfalls mit fortschreitender Schädigung*. Laboratorium für Betriebsfestigkeit, 1970.

[6] V. Grubisic and G. Fischer. Procedure for reliable durability validation of train axles. *Materialwissenschaft und Werkstofftechnik*, 37(12):973–982, 2006.

[7] Widem: Wheelset integrated design and effective maintenance, www.widem.org, 2005-2008.

[8] S. Beretta, M. Carboni, A. Lo Conte, and E. Palermo. An investigation of the effects of corrosion on the fatigue strength of aln axle steel. *Proceedings of the Institution of Mechanical Engineers, Part F: Journal of Rail and Rapid Transit*, 222(2):129–143, 2008.

[9] N. Gravier, J.J. Viet, and A. Leluan. Prédiction de la durée de vie des essieux-axes ferroviaires. *Revue générale des chemins de fer*, 1999(3):33–62, 1999.

[10] C.C. Osgood. Damage-tolerant design(safe-life and fail-safe structural design philosophies in fatigue damage and operating lifetime control). *Machine Design*, 41:91–95, 1969.

[11] J.R. Combes. Design for damage tolerance. *Journal of Aircraft*, 7(1):18–20, 1970.

[12] U. Zerbst, M. Vormwald, C. Andersch, K. Mädler, and M. Pfuff. The development of a damage tolerance concept for railway components and its demonstration for a railway axle. *Engineering fracture mechanics*, 72(2):209–239, 2005.

[13] U. Zerbst, R. Lundén, K.O. Edel, and R.A. Smith. Introduction to the damage tolerance behaviour of railway rails–a review. *Engineering fracture mechanics*, 76(17):2563–2601, 2009.

[14] S. Beretta, M. Carboni, and S. Cervello. Design review of a freight railway axle: fatigue damage versus damage tolerance. *Materialwissenschaft und Werkstofftechnik*, 42(12):1099–1104, 2011.

[15] S. Cantini, S. Beretta, and M. Carboni. POD and inspection intervals of high speed railway axles. In *Proc. 15 th Int. Wheelset Congress*, 2007.

[16] VPI-Instandhaltungsleitfaden. Private Freight Wagon maintenance standard.

[17] W.D. Rummel. Recommended practice for a demonstration of nondestructive evaluation (nde) reliability on aircraft production parts, 1982.

[18] J.A. Benyon and A.S. Watson. The use of monte-carlo analysis to increase axle inspection interval. In *Proceedings of the* 13^{th} *International Wheelset Congress*, 2001.

[19] J.R. Davis. *ASM Handbook: Nondestructive evaluation and quality control*, volume 17. ASM International, 1989.

[20] M. Carboni and S. Beretta. Effect of probability of detection upon the definition of inspection intervals for railway axles. *Proceedings of the Institution of Mechanical Engineers, Part F: Journal of Rail and Rapid Transit*, 221(3):409–417, 2007.

[21] M.J. Nadal. Locomotives à vapeur. *Collection Encyclopédie Scientifique*, 186, 1908.

[22] S. Bruni, A. Collina, G. Diana, and P. Vanolo. Lateral dynamics of a railway vehicle in tangent track and curve: tests and simulation. In *The Dynamics of Vehicles on Roads and on Tracks - Supplement to Vehicle System Dynamics, Volume 33. Proceedings of the* 16^{th} *IAVSD Symposium held in Pretoria, South Africa, august 30-september 3, 1999*, 2000.

[23] S. Alfi and S. Bruni. Mathematical modelling of train–turnout interaction. *Vehicle System Dynamics*, 47(5):551–574, 2009.

[24] F. Braghin, S. Bruni, and G. Diana. Experimental and numerical investigation on the derailment of a railway wheelset with solid axle. *Vehicle System Dynamics*, 44(4):305–325, 2006.

[25] F. Braghin, S. Cervello, E. Dalle Mura, P. Kavan, and F. Resta. The WIDEM Project. load measurement campaign on Czech Pendolino train. In *Proceedings of the* 15^{th} *International Wheelset Congress, Prague, Czech Republic, September 23-27, 1999*, 2007.

[26] M. Matsuishi and T. Endo. Fatigue of metals subjected to varying stress. *Japan Society of Mechanical Engineers, Fukuoka, Japan*, pages 37–40, 1968.

[27] ASTM E1049-85. Standard practices for cycle counting in fatigue analysis. Technical report, ASTM International, 2011.

[28] ABAQUS User Manual. Version 6.12. *Hibbit, Karlsson & Sorensen*, 2012.

[29] M. Madia, S. Beretta, and U. Zerbst. An investigation on the influence of rotary bending and press fitting on stress intensity factors and fatigue crack growth in railway axles. *Engineering Fracture Mechanics*, 75(8):1906–1920, 2008.

[30] M. Madia, S. Beretta, M. Schödel, U. Zerbst, M. Luke, and I. Varfolomeev. Stress intensity factor solutions for cracks in railway axles. *Engineering Fracture Mechanics*, 78(5):764–792, 2011.

[31] X.R. Wu and J. Carlsson. *Weight functions and stress intensity factor solutions*. Pergamon, 1991.

[32] X. Wang and S.B. Lambert. Stress intensity factors for low aspect ratio semi-elliptical surface cracks in finite-thickness plates subjected to nonuniform stresses. *Engineering fracture mechanics*, 51(4):517–532, 1995.

[33] N. Gravier, J.J. Viet, and A. Leluan. Predicting the life of railway vehicle axles. In *Proceedings of the* 12^{th} *International Wheelset Congress*, pages 133–146. China, 1998.

[34] A. Carpinteri, R. Brighenti, and A. Spagnoli. Surface flaws in cylindrical shafts under rotary bending. *Fatigue & fracture of engineering materials & structures*, 21(9):1027–1035, 1998.

[35] M. Freitas and D. François. Analysis of fatigue crack growth in rotary bend specimens and railway axles. *Fatigue & fracture of engineering materials & structures*, 18(2):171–178, 1995.

[36] S. Beretta, A. Ghidini, and F. Lombardo. Fracture mechanics and scale effects in the fatigue of railway axles. *Engineering fracture mechanics*, 72(2):195–208, 2005.

[37] UNI-EN13261. Railway applications - wheelsets and bogies - axles - product requirements. UNI EN 13261:2011, UNI - Ente Nazionale Italiano di Unificazione, Milano, Italy, 2011.

[38] G.H. Farrahi, J.L. Lebrijn, and D. Couratin. Effect of shot peening on residual stress and fatigue life of a spring steel. *Fatigue & Fracture of Engineering Materials & Structures*, 18(2):211–220, 1995.

[39] M.A.S. Torres and H.J.C. Voorwald. An evaluation of shot peening, residual stress and stress relaxation on the fatigue life of aisi 4340 steel. *International Journal of Fatigue*, 24(8):877–886, 2002.

[40] G. Hammersley, L. A Hackel, and F. Harris. Surface prestressing to improve fatigue strength of components by laser shot peening. *Optics and Lasers in Engineering*, 34(4):327–337, 2000.

[41] M.A. Moshier and B.M. Hillberry. The inclusion of compressive residual stress effects in crack growth modelling. *Fatigue & fracture of engineering materials & structures*, 22(6):519–526, 1999.

[42] F.P. Brennan, S.S. Ngiam, and C.W. Lee. An experimental and analytical study of fatigue crack shape control by cold working. *Engineering Fracture Mechanics*, 75(3):355–363, 2008.

[43] C. Gardin, S. Courtin, G. Bezine, D. Bertheau, and H. Hamouda. Numerical simulation of fatigue crack propagation in compressive residual stress fields of notched round bars. *Fatigue & Fracture of Engineering Materials & Structures*, 30(3):231–242, 2007.

[44] C. Gardin, S. Courtin, D. Bertheau, G. Bezine, and H. Ben Hadj Hamouda. The influence of roller burnishing on the fatigue crack propagation in notched round bars - experimental observations under three-point bending. *Fatigue & Fracture of Engineering Materials & Structures*, 30(4):342–350, 2007.

[45] E.R. De los Rios, A. Walley, M.T. Milan, and G. Hammersley. Fatigue crack initiation and propagation on shot–peened surfaces in {A316} stainless steel. *International Journal of Fatigue*, 17(7):493–499, 1995.

[46] P.S. Song and C.C. Wen. Crack closure and crack growth behaviour in shot peened fatigued specimen. *Engineering Fracture Mechanics*, 63(3):295–304, 1999.

[47] O. Hatamleh, J. Lyons, and R. Forman. Laser and shot peening effects on fatigue crack growth in friction stir welded 7075–T7351 aluminum alloy joints. *International Journal of Fatigue*, 29(3):421–434, 2007.

[48] I. Altenberger. Deep rolling - the past, the present and the future. In *Proceedings of 9th International Conference on Shot Peening*, pages 6–9, 2005.

[49] J. Lebahn, H. Heyer, and M. Sander. Numerical stress intensity factor calculation in flawed round bars validated by crack propagation tests. *Engineering Fracture Mechanics*, 2013.

[50] T.L. Anderson. *Fracture Mechanics, Fundamental and Applications*. Bona Raton, 2nd edition, 1995.

[51] W. Elbert. The significance of fatigue crack closure. In *Damage Tolerance in Aircraft Structures: A Symposium Presented at the Seventy-third Annual Meeting American Society for Testing and Materials, Toronto, Ontario, Canada, 21-26 June 1970*, volume 486, page 230. ASTM International, 1971.

[52] J.C. Newman. A crack-closure model for predicting fatigue crack growth under aircraft spectrum loading. *ASTM STP*, 748:53–84, 1981.

[53] J. Schijve. Some formulas for the crack opening stress level. *Engineering Fracture Mechanics*, 14(3):461–465, 1981.

[54] J. Schijve. *Fatigue crack propagation and the stress intensity factor*. TH Delft, Delft, 1973.

[55] J.C. Newman and W. Elbert. *Mechanics of fatigue crack closure*, volume 982. Astm International, 1988.

[56] H. Tsukuda, H. Ogiyama, and T. Shiraishi. Fatigue crack growth and closure at high stress ratios. *Fatigue & Fracture of Engineering Materials & Structures*, 18(4):503–514, 1995.

[57] J.D. Dougherty, J. Padovan, and T.S. Srivatsan. Fatigue crack propagation and closure behavior of modified 1070 steel: finite element study. *Engineering Fracture Mechanics*, 56(2):189–212, 1997.

[58] ASTM Standard. E647-05: Standard test method for measurement of fatigue crack-growth rates. *Annual book of ASTM standards*, 3 (1), 2005.

[59] D.H. Chen and H. Nisitani. Analytical and experimental study of crack closure behavior based on an s-shaped unloading curve. *Mechanics of fatigue crack closure*, pages 475–488, 1988.

[60] M. Toyosada and T. Niwa. The significance of rpg load for fatigue crack propagation and the development of a compliance measuring system. *International journal of fracture*, 67(3):217–230, 1994.

[61] F.C. Tong and T.G.F. Gray. Fatigue crack closure study based on whole-field displacements. *International journal of fatigue*, 18(8):593–601, 1996.

[62] F.A. Diaz, E.A. Patterson, R.A. Tomlinson, and J.R. Yates. Measuring stress intensity factors during fatigue crack growth using thermoelasticity. *Fatigue & Fracture of Engineering Materials & Structures*, 27(7):571–583, 2004.

[63] S.I. Rokhlin and J.Y. Kim. In situ ultrasonic measurement of crack closure. *International journal of fatigue*, 25(1):51–58, 2003.

[64] R.G. Forman and S.R. Mettu. Behavior of surface and corner cracks subjected to tensile and bending loads in ti-6al-4v alloy. Technical report, National Aeronautics and Space Administration, Houston, TX (USA). Lyndon B. Johnson Space Center, 1990.

[65] J.C. Newman. A crack opening stress equation for fatigue crack growth. *International Journal of Fracture*, 24(4):R131–R135, 1984.

[66] EL HADDAD et al. Fatigue crack propagation of short cracks. *Trans. ASME J. Eng. Mater. Technol.*, 110:42–46, 1979.

[67] R. Pippan, H.P. Stüwe, and K. Golos. A comparison of different methods to determine the threshold of fatigue crack propagation. *International journal of fatigue*, 16(8):579–582, 1994.

[68] S.C. Forth, Newman J.C., and R.G. Forman. On generating fatigue crack growth thresholds. *International Journal of Fatigue*, 25(1):9–15, 2003.

[69] S.C. Forth, Newman J.C., and R.G. Forman. Evaluation of fatigue crack thresholds using various experimental methods. *ASTM SPECIAL TECHNICAL PUBLICATION*, 1461:203, 2005.

[70] J.C. Newman, J. Schneider, A. Daniel, and D. McKnight. Compression precracking to generate near threshold fatigue-crack-growth rates in two aluminum alloys. *International journal of fatigue*, 27(10):1432–1440, 2005.

[71] S. Beretta and M. Carboni. Variable amplitude fatigue crack growth in a mild steel for railway axles: experiments and predictive models. *Engineering Fracture Mechanics*, 78(5):848–862, 2011.

[72] M. Carboni, L. Patriarca, and D. Regazzi. Determination of ΔK_{th} by compression pre-cracking in a structural steel. *J ASTM Int*, 6(9):1–13, 2009.

[73] R. Pippan. The growth of short cracks under cyclic compression. *Fatigue & Fracture of Engineering Materials & Structures*, 9(5):319–328, 1987.

[74] J.C. Newman and Y. Yamada. Compression precracking methods to generate near-threshold fatigue-crack-growth-rate data. *International Journal of Fatigue*, 32(6):879–885, 2010.

[75] M.A. James, S.C. Forth, and J.A. Newman. Load history effects resulting from compression precracking. *ASTM SPECIAL TECHNICAL PUBLICATION*, 1461:43, 2005.

[76] J. Schijve and D. Broek. Crack propagation: the results of a test programme based on a gust spectrum with variable amplitude loading. *Aircraft Engineering and Aerospace Technology*, 34(11):314–316, 1962.

[77] S. Suresh. *Fatigue of materials*. Cambridge university press, 1998.

[78] J.A. Bannantine, J.J. Comer, and J.L. Handrock. *Fundamentals of metal fatigue analysis*, volume 90. Prentice Hall Englewood Cliffs, NJ, 1990.

[79] W. Schütz. A history of fatigue. *Engineering Fracture Mechanics*, 54(2):263–300, 1996.

[80] NASA Johnson Space Center. Fatigue crack growth computer program nasgro version 4.2-reference manual, 2006.

[81] J.A. Harter. Afgrow users guide and technical manual. Technical report, DTIC Document, 1999.

[82] M. Luke, I. Varfolomeev, K. Lütkepohl, and A. Esderts. Fatigue crack growth in railway axles: assessment concept and validation tests. *Engineering Fracture Mechanics*, 78(5):714–730, 2011.

[83] K. Mädler. Experimental evaluation of wheelset axles residual life time on a full-scale wheel-rail roller test rig - an experience report. In *Proceedings of the* 17^{th} *International Wheelset Congress, Kiev, September 22-27, 2013*.

[84] D.S. Dugdale. Yielding of steel sheets containing slits. *Journal of the Mechanics and Physics of Solids*, 8(2):100–104, 1960.

[85] R.S. Vecchio, J.S. Crompton, and R.W. Hertzberg. The influence of specimen geometry on near threshold fatigue crack growth. *Fatigue & Fracture of Engineering Materials & Structures*, 10(4):333–342, 1987.

[86] J. Tong. T-stress and its implications for crack growth. *Engineering fracture mechanics*, 69(12):1325–1337, 2002.

[87] P. Hutař, S. Seitl, and Z. Knésl. Effect of constraint on fatigue crack propagation near threshold in medium carbon steel. *Computational materials science*, 37(1):51–57, 2006.

[88] I. Varfolomeev, M. Luke, and M. Burdack. Effect of specimen geometry on fatigue crack growth rates for the railway axle material EA4T. *Engineering Fracture Mechanics*, 78(5):742–753, 2011.

[89] D. Regazzi, I. Varfolomeev, S. Moroz, M. Luke, and S. Beretta. Experimental and numerical investigations of fatigue crack closure in standard specimens. *DVM 45, Berlin, February 19-20, 2013*.

[90] M. Carboni, S. Beretta, and M. Madia. Analysis of crack growth at R=-1 under variable amplitude loading on a steel for railway axles. *J ASTM Int*, 5(7), 2008.

[91] A. Conle and H. Nowack. Verification of a neuber-based notch analysis by the companion-specimen method. *Experimental Mechanics*, 17(2):57–63, 1977.

[92] EURAXLES European Project. http://www.euraxles.eu/, 2013.

[93] W.B. Nelson. *Applied life data analysis*, volume 577. Wiley. com, 2005.

[94] S. Bruni, P. Belforte, and L. Mazzola. An alternative method for axle calculation in the frame of en13103/13104. *WC*, 2007.

[95] S. Bruni, R. Corradi, and L. Mazzola. Wheel rail contact forces as input for optimal and robust axle design. *CM*, 2009.

[96] J. Martínez-Casas, L. Mazzola, L. Baeza, and S. Bruni. Numerical estimation of stresses in railway axles using a train-track interaction model. *International Journal of Fatigue*, 2012.

[97] S. Bruni, J. Vinolas, M. Berg, O. Polach, and S. Stichel. Modelling of suspension components in a rail vehicle dynamics context. *Vehicle System Dynamics*, 49(7):1021–1072, 2011.

[98] E. Di Gialleonardo, F. Braghin, and S. Bruni. The influence of track modelling options on the simulation of rail vehicle dynamics. *Journal of Sound and Vibration*, 331(19):4246–4258, 2012.

[99] M. Shiratori, T. Miyoshi, and K. Tanikawa. Analysis of stress intensity factors for surface cracks subjected to arbitrarily distributed surface stresses. *Trans. Japan Soc. Mech. Engrs.*, 52:409–417, 1986.

[100] S. Beretta, M. Carboni, S. Cantini, and A. Ghidini. Application of fatigue crack growth algorithms to railway axles and comparison of two steel grades. *Proceedings of the Institution of Mechanical Engineers, Part F: Journal of Rail and Rapid Transit*, 218(4):317–326, 2004.

[101] MARAXIL Project. http://maraxil.mecc.polimi.it/, 2013.

[102] M. Carboni and D. Regazzi. Effect of the experimental technique onto R dependence of ΔK_{th}. *Procedia Engineering*, 10:2937–2942, 2011.

[103] M.H. Swain. Monitoring small-crack growth by the replication method. *Small-Crack Test Methods*, 1:34–56, 1992.

[104] J. Krautkrämer and H. Krautkrämer. *Ultrasonic Testing of Materials*. Springer-Verlag, 1990.

[105] V. Hauk. *Structural and Residual Stress Analysis by Nondestructive Methods: Evaluation-Application-Assessment*. Access Online via Elsevier, 1997.

[106] M.E. Fitzpatrick, A.T. Fry, P. Holdway, F.A. Kandil, J. Shackleton, and L. Suominen. *NPL Good Practice Guide No. 52: Determination of Residual Stresses by X-ray Diffraction*. ISSN 1368-6550, 2002.

[107] J. Schijve. *Fatigue crack propagation in light alloy sheet material and structures*. NLL, 1960.

[108] J. Schijve. *Fatigue of structures and materials*. Springer, 2001.